

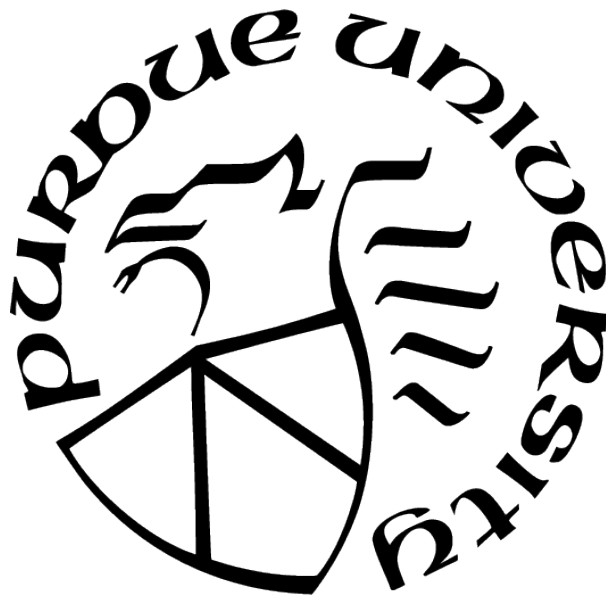
INTERACTION OF LIGHT WITH ORDERED ARRAY OF
RARE EARTH IONS IN SOLIDS

by
Arindam Nandi

A Dissertation

*Submitted to the Faculty of Purdue University
In Partial Fulfillment of the Requirements for the degree of*

Doctor of Philosophy



Department of Physics and Astronomy

West Lafayette, Indiana

May 2022

**THE PURDUE UNIVERSITY GRADUATE SCHOOL
STATEMENT OF COMMITTEE APPROVAL**

Dr. Mahdi Hosseini, Chair

School of Electrical and Computer Engineering

Dr. Chen-Lung Hung

Department of Physics and Astronomy

Dr. Zubin Jacob

School of Electrical and Computer Engineering

Dr. Hadiseh Alaeian

School of Electrical and Computer Engineering

Dr. Oana Malis

Department of Physics and Astronomy

Approved by:

Dr. Gabor A. Csathy

I dedicate this thesis to my parents, Ashok Kumar Nandi and Rintu Nandi, for their
endless love, support, and encouragement.

ACKNOWLEDGMENTS

I have been extremely fortunate to have received the support and guidance of many people during my time as a graduate student at Purdue. I sincerely appreciate the help and express gratitude to all.

First and foremost, I would like to thank my advisor, Prof. Mahdi Hosseini, for his insight and guidance during my Ph.D. His dedication to research motivates us all to explore new things. Along with being an exceptional scientist, he is a great teacher and inspiring mentor. I have learned a lot from him over the years, from various experimental techniques to using the latest software to approach a problem effectively. I will be forever grateful to him for all the help and support over the years.

I would also like to express sincere gratitude to all my committee members: Prof. Zubin Jacob, Prof. Chen-Lung Hung, Prof. Hadiseh Alaeian, Prof. Oana Malis for their support and advice during my research at Purdue. A humble acknowledgment goes out to all my professors at Purdue for valuable courses and insightful discussions. I am very thankful to Birck Nanotechnology Center, School of Electrical and Computer Engineering, and Department of Physics and Astronomy for providing my funding during my research. I am also grateful to the current and ex Physics and BNC staff, Sandy, Janice, Nancy, Richard, Brenda, for their unfailing and timely assistance to every administrative need, providing training on the laboratory instruments and making the labs a safe place to work.

A special thank you to all my lab mates, specially Xiaodong, Dongmin, Haechan, Kei-ichiro, for all the collaborative projects and many enlightening discussions. A big thank you to all my amazing friends: Amartya, Prabudhya, Sayantan da, Somrita, Sid bro, Shivam, Srishti, Sanchari, Satarupa, Aritra, Debadrita, Aarush, Riju and many others, for the beautiful memories that we shared. I cannot thank my fiancé, Indrani, enough for always being there for me and making me a better person. Far away from home, life would not have been the same without the endless fun and adventures with you all.

Lastly, I would like to thank my parents and sister for their constant support and endless love. It kept me motivated throughout the journey and encouraged me to perform better. I am also grateful to all my family members and friends who have supported me along the way.

Arindam Nandi, West Lafayette, March 2022

TABLE OF CONTENTS

LIST OF FIGURES	9
LIST OF SYMBOLS	14
ABBREVIATIONS	15
ABSTRACT	16
1 INTRODUCTION AND MOTIVATION	18
1.1 Thesis Outline	20
2 PROPERTIES OF RARE EARTH IONS	23
2.1 Electronic structure and transition dynamics of Rare Earth Ions	23
2.1.1 LS Coupling and JJ Coupling	24
2.1.2 REIs inside a crystal	25
2.2 Homogeneous and Inhomogeneous Broadening	25
2.3 Spectral Hole Burning	27
2.4 Population lifetime	29
2.5 Coherence time	30
2.6 Cross relaxation	30
2.6.1 Spin-Spin coupling	30
2.6.2 Spin-Lattice coupling	31
2.6.3 Multi-phonon processes	32
3 INTERACTION OF LIGHT WITH RARE EARTH IONS	33
3.1 Interaction of a two-level atom with a single mode light field	33
3.2 Atom light interactions inside cavity	36
3.2.1 FSR and Finesse	36
3.2.2 Quality Factor and Mode Volume	37
3.2.3 Purcell Factor	37
3.3 Optical Quantum memory with rare-earth ions	40

3.3.1	Controlled Reversible Inhomogeneous Broadening	40
3.3.2	Atomic Frequency Comb	41
4	EXPERIMENTAL TECHNIQUES	44
4.1	Low temperature measurements	44
4.1.1	Sample chamber	45
4.1.2	3D nano-positioners for fiber-to-chip coupling	46
4.2	Single photon detection	47
4.3	Photon Echo and Spin Echo	48
4.4	Homodyne and Heterodyne detection	49
5	THEORETICAL INVESTIGATION OF INTERACTION OF LIGHT WITH ATOMIC ARRAY	52
5.1	Introduction	53
5.2	Model: light interaction with a periodic lattice of atoms	53
5.3	Long-range cooperative light emission	55
5.4	Controlling dissipation	57
5.5	Photon generation	59
5.6	Storage in an ordered lattice and the effect of geometry	61
5.7	Conclusion	64
6	ATOMIC ARRAY IN SILICON PHOTONICS	65
6.1	Introduction	65
6.2	Theory	66
6.3	Experimental details	70
6.4	Measurements and results	73
6.4.1	Photon-assisted excitations	75
6.4.2	Absence of Sub and superradiant modes	76
6.4.3	Loss suppression due to atomic geometry	77
6.5	Fano resonance	79
6.6	Conclusion	80

7	ATOMIC ARRAY IN CRYSTAL	81
7.1	Introduction	82
7.2	Experimental details	82
7.3	Theory	84
7.4	Results	86
7.5	Conclusions	89
8	PREPARATION FREE STORAGE	91
8.1	Introduction	91
8.2	Traditional AFC memory	92
8.3	Experimental Approach for preparation free storage	93
8.4	Experimental Results	95
8.5	On-demand memory	98
8.6	Conclusion	98
9	CONCLUSION AND FUTURE DIRECTION	99
9.1	Summary and Conclusion	99
9.2	Future Direction	101
9.2.1	Atomic mirror assisted light trapping	101
9.2.2	Long-range cooperative resonances in Solid-state platform	101
9.2.3	Preparation free storage	102
	REFERENCES	104

LIST OF FIGURES

1.1	Integrated Quantum Communication network with communication nodes and quantum memory.	18
2.1	Electronic configuration of rare earth ions.	23
2.2	Homogeneous and inhomogeneous linewidth has been shown in this figure. Homogeneous linewidth (Γ_h) corresponds to the effect experienced equally by individual ions or atoms in the solid-state. The envelope of all the homogenous linewidths is defined as the inhomogeneous linewidth (Γ_{inh}), which is much broader in the frequency distribution.	27
2.3	Spectral hole-burning process for an ion with three ground and excited spin-levels. (b) shows a transient hole where the hole lifetime is determined by the excited state decay time of the ions. (c) shows a permanent hole where the hole lifetime is determined by ground state lifetime of the ions. Difference between the energy levels are not to scale.	28
2.4	Probing a spectral hole in the inhomogeneously broadened absorption spectrum for an atomic ensemble.	29
3.1	Schematic diagram of the enhancement of spontaneous emission rate due to cavity.	38
3.2	Schematic diagram of the two situations for rare-earth ions inside the cavity. (a) In this case, the emitter homogeneous linewidth is much less than cavity linewidth. (b) Here, the emitter homogeneous linewidth is much greater than cavity linewidth.	39
3.3	Schematic diagram of Atomic Frequency Comb (AFC) storage protocol. (a) shows an atom with an excited state $ e\rangle$, which is connected to two lower states $ g\rangle$ and $ s\rangle$. (b) shows input light is stored and comes out as an echo after a time $t = 2\pi/\Delta$	42
4.1	Cryogenic setup by Montana Instruments.	44
4.2	Sample chamber inside the Cryogenic setup.	45
4.3	Controller for 3D nano-positioners for high-precision alignment for fiber-to-chip coupling.	46
4.4	Single Photon Avalanche Detector Module from MPD.	47
4.5	Schematic diagram of the 2 pulse photon echo process.	49
4.6	Schematic diagram of the experimental setup for heterodyne detection.	50

5.1	(a) A schematic of an optical ring resonator hosting an array of atomic segments forming a lattice commensurate with the emission wavelength resonant with the cavity. (b) The input (E_{in}), transmitted (E_f) and reflected (E_b) light intensities for a pulse propagating through the bus waveguide coupled to the resonator. An atomic lattice consists of 100 segments with spacing of λ is considered. (c) A pulse of light resonant with the resonator can be amplified or deamplified depending on the initial state of the atoms and atomic spacing. σ_{ee} and σ_{gg} denote the atomic population in excited state $ e\rangle$ and ground state $ g\rangle$, respectively. The simulation parameters used are : $g/\Gamma = 0.5$, $\delta\omega = 0$, $N = 15$ and propagation time $c/r\phi_j \ll 2\pi/\Gamma$ where c is the velocity of light in vacuum and r is the radius of the ring resonator.	54
5.2	(a) Intensity of the emission light from an ensemble of 60 and 100 atoms inside the resonator. Inset is a plot of atomic population and coherence as a function of time. (b) Maximum emission intensity as a function of total atom number in the cavity for 100 atomic segments with different width of local atomic distribution. Simulation parameters include: cavity decay rate, $\kappa = 10^6\gamma$, atomic decoherence rate $\Gamma = 0.01\kappa$, light-atom coupling strength, and $g/\Gamma = 0.5$	57
5.3	(a) The level diagram of a three-level atom considered with two pump light deriving two Λ transitions creating photons in modes a and b in two directions. (b) A 1-D representation of the light-atom interaction for two arrays of atoms one commensurate and one incommensurate with the intra-cavity light whose also resonant with the Raman transition of the atoms. (c) The normalized probability amplitude of emitting bi-photons in the same direction is plotted as a function of lattice constant for 5 and 100 atoms interacting with the intra-cavity light.	60
5.4	The amplitude (a) and phase (b) of $\Theta(k)$ as a function of the incommensurability constant ζ . The gray curve shows amplitude and phase of $\Theta(k)$ for an atomic array out of the resonance with the optical wavelength. Results plotted considering 100 segments with $A = 0.2$	62
5.5	The difference in effective coupling (energy gap) of the two clockwise and counter clockwise modes.	63
6.1	Schematic of the designed active SiN ring resonator. Isotopically pure ^{168}Er ions are implanted as an array inside a microring cavity. The segments are separated by multiples of the wavelength of Er emission. At each segment with a width much smaller than the wavelength, around 10^4 ions were implanted along the diameter of the ring. A photonic crystal mirror is used to increase the collection efficiency to the lensed fiber on the left (output port). The excitation pump enters the ring either from the drop-port or the mirror-side waveguide using another lensed fiber.	66

6.2	(a) Result of numerical simulation for total field intensity ($T + R = \mathcal{E}_b(z = 0) ^2 + \mathcal{E}_f(z = L) ^2$) as a function of atom spacing from a lattice of atoms, which is normalized to that of a random atomic distribution. In this simulation, 15 atomic segments were considered. (b) Emission probability plotted using Eq.6.3 for $\eta_I = 0.25, 1.25$ and 2.5 (solid lines). The dashed line shows the Beta probability function approximately describing the decay of the probability at high cooperativities.	69
6.3	(a) Schematic cross section of the SiN resonator with Comsol simulation of the mode with effective index 1.58 shown in the inset. (b) Experimental setup showing two lensed fiber precisely controlled inside the cryostat using nanopositioners to couple light in and out of the sample. Inset shows the SEM of the ring resonator wall with smooth etching and u-grooved for fiber-to-chip coupling.	70
6.4	(a) Measured cavity transmission for the two orthogonal polarization. As the waveguide and ring are design for the TM mode, TM has the highest coupling while TE has the highest Q factor. The free-spectral range (FSR) of the two TM and TE modes and effective mode indices match the COMSOL calculations. The inset shows the fitted Lorentzian cavity transmission for TE (blue) and TM (orange) modes. (b) Photoluminescence decay of ions in the resonator is shown under 980nm (off-resonant) and $1.5 \mu\text{m}$ (on-resonant) excitation of annealed and not-annealed sample.	71
6.5	Mass spectrum of Er isotopes (inset) and Er, Au and Si ions measured at Sandia to deterministically select an Er isotope prior to implantation.	72
6.6	(a) Resonance photoluminescence spectrum at 4K (blue bars) and 300K (red bars). The enhanced emission around 1520nm is a signature of the Bragg resonance induced by the atomic lattice. Inset shows the ratio between the peak emission photon number at 1521nm (near the near the Bragg resonance) to that at 1532 nm (near the typical Er emission) as a function of temperature. Inset shows the temperature dependency of the emission ratio with a dashed line fitted to guide the eye. (b) The PL lifetime is shown for 4K (blue circles) and 300K (red squares). The longer PL decay time around 1535nm is associated with enhanced reabsorption away from the CL condition.	74
6.7	PL Emission of Er ions (green square) and pump transmission spectrum (red circle) at room temperature near 1532nm cavity dip.	76

6.8	(a) The ratio between the peak emission photon number at 1521nm to that at 1532 nm as a function of pump laser power. Here, for the iCL (ringC), near 1520nm, the emission ratio does not depend on laser power, but for the CL (ringB) the ratio increases with laser power and then saturates. Such nonlinear response across the emission spectrum in the CL is expected when emission exceeds the re-absorption probability in the CL. (b) Normalized emission (probability) as a function of spacing parameter, ζ , is plotted for ringA, ringB, and ringC (see text for details). Here ringA and ringB satisfy the CL condition near 1520nm while ringC does not. The dashed lines are Gaussian and Lorentzian fits to the regular and Bragg resonance emission profiles, respectively.	78
6.9	(a) Transmitted spectrum of the pump light through ringA with fitted Lorentzian width of 2.6 ± 0.1 GHz. (b) Emission spectrum near cavity resonance at 1520 and 1532nm for ringA and ringB. The spectrum is fitted with Fano-Lorentzian lines with asymmetry described by Fano parameter. The asymmetry in the lineshape of (a) is due to a change in the rate of the scan which does not appear when a wide scan is used. In the case of (b) the laser frequency is fixed for each point and the lineshape around 1532nm (green data) shows a symmetric Lorentzian, as expected from an iCL.	79
7.1	(a) A one-dimensional array of atomic scatterers is created inside an Er doped YSO crystal using a standing wave pump (pump A and B) to create spatio-spectral hole burning. Probe light EA or EB is applied after hole burning to measure reflection Er or transmission Et, respectively, detected by single photon detector (SPD). A magnetic field of 200mT was applied parallel to D1 axis for measurement of coherence time of Er ions. The crystal was placed in a cryostat at 4K. (b) shows numerical simulation of atomic population after atoms are pumped with a standing wave light. (c) Simulated coherent reflection of probe light as a function of optical density.	83
7.2	a) The population lifetime measured by observing the area of the spectral hole probed at different delay times after pumping. Inset shows the linewidth of a single hole in inhomogeneously broadened absorption spectrum. b) A two-pulse photon echo technique is used to measure the dephasing time at 4K probed by 1538nm light corresponding to the $I_{13/2}$ to $I_{15/2}$ transition. The echo area is plotted at varying delays between $\pi/2$ and π pulses of duration $0.8\mu s$ and $1.6\mu s$, respectively. The minimum time delay of $2.1\mu s$ is chosen to avoid the spontaneous emission caused by the nonideal π pulse.	86

7.3	<p>(a) Backscattered (reflected) probe after spatio-spectral hole burning ($t=0$) as a function of probe time. Reflection drops with time as population decays and probe washes out the atomic grating over time. By shifting the start of the probe pulse (ton), probe-induced loss is evidenced. The spontaneous emission is also shown (pump off, blue circles), which is negligible compared to the reflected light.</p> <p>(b) Normalized probe reflection (peak intensity) is shown as a function of pump duration and pump power (inset). Here, the probe pulse starts at $50\mu s$ after turning off the pump pulse to avoid any leakage. The solid lines are exponential fits of form $1 - Ae^{(-x/x_0)}$ used to capture the saturation behavior of the ions. Here A and x_0 are the fitting parameters. A pump power and duration of $1mW$ and $400\mu s$ is used for the main plot and the inset, respectively. A maximum reflection of 10% is measured from a $50\mu W$ probe, which corresponds to normalized value 1 in the vertical axes.</p> <p>(c) Normalized probe reflection (peak intensity) is plotted as a function of frequency difference between the counter-propagating pumps, $\omega_a - \omega_b$, of $1ms$ duration. All measurements were done at 4K and probe duration is $10ms$.</p>	88
7.4	<p>(a) Probe reflection and transmission spectra at 4K. Inset shows the result of numerical simulation taking into account the frequency fluctuation of the pumping laser. (b) Reflected probe spectra for different pumping duration is shown. The probe frequency in both plots is referenced to the center frequency of the spectral hole.</p>	90
8.1	<p>Schematic diagram of Atomic Frequency Comb. (a) shows the preparation pulse sequence to create the atomic frequency comb (AFC) structure. (b) shows The input pulse is stored and comes out as an echo after a time $t = 2\pi/\Delta$.</p>	92
8.2	<p>Schematic diagram of the experimental setup for the preparation free storage protocol. First, the light from the laser is modulated by the Electro-optic Modulator (EOM). Then it goes to the sample, which is kept in the 4K cryostat. Then the signal from the ions is mixed with the local oscillator using a beam splitter (BS) to do the heterodyne detection. We used a photodetector (PD) for heterodyne measurement.</p>	94
8.3	<p>Experimental results for echo measurements at modulation frequency of 5MHz. Here $\delta/2\pi$ is 5 MHz and the echo comes out at every $2\pi/\delta = 200ns$.</p>	96
8.4	<p>Experimental results for echo measurements at modulation frequency of 10MHz. Here $\delta/2\pi$ is 10 MHz and the echo comes out at every $2\pi/\delta = 100ns$.</p>	97

LIST OF SYMBOLS

c	Speed of light
λ	Wavelength of light
Q	Quality factor of cavity
V	Mode volume
g	Light-atom coupling strength
$\hat{\sigma}_{ee/gg}$	Atomic population operator
Ω	Inhomogeneous Broadening FWHM
κ	linewidth of resonator
T_1	Population decay time
T_2	Coherence time
γ_h	dcoherence rate
N_{eff}	Effective number of atoms
F_p	Purcell factor
η	co-operativity
F	Finesse of resonator
n_{eff}	effective refractive index
q	Fano parameter

ABBREVIATIONS

AOM	Accousto Optic Modulator
EOM	Electro Optic Modulator
FWHM	Full width at half maxima
DLCZ	Duan-Lukin-Cirac-Zoller protocol
SPD	Single photon detector
YSO	Yttrium Orthosilicate
FSR	Free spectral range
PhC	Photonic crystal
TE	Transverse electric
TM	Transverse Magnetic
SLPM	Standard liter per minute
PL	photoluminescence
LPCVD	Low-pressure chemical vapor deposition
RIE	Reactive-ion-etching
EBL	electron beam lithography
CL	Commensurate Lattice
iCL	Incommensurate Lattice
cQED	Cavity Quantum Electro-dynamics
CW	Continuous Wave

ABSTRACT

Rare-earth ions in crystalline hosts have been identified as attractive media for quantum optical applications where record-high coherence times, quantum storage efficiency in solids, and quantum storage bandwidth have been demonstrated. Among rare-earth ions, Erbium uniquely possesses optical transitions at 1.5 μm region, making it suitable for integration with fiber telecommunication and silicon photonics. However, the intra-4f optical transitions are parity forbidden for rare-earth ions. Although, transitions are observed due to the interaction of the 4f valence electrons' energy levels with crystal fields or the lattice vibrations, the photon emission rate is prolonged for these ions. For example, Er^{3+} excited state lifetime for 1530nm transition is $\sim 10ms$, which is about a million times longer than the excited state lifetime of alkali atoms like cesium and rubidium. There have been some recent works showing enhanced emission rate of erbium ions by $\sim 10^3$ times by building a nano-phonic cavity to reach high Purcell factors. Our alternative approach to solving this problem is to use an ensemble of ions instead of a single ion to induce collective interactions in a suitable platform. In one experiment, we fabricated a SiN micro-ring resonator and implanted 10^4 isotopically pure ^{168}Er ions in narrow segments located precisely in solids. The segments are typically separated by 0.962nm corresponding to multiples of the wavelength of Er emission at 1520nm. And we showed that when the lattice of ions is commensurate with the wavelength of the light, the scattering loss caused by the other ions is reduced. We have demonstrated for the first time that how designing atomic geometries in a solid-state photonic system can reduce the radiative loss due to spontaneous emission of ions into other photonic channels. This phenomenon is analogous to the Borrmann effect seen in x-ray transmissions of crystals at the Bragg angle of incidence. We have also shown how the interference between the optical cavity mode and atomic Bragg mode generates Fano-type resonance features. We performed these measurements using erbium ions in the SiN host. The limitations such as low coherence time and large inhomogeneous broadening in this platform prohibit observing cooperative and quantum behavior. To improve the optical property of erbium ions and study other cooperative effects, we engineered an effective ion array in an Er-doped Yttrium Orthosilicate crystal which can exhibit higher coherence time and narrower inhomogeneous

broadening compared to SiN. So, we used the spectral hole burning technique to make an atomic grating in randomly distributed Er ions inside YSO. Two counter-propagating pump pulses created a standing wave inside the crystal, which enabled the creation of spectral holes only near the antinode locations. At the same time, atoms near nodes remain in the ground state. Such atomic population grating behaved like an atomic array. We have seen coherent backscattering up to 20% of the incident probe from this atomic grating resembling a mirror. To increase the reflection efficiency, we tried to increase the ion concentration in the YSO crystal. But, at high concentrations, the dipole-dipole interaction increases the broadening and decoherence rates of the ions. To increase the optical density without increasing the ion concentration, we fabricated long waveguides in SiN and LiNbO₃ with rare-earth ions implanted inside. As a future direction, we are trying to increase the reflection efficiency from the atomic grating to the point where we can see atomic mirror-assisted light trapping. We are also trying to see long-range co-operative behavior from rare-earth ion-doped crystals and rare-earth ions implanted inside long waveguides. This can open possibilities of new quantum photonic device engineering for applications in scalable and multiplexed quantum networks.

1. INTRODUCTION AND MOTIVATION

There has been extensive interest in studying light-atom interactions for different applications, including quantum information, quantum computing, and long-range quantum communications. Much research is going on to generate and store optical qubits. To explain the motivation behind my thesis, I would like to discuss more about quantum communications. The idea of quantum communications is sharing entanglement or secure keys between two parties connected by quantum or classical channels [1], [2]. A quantum state of light constructed, for example, as superposition or entangled combinations of horizontal and vertical polarizations of light can be used to carry quantum information between parties [3].

The main advantage of quantum communication is that it is fundamentally secure. If an eavesdropper tries to steal the information, it can be detected. So, if we have Alice, who encodes her information in terms of any superposition states of light and send the information to Bob, the laws of quantum physics allow Alice and Bob to communicate securely. In this process, because quantum information cannot be copied or amplified, Alice and Bob can also detect presence of an eavesdropper in the channel [4].

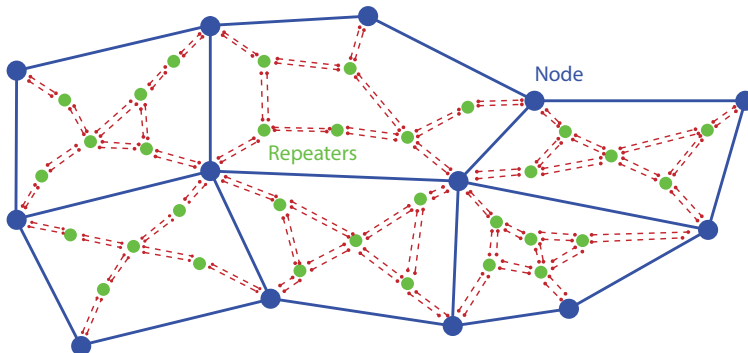


Figure 1.1. Integrated Quantum Communication network with communication nodes and quantum memory.

A more advanced quantum communication system, can be achieved where entangled photons are used to teleport quantum information from Alice to Bob without directly sending the quantum states carrying information to Bob. But the main challenge in quantum communication is that quantum information is sensitive to loss. And because such information

can not be amplified, we cannot propagate these photons for a very long distance due to loss from absorption and scattering. As a result, multinode links are proposed to relay quantum information over long distances. A network of nodes in 1D or 2D that enable distribution of quantum entanglement over long distances is referred to as quantum repeaters.

For example, the photons can not be sent directly between two far communication nodes (represented as blue dots in fig 1.1) for information transfer. This is due to loss from absorption and scattering which increases with propagation distance. This loss is significant limitation for long-distance quantum communication. That's why stations are needed connecting these dots, and, in each station, quantum memories (green dots in fig 1.1) are installed to relay the quantum information effectively [5], [6]. Primary devices needed for this long-distance communications are photon sources, quantum memories, quantum repeaters, and detectors, all working at the same wavelength. The least developed technology is quantum memory and thus it is a critical challenge in the field. [7], [8]

Our approach is to work on solid-state quantum memory to tackle this problem. We chose solid-state platforms because it is possible to miniaturize quantum optical elements, which enable us to in principle build many devices in a small area. Among quantum memory qubits, our main interest is to work with rare-earth ions for several advantages they have. One of the main advantages of using rare-earth ions is that they have smaller size than defects like Nitrogen-Vacancy (NV) center and quantum dots [9]. Because of the small size and shielded valence electrons of rare-earth ions, not only we can have a greater number of emitters, but also these emitters maintain their property relatively well inside a solid host. Another advantage is it is compatible with many fiber infrastructure and silicon photonics [7], [8], [10]. These ions can be doped or implanted in Silicon photonics and crystals, including YSO, YAG, LiNbO₃.

Another vital advantage of erbium is the presence of optical transition in the telecom band, which is helpful for fiber-based quantum communication applications. Fused silica fibers have minimum optical loss around 1550 nm wavelength. The mainstream telecom industry is heavily built with these optical fibers. So, a natural optical transition with good coherence properties at these wavelengths makes erbium ions a great candidate for quantum

information and communication applications. Erbium also has good optical properties in some hosts having a long coherence time, as shown in various recent publications.

This thesis explores the possibilities of erbium ions as suitable quantum emitters in solid-state platforms for quantum applications. This thesis also investigates using an ensemble of Er ions and their geometric structure to enhance light atom interactions and build an atomic array for low loss, efficient quantum memory.

1.1 Thesis Outline

The primary approach in this thesis was to explore the potential of Erbium ions in a solid medium for quantum communication and quantum storage applications. All the experiments and results are presented to help realize this goal. The thesis is organized as follows:

Chapter 2 describes the basic properties of rare-earth ions and their interaction with light in solid hosts. The static and dynamic interactions of rare-earth ions are presented, essential in determining coherence and storage properties in the solid-state medium.

Chapter 3 focuses on light atom interactions in free space and inside the cavity. The quantum optics theory is discussed from one atom in a single photonics mode to many atoms with clock-wise and anti-clockwise electromagnetic fields inside a cavity. Different important cavity parameters like FSR, finesse, Q factor are also discussed in this chapter. This chapter ends with a brief discussion of other quantum memory protocols used in this thesis in later experiments.

Chapter 4 explains the experimental techniques used for the experiments. These techniques include working at ultra-low temperatures, detecting single photons, two-pulse photon echo technique to determine coherence properties, homodyne and heterodyne measurements, generating different pulse shapes with acousto-optic modulators (AOM) and Electro-optic modulators (EOM), imaging systems, and fiber to chip coupling techniques. These experimental techniques were helpful in successfully conducting various experiments and getting the desired results.

Chapter 5 details our theoretical investigation of a novel regime of light-matter interaction, wherein collective and cooperative coherent excitations can emerge from the interaction

between engineered arrays of atoms. We consider an array of rare-earth ions precisely implanted into a solid-state photonic resonator. By designing the geometry of the ions within the resonator, we control the interference between the optical modes. The approach enables control of loss, absorption, and emission and may lead to the construction of on-chip quantum memories. Our theoretical study suggests photon generation and storage dependency to atomic geometry in an optical resonator.

Chapter 6 shows the experimental demonstration of the theoretical research in the previous chapter. In this project, an atomic array composed of up to 1000 implanted segments of erbium ions with telecom transition was designed, and optical characterization at 4K was done. This chapter experimentally demonstrates that using precision ion implantation in silicon nitride materials, arrays of rare-earth ions can be engineered to study collective atomic resonances.

In the above experimental project, we were looking at the SiN host. But SiN is an amorphous host, and implanting ions further degrades the optical properties. To improve the optical property and study other interesting effects, we tried to look into doped crystals. Chapter 7 demonstrates the experimental results and analysis that the absorption profile of a randomly distributed ensemble of rare-earth ions in a solid-state crystalline host can be engineered to create a 1D array of atomic scatterers effectively. Furthermore, coherent interference between lightly scattered atoms can reduce the propagation loss and give rise to coherent backscattering resembling a mirror.

Chapter 8 explains the ongoing work in the preparation of free quantum storage. Quantum memories are the building blocks for quantum information and long-distance quantum communication. A novel technique to store optical qubits in a solid-state platform is proposed where a long preparation time is unnecessary.

Chapter 9 gives the concluding remarks about the theoretical and experimental results towards possibilities of rare-earth ions in quantum communication and quantum storage applications. Finally, it points out the advances made during this research and scopes for advancements in quantum technologies in general.

Several sections of this thesis have been published by, submitted to, or accepted for publication in peer-reviewed scientific journals. Below is the list of some selected published

articles resulting from my research work during my Ph.D. which is also discussed in this thesis:

Arindam Nandi, Xiaodong Jiang, Dongmin Pak, Daniel Perry, Kyunghun Han, Edward S. Bielejec, Yi Xuan, and Mahdi Hosseini. **"Controlling light emission by engineering atomic geometries in silicon photonics."**Optics letters 45, no. 7 (2020): 1631-1634.

Arindam Nandi, Haechan An, and Mahdi Hosseini. **"Coherent atomic mirror formed by randomly distributed ions inside a crystal."** Optics Letters 46.8 (2021): 1880-1883.

Furuya, Keiichiro, Arindam Nandi, and Mahdi Hosseini. **"Study of atomic geometry and its effect on photon generation and storage."**Optical Materials Express 10, no. 2 (2020): 577-587.

Jiang, Xiaodong, Arindam Nandi, Dongmin Pak, and Mahdi Hosseini. **"Optomechanical frequency comb memory."**Optics letters 43, no. 20 (2018): 4973-4976.

Jiang, Xiaodong, Dongmin Pak, Arindam Nandi, Yi Xuan, and Mahdi Hosseini. **"Rare earth-implanted lithium niobate: Properties and on-chip integration."** Applied Physics Letters 115, no. 7 (2019): 071104.

Pak, Dongmin, Haechan An, Arindam Nandi, Xiaodong Jiang, Yi Xuan, and Mahdi Hosseini. **"Ytterbium-implanted photonic resonators based on thin film lithium niobate."** Journal of Applied Physics 128, no. 8 (2020): 084302.

2. PROPERTIES OF RARE EARTH IONS

This chapter describes the basic properties of rare-earth ions and their interaction with light in solid hosts. It illustrates rare-earth ions' static and dynamic interactions that are important in determining coherence and storage properties in the solid-state medium. The electronic structure of rare-earth ions is discussed in detail in the beginning. It also highlights the advantage of rare-earth ions because of their shielded valence electrons by outer orbitals. The population lifetime (T_1) and coherence time (T_2) are discussed in detail. At the end of this chapter, different dephasing and cross-relaxation processes like spin-spin coupling, spin-lattice coupling, and multiphoton processes are discussed. More in-depth discussions can be found in these references [9], [11], [12].

2.1 Electronic structure and transition dynamics of Rare Earth Ions

The rare-earth group consists of 15 elements, also known as the lanthanide series, named after the first element, Lanthanum. They share some common physical and chemical properties, of which the most important is the electronic configuration. The rare-earth elements have filled 5s, and 5p orbital ($5s^25p^6$) and their valence electrons reside in the inner 4f orbital, shielded by the outer filled orbitals.

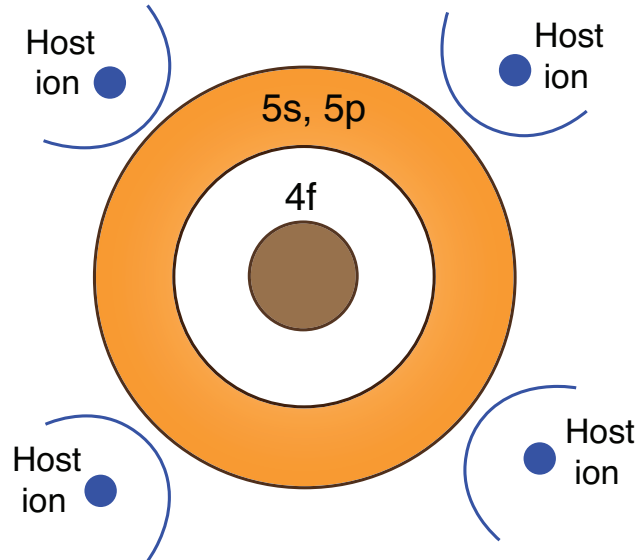


Figure 2.1. Electronic configuration of rare earth ions.

Because of this shielding of the valence electrons, the rare-earth ions possess good coherence properties and narrow homogeneous lines in low temperatures. Their transition energies do not vary too much in different solid hosts. In most of the compounds, rare earth elements reside as tri-positive ions. In a solid-state medium, Er^{3+} shows one of the narrowest homogeneous linewidths among rare earth elements, $\Gamma_h=73\text{Hz}$.

According to the Kramers degeneracy theorem, there is at least a twofold degeneracy for every energy level that possesses half-integer total spin. So, all alternate rare-earth ions have half-integer total spin, named Kramers ions. Their degeneracy can be lifted by applying a magnetic field. Though all the rare-earth ions have optical transitions, two of the rare-earth ions (Er^{3+}, Nd^{3+}) have optical transitions in the telecommunications band of fiber-optic communications, where the losses are minimal. This is a critical property of these rare-earth ions, making them an obvious choice for application in quantum communications and networks.

2.1.1 LS Coupling and JJ Coupling

This section presents the energy level structure of REIs from which we can have more insights on the optical transitions between the electronic states of the valence electrons in 4f orbital. To know exactly how to determine the energy levels of the valence electrons having different orbital and spin angular momentum, we need to understand different coupling schemes like LS (Russell–Saunders) coupling and JJ coupling.

In the LS coupling, the combination of individual electronic spins, S_i form a total spin angular momentum S. Similarly, the mix of individual orbital angular momentum l_i form total orbital angular momentum L. The interaction of total spin angular momentum, S, and total orbital angular momentum, L, is called L-S or Russell Sanders coupling. The total angular momentum J is the result of this L-S coupling.

In the case of JJ coupling, individual electronic spin angular momentum s_i interacts with its orbital angular momentum l_i . This interaction results in individual total angular momentum j_i . The combination of all the j_i results in total angular momentum J for the JJ coupling scheme.

For the rare-earth ions, the 4f valence electrons can be better described by L-S coupling; that is why it is the preferred basis in most literature.

2.1.2 REIs inside a crystal

If the rare-earth ions are implanted or doped inside a crystal, it experiences a local electric field which breaks the Kramers degeneracy of each multiplet to a maximum of $J + 1/2$ crystal field levels depending on the ions' site symmetry. For example, in the case of Er in YSO crystal, the ground multiplet $^4I_{15/2}$ can be split into $(15/2+1/2)=8$ Kramers doublets, and the $^4I_{13/2}$ multiplet splits into 7 doublets. This local field interaction inside the crystal is called crystal-field interaction, which is also responsible for inhomogeneous broadening discussed earlier. In addition, this crystal field dictates spin-lattice dynamics and optical transition strengths. So, the crystal field plays a massive role in determining coherence properties which is critical for quantum applications with rare-earth ions.

2.2 Homogeneous and Inhomogeneous Broadening

There are two main processes responsible for spectral line broadening, homogeneous and inhomogeneous, which determines the observed spectral width of optical transitions of the atoms. In the case of homogeneous broadening, the effect is experienced equally by individual ions or atoms in the solid-state. It is caused by dynamic fluctuations in the surrounding environment that act as perturbations on the atom's transition frequency and phase. For example, in erbium-doped compounds, the main factors determining the homogeneous linewidth are:

$$\Gamma_{hom} = \Gamma_{pop} + \Gamma_{Er-Er} + \Gamma_{phonon} + \Gamma_{Er-host} + \Gamma_{ISD}$$

Where, Γ_{pop} is the fundamental linewidth dependent on the excited state population lifetime, T_1 by this formula, $\Gamma_{pop} = 1/(2\pi T_1)$. Rare-earth ions have a very long excited state population lifetime, partially responsible for the large homogeneous linewidth of rare-earth ions in solids. For example, the excited state population lifetime of the optical transition

from $I_{13/2}$ to $I_{15/2}$ erbium ions in YSO crystal is $10ms$ at 4K according to the measurement in this work. The contribution of Γ_{Er-Er} comes from the phonon-induced electronic spin-flip transitions in their ground state, which perturbs the energy levels of the optical transitions. We can control this electronic spin flip by choosing the temperature, magnetic field strength, and direction of the magnetic field. The next contribution Γ_{phonon} comes from phonon coupling, where energy transfer occurs between the vibrational modes of the crystal and the rare-earth ions. The vibrational modes of any solid medium can generate oscillatory electric and magnetic fields. Phonons are discrete quanta of these electric fields, emitted or absorbed by the defects or ions. The contribution of Γ_{phonon} decreases with temperature, which is why most of the rare-earth-doped crystals are measured at cryogenic temperatures. $\Gamma_{Er-host}$ depends on the host lattice's nuclear and electron spins. Some host crystals, such as Y_2SiO_5 , exhibit very low nuclear magnetic moment and provide good optical properties to rare-earth ions. Instantaneous spectral diffusion (ISD) is responsible for the term Γ_{ISD} , which is caused by the changes in the local environment because of optical excitation of neighboring atoms. This effect can be reduced by having low atom concentrations or minimizing optical excitation densities. The homogeneous linewidth was measured in low concentration erbium doped YSO crystal in this work is 100KHz at 4K. The number of doped erbium ion was 0.005% of Ytterbium atom present in the crystal. For erbium ions implanted in amorphous host silicon nitride, we got a homogeneous linewidth of 60MHz. With sub-kelvin temperatures and a very high magnetic field, the homogeneous linewidth of erbium ions in YSO crystal can be reduced to below 100Hz.

In contrast to homogeneous broadening caused by dynamical processes, inhomogeneous broadening is caused by any static perturbation that changes the local environment for one ion in a solid different from another ion. These variations in the local environment are mainly due to crystal growth, impurities, or lattice imperfections and dislocations. These other disorders shift the center of the homogeneous linewidth of individual atoms or ions, resulting in a frequency distribution of transition frequencies. So, the combination of these homogeneously broadened lines for individual optical centers centered at different resonant frequencies creates a much broader absorption spectrum. This broadening, which is often Gaussian in shape, is known as inhomogeneous broadening, and the linewidth of this fre-

quency distribution is known as inhomogeneous linewidth (Γ_{inh}), which is also shown in Fig.1.

The inhomogeneous broadening can be very different depending on the optical center concentration and host material. For example, for the 0.005% Er:YSO crystal studied in this thesis, the inhomogeneous broadening is $\sim 2GHz$ at 4K without magnetic field, but in the amorphous host SiN, the inhomogeneous broadening of erbium was 400GHz for a concentration of $10^{14}/cm^2$.

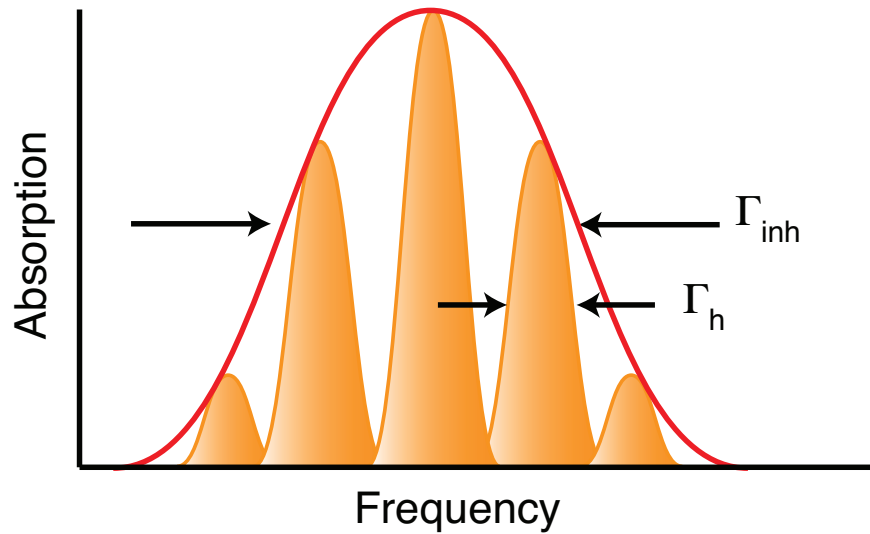


Figure 2.2. Homogeneous and inhomogeneous linewidth has been shown in this figure. Homogeneous linewidth (Γ_h) corresponds to the effect experienced equally by individual ions or atoms in the solid-state. The envelope of all the homogenous linewidths is defined as the inhomogeneous linewidth (Γ_{inh}), which is much broader in the frequency distribution.

2.3 Spectral Hole Burning

Spectral hole burning is a process where a narrowband laser selectively excites a subset of ions in the broad inhomogeneous profile. Ions that are resonant to that frequency band absorb the pump and go to the excited state. Repeated pumping can cause the removal of most of the ions in the ground state for that narrow frequency range. This causes a reduction of optical absorption at the laser pump frequency resulting in a spectral hole in the inhomogeneous spectrum. So, a specific homogeneous packet is saturated in the spectral

hole burning process, giving a narrow peak in the broad absorption spectrum. The hole linewidth can be very narrow, which is ultimately limited by the homogeneous linewidth of ions. Practically, the hole linewidth is often determined by the linewidth of the laser. If the laser power is extreme, it can cause a broadening of the spectral hole known as power broadening.

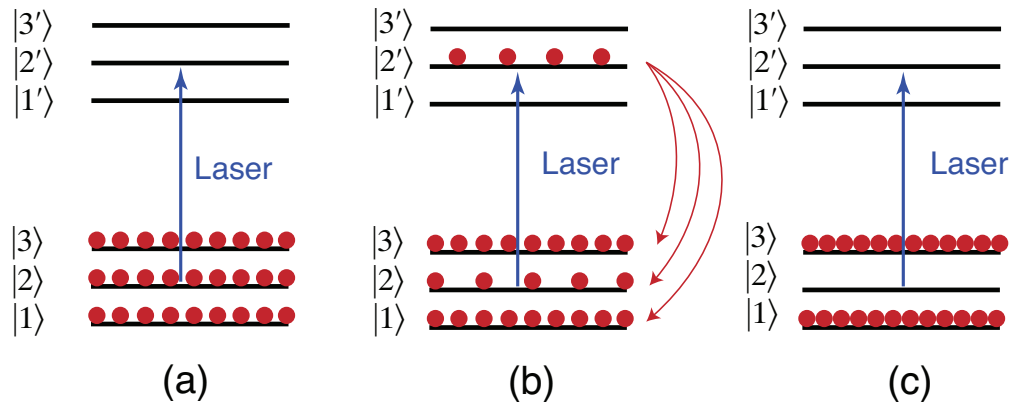


Figure 2.3. Spectral hole-burning process for an ion with three ground and excited spin-levels. (b) shows a transient hole where the hole lifetime is determined by the excited state decay time of the ions. (c) shows a permanent hole where the hole lifetime is determined by ground state lifetime of the ions. Difference between the energy levels are not to scale.

The hole lifetime depends on how fast the vacant ground state gets filled up. If the hole lifetime is limited by the excited state decay time, T_1 , it is called transient spectral hole burning. For Er-doped materials like $Er^{3+} : Y_2SiO_5$, $Er^{3+} : KTP$ and $Er^{3+} : Y_2O_3$, the ground state population goes to excited state forming a two-level system, and depending on the excited state decay time, those ions come back to those ground state. The excited-state lifetime of Er^{3+} ion in those materials is about 10ms in low temperature, so the lifetime of transient spectral hole burning is also around 10ms in those materials.

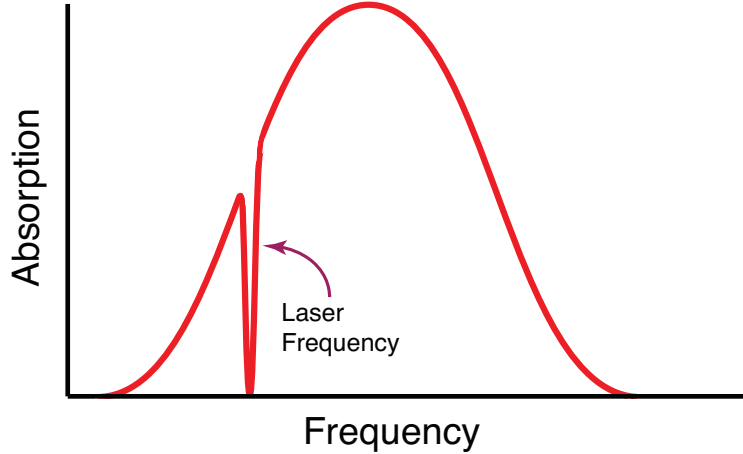


Figure 2.4. Probing a spectral hole in the inhomogeneously broadened absorption spectrum for an atomic ensemble.

The other kind of spectral hole burning (SHB) is the persistent SHB, where the hole lifetime is much larger than T_1 . For example, in Tm:YAG, there are hyperfine energy levels in the presence of a magnetic field. Therefore, the ions from one ground state can be transferred to the auxiliary states where the lifetime can be longer. In this way, moving from a two-level system to a three-level system, one can create persistent SHB if the lifetime of the auxiliary state is sufficiently high. For Tm:YAG, persistent hole lifetime can be from 10s seconds to hours.

The following section provides essential physical and chemical properties of rare-earth ions (REIs). The energy level structure in different solid hosts is also described.

2.4 Population lifetime

The atoms in the excited state decay to the ground state at an exponential rate without any external disturbance. The time constant for this exponential decay is defined as the population lifetime (T_1). It is possible to have multiple decay paths between excited and ground states, where the atoms go to the intermediate states before coming back to the ground states. We assign branching ratios as the relative probability for a particular decay path if multiple decay paths are a possibility. The lifetime of the excited state where it can decay via n path is defined as:

$$1/T_1 = \left(\sum_n \frac{1}{T_1(n)} \right)$$

Where $T_1(n)$ denotes the population lifetime of transition n .

2.5 Coherence time

Coherence time of an atom is defined as the inverse of its homogeneous linewidth (Γ_h):

$$T_2 = \frac{1}{\Gamma_h}$$

Coherence time is a significant quantity in quantum storage as it determines how long we can store the quantum information. Furthermore, coherence time is dependent on dynamic effects like spin-flip transition, phonon couplings, and even population decay time from an excited state to a ground state. Thus, the maximum limit of the coherence time is limited by the population lifetime of the ion, $T_2 \leq 2T_1$.

2.6 Cross relaxation

Many processes inside a solid-state medium are directly responsible for reducing coherence times and degrading optical properties. Therefore, it is essential to identify those so that it is possible to suppress them as much as possible for quantum applications.

2.6.1 Spin-Spin coupling

The first type of cross-relaxation discussed here is spin-spin coupling. In this process, energy and angular momentum are exchanged between ions. In this thesis, the rare-earth ion concentration was carefully chosen to minimize cross-relaxation. The most prominent cross-relaxation is magnetic-dipole interaction. If we increase the concentration of the ions, the direct spin exchange is possible due to the overlap of dopant wavefunctions. All these processes are resonant as total energy is conserved. There can be situations where transition energies between two ions are different. In that case, they have to rely on additional sources to make these transitions happen. In YSO crystal, this three-body process occurs because

of the abundance of nuclear spin 1/2 Y ions. This magnetic-dipole-assisted cross-relaxation is dependent on the distance between the ions as r^{-3} . So, low doping in crystal hosts is preferred in quantum applications, especially in building quantum memories.

It is also essential to consider the cross-relaxation outside the dopant ions. It is vital to choose a good host to maximize the coherence properties. In YSO and Si, there is 5% abundance of nuclear spin 1/2 ^{29}Si . A rapidly fluctuating magnetic field is created when ions with nuclear spin cross relax with each other. This is generally the limiting factor of coherence times in some rare-earth ion hosts. Much research has been done with ultra-low temperatures and high magnetic fields to suppress these noises effectively.

2.6.2 Spin-Lattice coupling

Spin-Lattice coupling or phonon coupling is the transfer of energy between the crystal's vibrational modes and the doped ions. Inside the crystal, there are ions and positive charges present. Different vibrational modes of the crystal can generate oscillatory electric and magnetic fields. Phonons are defined as discrete energy of these oscillatory fields. These phonons can be absorbed or generated by the ions during other transitions. Because phonons have non-zero energy, all the transitions assisted by spin-lattice couplings are non-degenerate.

In case of spin-lattice coupling, the probability a particular transition affected by it largely depends on temperature. The density of phonons of a particular energy can be described by Planck distribution:

$$\rho_{ph}(\omega) = \frac{3\hbar\omega^3}{2\pi^2\nu^3} \frac{1}{\exp(\frac{\hbar\omega}{kT}) - 1}$$

Special care is usually taken to reduce the availability of phonons of a particular energy. For example, the energy difference between Kramers doublet transition is in GHz at 4K for a magnetic field of 100s of mT. This energy gap can be as high as THz with a high enough magnetic field. In this energy gap, phonon transitions are generally quite common. That is why rare-earth-doped crystals usually are kept in very low temperatures with high magnetic field for quantum applications to reduce the phonon-assisted transitions. Low temperature reduces the available phonons and high magnetic field increases the energy gap

between Kramers doublet transition. Both of these effect helps to reduce the phonon-assisted transitions.

2.6.3 Multi-phonon processes

We have primarily discussed the transitions where a single phonon was responsible. But, in reality, in crystal host, multi-phonon processes do occur. The most common of these are the Raman process. In this process, a continuum of low-energy phonons is formed. It can be described as $\hbar\omega_{vir} = \hbar(\omega_1 - \omega_2)$, where ω_{vir} is the virtual phonon and ω_1, ω_2 are the frequencies for the thermal phonons.

Another multi-photon process is the Orbach process which is the resonant transition assisted by more than one phonon. For example, if we have phonons with frequency ω_1, ω_2 , then for this process to happen, the energy difference between two allowed transitions must be precisely matched.

3. INTERACTION OF LIGHT WITH RARE EARTH IONS

In 1899, Max Planck proposed that light must be quantized to explain the blackbody radiation, giving birth to quantum optics. According to quantum mechanics, electromagnetic waves consist of discrete energy packets termed photons. Atom-light interaction can be expressed by quantizing light or electromagnetic waves.

A two-dimensional state space can describe the quantum system of a 2-level atom spanned by atomic excited state $|e\rangle$ and atomic ground state $|g\rangle$. These two state vectors form the complete orthonormal basis in the 2D Hilbert space. The Rabi model was one of the first semi-classical theories to describe the atom-light interaction. Rabi model works for a closed system and single-mode EM waves. It takes account of the two-level atom and a continuous EM field. The model can be solved by time-dependent perturbation theory. Rabi model can successfully show the oscillations of probability to find the atom in excited state and ground state if we excite the atom with EM waves. However, as this model assumes classical EM field, vacuum oscillation and other quantum phenomena (spontaneous emission, etc.) can not be shown.

The next improvement of this theory comes from the Jaynes-Cummings model, which is a quantum model [13]. It assumes the EM field as quantized excitations. Quantum phenomena like vacuum rabi oscillation, spontaneous emission, collapse, and revival of oscillations can only be explained by this model. Below are some derivations for light-atom interactions that can be helpful to understand the next chapters in this thesis [14], [15].

3.1 Interaction of a two-level atom with a single mode light field

In this section, we want to explore the interaction of a two-level atom with a single mode light field. The derivations are presented in the Schrodinger picture. Here $\hat{\rho} = \sum_j p_j |\psi_j\rangle\langle\psi_j|$ denotes the density operator, the coefficients p_j are non-negative and add up to one, and $|\psi_j\rangle\langle\psi_j|$ is an outer product of the wave-functions (atomic and optical) of the system written in bra-ket notation. The time evolution of the density matrix can be expressed as:

$$\frac{\partial}{\partial t}\hat{\rho} = \frac{1}{i\hbar}[\hat{H}, \hat{\rho}] \quad (3.1)$$

where total Hamiltonian is $\hat{H} = \hat{H}_R + \hat{H}_{at} + \hat{H}_{int}$. Here we are ignoring the irreversible decay processes and focusing on reversible evolution of the density matrix. The first component of the total Hamiltonian, \hat{H}_R is due to the light field from laser modes \hat{a}_k and can be represented as:

$$\hat{H}_R = \sum_k \hbar\omega_k(\hat{a}_k^\dagger\hat{a}_k + 1/2) \quad (3.2)$$

For a single mode light field, we can write:

$$\hat{H}_R = \hbar\omega(\hat{a}^\dagger\hat{a} + 1/2) \quad (3.3)$$

and the second component of the total Hamiltonian, \hat{H}_{at} for a single two-level atom is expressed as:

$$\hat{H}_{at} = \hbar\omega_{at}\hat{\sigma}^\dagger\hat{\sigma} \quad (3.4)$$

The third component of the total hamiltonian, \hat{H}_{int} is called the interaction Hamiltonian which describes the interaction of light with atoms. This interaction Hamiltonian describing the interaction of single mode light field and a single atom can be expressed as:

$$\hat{H}_{int} = \hbar g(\hat{\sigma} + \hat{\sigma}^\dagger)(\hat{\mathcal{E}} + \hat{\mathcal{E}}^\dagger) \quad (3.5)$$

where $\hat{\mathcal{E}} = \int \hat{a}_k e^{-ikz} dk$ is the optical mode interacting with the atoms. Here, g is the vacuum Rabi frequency and assuming g is the same for all k modes, it can be expressed as:

$$g = d\sqrt{\frac{\omega}{2\epsilon_0 V \hbar}}$$

Here ϵ_0 is vacuum permeability, V is the quantized volume, ω is the transition frequency and d is the atomic transition dipole moment. The oscillation frequency of $\hat{\sigma}\hat{\mathcal{E}}$ and $\hat{\sigma}^\dagger\hat{\mathcal{E}}^\dagger$ are twice as fast as the atomic transition frequency. So, while calculating the interaction hamiltonian,

these terms can be neglected as they are responsible for far off-resonant excitations. We can obtain the Jaynes-Cummings Hamiltonian in this form with rotating wave approximation:

$$\hat{H}_{int} = \hbar g(\hat{\sigma}\hat{\mathcal{E}}^\dagger + \hat{\sigma}^\dagger\hat{\mathcal{E}}) \quad (3.6)$$

Now, I will briefly describe the reversible evolution of the density matrix [15]. The assumption made here is that the atom is excited by coherent radiation modes. To get the evolution of the averaged atomic modes, we need to take the trace over the atomic variables:

$$\langle\hat{\sigma}_{12}\rangle = Tr_{at}(\hat{\rho}\hat{\sigma}) \quad (3.7)$$

$$\langle\hat{\sigma}_{11}\rangle = Tr_{at}(\hat{\rho}\hat{\sigma}^\dagger\hat{\sigma}) \quad (3.8)$$

$$\langle\hat{\sigma}_{22}\rangle = Tr_{at}(\hat{\rho}\hat{\sigma}\hat{\sigma}^\dagger) \quad (3.9)$$

where $\hat{\sigma}_{12}$ describes the atomic coherence and $\hat{\sigma}_{11}, \hat{\sigma}_{22}$ describes the ground state and excited state atomic populations respectively. From equation 2.1 and applying the cyclic properties of trace, the following equations of motion can be derived (ignoring the irreversible decay processes):

$$\frac{d}{dt}\langle\hat{\sigma}_{12}\rangle = i\omega_{at}\langle\hat{\sigma}_{12}\rangle + ig\hat{\mathcal{E}}(\langle\hat{\sigma}_{11}\rangle - \langle\hat{\sigma}_{22}\rangle) \quad (3.10)$$

$$\frac{d}{dt}\langle\hat{\sigma}_{11}\rangle = ig(\hat{\mathcal{E}}^\dagger\langle\hat{\sigma}_{12}\rangle - \hat{\mathcal{E}}\langle\hat{\sigma}_{21}\rangle) \quad (3.11)$$

In the situation where the laser power is small and well below the saturation of the atomic absorption, the excited state population $\langle\hat{\sigma}_{22}\rangle$ will be negligible. In this case, the time evolution of optical coherence can be written as:

$$\frac{d}{dt}\langle\hat{\sigma}_{12}\rangle \approx -i\omega_{at}\langle\hat{\sigma}_{12}\rangle + ig\hat{\mathcal{E}} \quad (3.12)$$

These equations are obtained when decay processes are ignored. To include non-unitary operations one needs to write mater equation. Also one needs to include spatial dependency and Maxwell equations. More complete derivation will be provided in chapter 5 and chapter 6 where specific systems such as photonic micro-ring resonators and standing waves inside a crystal are discussed. The equations needed to be modified according to the particular system we wanted to explore.

3.2 Atom light interactions inside cavity

Light-atom interactions inside a cavity are of great research interest because of the increased interaction probability of atoms with light, and it also allows different non-linear processes. The cavity allows a strong coupling regime where a coherent transfer of excitations is possible from light to matter and vice versa. It also modifies the emission rates responsible for superradiance, lasing, and other co-operative emissions.

This section defines some of the critical cavity parameters used frequently in this thesis.

3.2.1 FSR and Finesse

In an optical resonator, free spectral range (FSR) is defined as the spacing of the resonator modes. In the case of vacuum standing wave resonator of length L , the FSR is defined as:

$$\delta\nu = \frac{c}{2L} \quad (3.13)$$

where c is teh velocity of light in vacuum. If the light passes through an dispersive medium, the FSR is defined as:

$$\delta\nu = \frac{c}{2n_g L} \quad (3.14)$$

Where n_g is the group index of the medium.

The finesse of an optical resonator is defined as the FSR divided by the bandwidth of the resonances:

$$F = \frac{c/(2n_g L)}{\Delta\nu} \quad (3.15)$$

3.2.2 Quality Factor and Mode Volume

The Quality factor of a cavity measures how good the cavity is in storing the energy. The cavity Q can be defined as:

$$Q = 2\pi \frac{\text{Optical Energy stored in the cavity}}{\text{Optical energy lost in one cycle of oscillation}} \quad (3.16)$$

which in turn can be expressed as:

$$Q = 2\pi\nu_0 \frac{\text{Optical Energy stored in the cavity}}{\text{Rate of Optical energy loss from cavity}} \quad (3.17)$$

This definition can be simplified in terms of known parameters where we can get:

$$Q = \frac{\nu_0}{\Delta\nu} \quad (3.18)$$

Where $\Delta\nu$ denotes the FWHM of the optical resonance.

The mode volume (V) is a measure of the spatial confinement of the electromagnetic radiation. Smaller mode volume is preferred to increase the interaction probability of light with atoms.

3.2.3 Purcell Factor

The spontaneous emission rate enhancement of an atomic system by manipulating its environment is defined as the Purcell effect. The enhancement factor is the Purcell Factor, F_p , which is the ratio of enhanced spontaneous emission rate and natural, spontaneous emission rate.

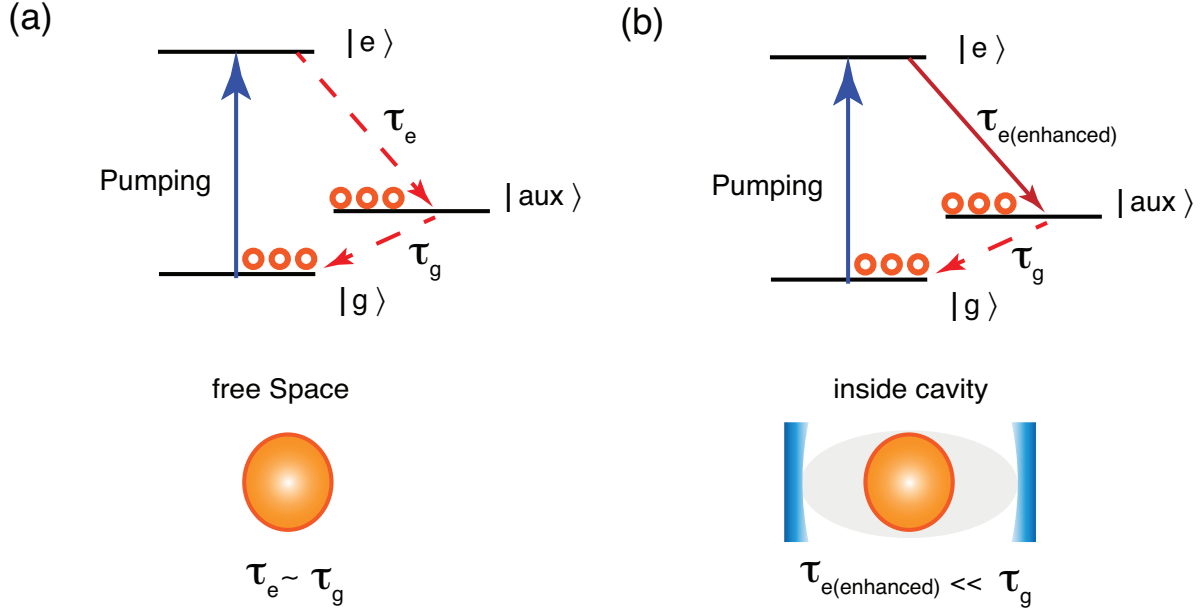


Figure 3.1. Schematic diagram of the enhancement of spontaneous emission rate due to cavity.

For a cavity with quality factor Q and mode volume V , the Purcell factor can be calculated with this formula:

$$F_p = \frac{3}{4\pi^2} \left(\frac{\lambda}{n}\right)^3 \left(\frac{Q}{V}\right) \left(\left|\frac{E_{ion}}{E_{peak}}\right|\right)^2 B_r \quad (3.19)$$

where λ is the resonant wavelength of the ion, n is the refractive index of the cavity material, $\left(\left|\frac{E_{ion}}{E_{peak}}\right|\right)^2$ denotes the electric field overlap and B_r denotes the branching ratio of the ion transition.

It can be seen that to get higher Purcell enhancement, the quality factor Q should be increased, and the mode volume V should be as small as possible. In the figure 3.1 we have a schematic diagram showing the difference in excited state lifetime with and without a cavity. If the ion is inside the cavity, the excited state lifetime can be reduced considerably, resulting in a higher photon emission rate.

But in the case of rare-earth ions inside the cavity, we must be cautious about the homogeneous linewidth of the ions themselves. We can see in the 3.2 figure there can arise two situations. Figure 3.2(a) shows the case where emitter homogeneous linewidth is much

less than cavity linewidth. In this case the general formula of Purcell factor can be applied, where $P \propto \frac{Q_{cav}}{V_{mode}}$.

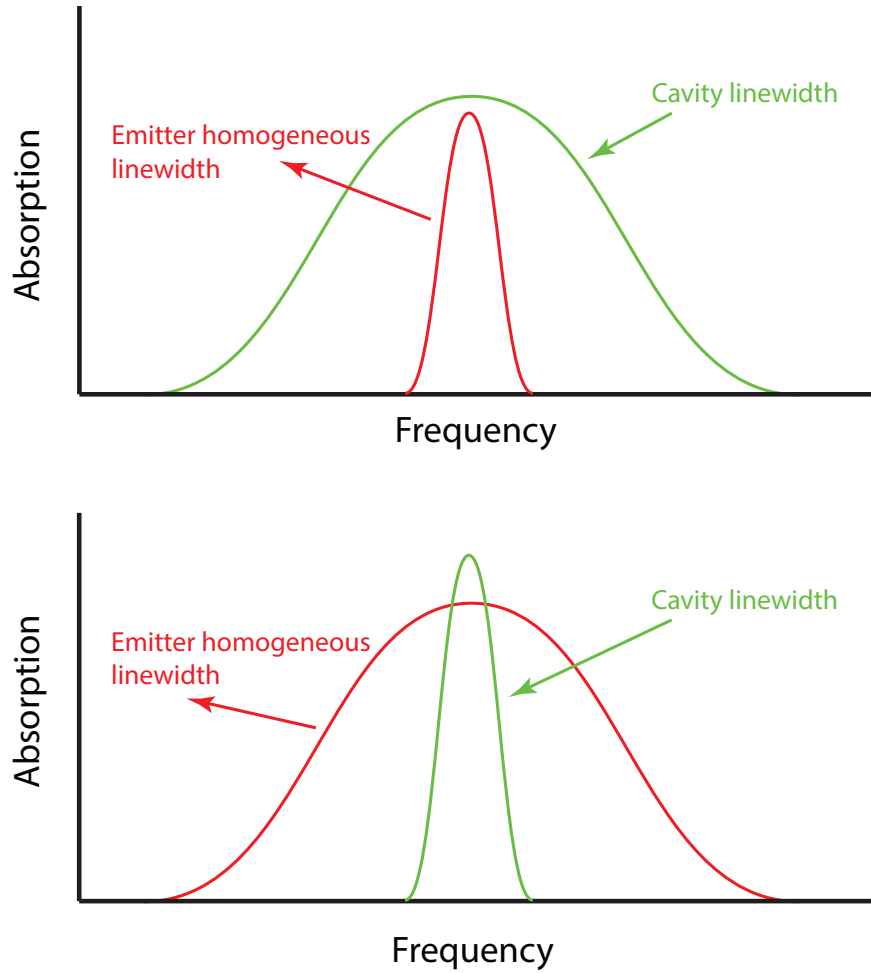


Figure 3.2. Schematic diagram of the two situations for rare-earth ions inside the cavity. (a) In this case, the emitter homogeneous linewidth is much less than cavity linewidth. (b) Here, the emitter homogeneous linewidth is much greater than cavity linewidth.

But for the second case, which is shown in figure 3.2(b), we can see that the emitter homogeneous linewidth is much greater than cavity linewidth. So, in this case, we have to adjust the formula of the Purcell factor by replacing the quality factor of the cavity with the quality factor of the emitter itself, $P \propto \frac{Q_{em}}{V_{mode}}$. Here, the Q_{em} is defined as the ratio of emitter transition frequency with the homogeneous linewidth of the emitter.

3.3 Optical Quantum memory with rare-earth ions

A device that can store and retrieve arbitrary quantum states of light can be considered quantum optical memory. Ideally, it should store and preserve quantum properties of light with memory retrieval fidelity exceeding the classical limit. Quantum memories are crucial for quantum repeater architectures that allow long-distance quantum communications to overcome fiber loss. Another beneficial application of quantum memory is transforming a probabilistic single-photon source towards a deterministic source of single photons, which can be extremely useful for different quantum applications.

An optical quantum memory reversibly maps the photons onto long-lived coherent excitations. There has been much research devoted to realizing an efficient quantum memory. Rare-earth ions doped or implanted in host crystals at very low temperatures and high magnetic fields can have highly coherent quantum states in their valence orbital. For that reason, rare-earth ions in crystalline hosts have been identified as attractive media for quantum optical applications where record-high coherence times, quantum storage efficiency in solids, and quantum storage bandwidth have been demonstrated. Among rare-earth ions, Erbium uniquely possesses optical transitions at $1.5 \mu m$ region, making it suitable for fiber telecommunication and silicon photonics.

In this section, I am reviewing different storage protocols that are especially popular in rare-earth quantum memories and used in this thesis for later experiments. More in-depth discussions can be found here [16], [17].

3.3.1 Controlled Reversible Inhomogeneous Broadening

In the Controlled Reversible Inhomogeneous Broadening (CRIB) process, the first step is to dephase the atomic polarization by an external field. In this way, an incoming light pulse is stored into the collective states of the atomic ensemble. In the next step, a reversal of the applied field is applied, which rephases the atomic polarization. This rephasing results in a reemission of the light. CRIB utilizes the inhomogeneous broadening of the transition and uses a non-optical method to time-reversed the absorption process.

For the CRIB protocol, different approaches are followed. The first CRIB protocol was developed for impurities embedded in solid-state systems, also known as transverse CRIB. Because of a transverse field gradient, different shifts of the dipole moments were observed due to an externally applied field. Therefore, the direction of the field is reversed in the next step. This causes dipole moments to shift in the opposite direction leading to reversing of the dephasing process (rephasing). This rephasing causes an emission of light termed an echo. Different approaches were also proposed in subsequent years, including the longitudinal CRIB approach. In this approach, the dipole moment shift depends on the dipole's position in the solid medium. Theoretical efficiency for this memory protocol can be as high as 100% given that atoms have very high coherence time and the system with high optical depth. However, the efficiency limit for transverse CRIB is limited to 54%.

3.3.2 Atomic Frequency Comb

In Atomic Frequency Comb (AFC) storage protocol, a pulse of light is absorbed by an atomic Frequency Comb. If the intertooth spacing of the AFC is Δ , then the light will come out of a time, $t = 2\pi/\Delta$. A frequency selective optical pumping can create a comb-like absorption profile if an atomic medium has large inhomogeneous bandwidth. This is why rare-earth ions are a popular choice as a storage medium in this protocol as they have large inhomogeneous broadening and long coherence time.

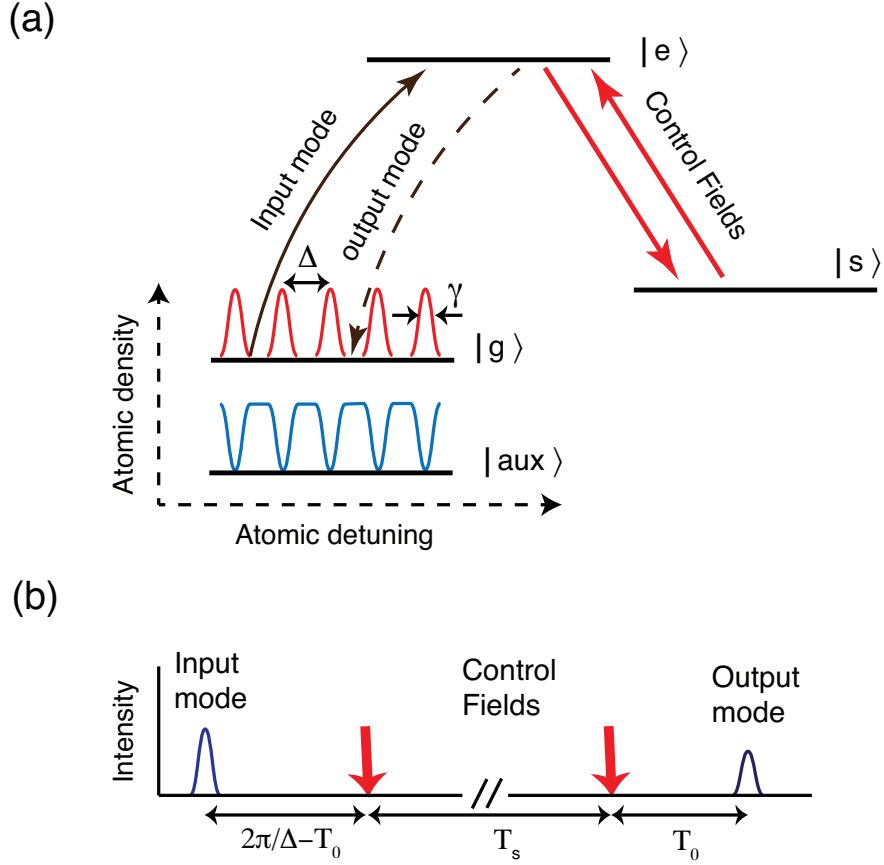


Figure 3.3. Schematic diagram of Atomic Frequency Comb (AFC) storage protocol. (a) shows an atom with an excited state $|e\rangle$, which is connected to two lower states $|g\rangle$ and $|s\rangle$. (b) shows input light is stored and comes out as an echo after a time $t = 2\pi/\Delta$.

Let's assume the storage medium consisting of an ensemble of ions has an excited state $|e\rangle$, which is connected to two lower states $|g\rangle$ and $|s\rangle$ as seen in figure 3.3. With frequency-selective pumping, the $|g\rangle - |e\rangle$ transition is spectrally shaped. The atomic density function looks like a comb and has a series of narrow peaks of linewidth γ separated by distance Δ spanning a large frequency range. Hence, the spectrally shaped atomic density function is called the atomic frequency comb.

The light pulse that needs to be stored should have linewidth γ_p larger than the AFC peak spacings Δ . To store efficiently, γ_p also needs to be smaller than the whole frequency range spanning AFC. Ideally, then input light can be absorbed by the AFC. This light is

stored as a single excitation in the AFC over all the atoms resonant with the photon. The atomic ensemble forms a collective state, also known as the Dicke state.

This collective state is formed by a coherent excitation of the AFC modes by the incoming photons. This collective state has a detuning of $\delta_i = n_i \Delta$, where n_i are integers and Δ is the AFC spacing. After the initial excitation, the collective state starts to dephase. The rephasing happens after a time, $t = 2\pi/\Delta$, which results in coherent reemission of light in a forward direction similar to the photon-echo process. The theoretical limit of AFC storage efficiency is 54% which is limited by the reabsorption process. Later it was suggested that the reemission could be forced to move backward, and in this case, the efficiency limit can be as high as 100% for proper phase-matching conditions.

The described process is a quantum storage protocol with a fixed storage time $t = 2\pi/\Delta$. Some modifications are implemented to transform it into on-demand quantum memory to make it more useful. An optical control field is applied from state $|e\rangle$ to $|s\rangle$ for this to happen. In the $|s\rangle$ state, it is stored as a collective spin state. Because this does not have a comb structure, it will not generate an echo after a fixed time. Another control field needs to be applied to get the echo, reversing from $|s\rangle$ to $|e\rangle$ to move the excitation back to the original place after a time T_s . Now an echo will come out but after a time of $t = T_s + 2\pi/\Delta$. As we can control the time T_s , this AFC storage protocol becomes an on-demand quantum memory.

4. EXPERIMENTAL TECHNIQUES

This chapter describes the instruments and techniques used for setting up the experiments. The first section discusses the main components of the low-temperature setup. One of the most challenging parts was to bring the sample to a very low temperature. Then briefly, the fiber-to-chip coupling techniques are discussed. Section 2 illustrates single-photon detection methods and the software used to analyze the data. In section 3, photon echo measurement techniques are discussed, which was crucial to knowing the quantum emitters' coherence properties. The following section discusses optical modulation and homodyne and heterodyne measurement.

4.1 Low temperature measurements



Figure 4.1. Cryogenic setup by Montana Instruments.

We used a cryogenic setup (cryostation - Standard (s) Series) provided by Montana Instruments for low-temperature measurements. The cryogenic system can be integrated with the sample and control the temperature and vacuum parameters of the whole system. It comes with different parts, including a system control unit, vacuum control unit, and helium compressor. It allowed the samples to go to as low as 3.2K temperature.

In Fig.4.1, we can see the cryogenic setup integrated with the optical imaging system to study the sample at low temperature. Inside the chamber, a mechanical pump is attached, which pumps out the air to create a vacuum.

The actual cooling happens by a two-stage Gifford-McMahon cryocooler. We isolated the cryocooler mechanical vibrations from the sample and optical alignments by a vibration-damping support structure. In addition, there is a separate helium compressor that provides the necessary helium for the closed-loop cooling cycle.

4.1.1 Sample chamber

The sample chamber is the integrated platform for the sample mount assembly, a radiation shield surrounding the sample, and outer vacuum housing with windows.

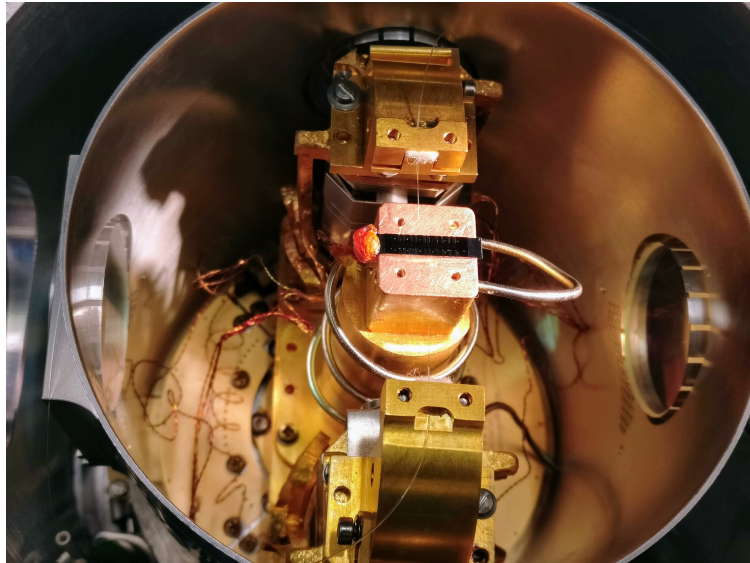


Figure 4.2. Sample chamber inside the Cryogenic setup.

A thermometer is attached to the platform and the sample holder to display the temperature at all times correctly. If the temperature does not go to the desired temperature, then there can be several reasons, including leaks, out-gassing by some object, or saturation of charcoals that absorbs gas molecule.

Extra care has been taken to reduce the thermal fluctuation using both active and passive techniques. In the fig.4.2, the sample chamber can be seen where a silicon nitride chip with a micro-ring resonator in it is mounted. A vacuum-compatible thermal grease has been used to have good thermal contact between the sample platform and the sample. To fix the position of the sample, a low-temperature compatible varnish has been used. Once the position of the sample is fixed, the optical fiber alignment is done by the nano-positioners, which are described in the next section.

4.1.2 3D nano-positioners for fiber-to-chip coupling

We have used 3D nano-positioners by Montana instruments to precisely move the optical fibers for high-precision alignment. The light fiber-to-chip coupling is very sensitive to the alignment, and precise, controlled movement of the optical fiber is necessary. We successfully installed this 3-axis (XYZ) piezo-driven, slip-stick style nano-positioners, controller, and flexible thermal links so that the sample temperature always remains as expected. The motion range for these nano-positioners was 5mm on each axis which was enough for the high-precision alignment.



Figure 4.3. Controller for 3D nano-positioners for high-precision alignment for fiber-to-chip coupling.

In the above fig. 4.3 we can see the Controller for 3D nano-positioners. The movement of the stage can be done in step size or continuous mode.

4.2 Single photon detection

One of the most critical aspects of this thesis is to detect very small optical signals. To do this, a single-photon detector is needed. We used PDM-IR from Micro Photon Devices (MPD) in our lab. This photon counting module is an InGaAs/InP Single-Photon Avalanche Diode (SPAD) specialized for detecting near-infrared single photons within wavelength range 1100nm to 1600nm. It is integrated with a programmable frequency and pulse generator for gating the detector. It also has a front-end circuit for photodetector's avalanche sensing and a fast circuit for detector's avalanche current quenching. All the primary parameters can be selected according to the use case with the software.



Figure 4.4. Single Photon Avalanche Detector Module from MPD.

In fig. 4.4 we can see the SPAD detector used for detecting minimal signal. It produces a clean temporal response of the arrival photons. For this reason, it can be used for both counting and timing measurements. For better analyzing the data, we used the Timeharp interface. The TimeHarp software helped us with different measurement parameters and visualized the result in a more understandable version. The most crucial measurement characteristics such as count rate, count maximum, and position, histogram width (FWHM) can be seen continuously with this software.

4.3 Photon Echo and Spin Echo

For a two-pulse photon echo experiment, the sample is excited by two pulses of strong laser light separated by a time delay, τ . The first pulse, also known as the $\pi/2$ pulse, is responsible for creating a coherent superposition of ground and excited state. Because of this coherence, the sample can be seen as a macroscopic oscillating dipole moment. Because of the inhomogeneous broadening present in the sample, there is a spread in the transition energies of the ions. As time evolves, this spread in transition energies creates different relative phases, which results in a loss of coherence. The second pulse, known as the π pulse, does population inversion, which exchanges the phases of the ground and excited states. This exchange results in a negative sign of the accumulated phases of the in-homogeneously broadened states which reverses the dephasing or causes the rephasing. As seen in the figure 4.5 after the second pulse at time delay, τ later the rephasing of the ions completes with no relative phase among ions. Once again, we have the macroscopic oscillating dipole, which emits a burst of radiation termed as photon echo.

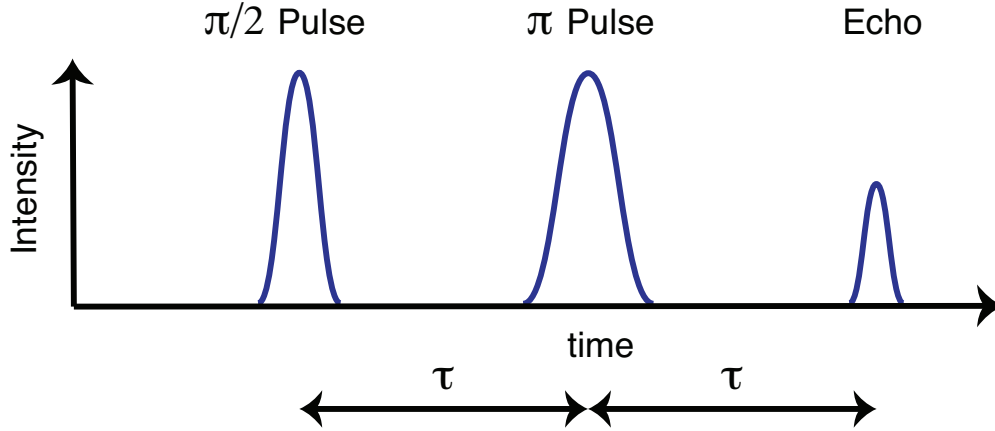


Figure 4.5. Schematic diagram of the 2 pulse photon echo process.

The echo intensity decays exponentially with delay time τ between the two pulses. Also, the echo intensity depends on the coherence property of the ions, and the coherence time (T_2) is measured by fitting the echo intensity to delay time τ . As we know, dephasing happens because of static and dynamic effects related to homogeneous and inhomogeneous broadening. But, the dephasing effect due to the static effects cancels out because of the pulse sequence. So, the photon echo decay rate tells us about the dynamical processes that cause the dephasing related to the homogeneous broadening. The homogeneous linewidth (Γ_h) can thus be calculated from the coherence time T_2 , by this formula $\Gamma_h = 1/(\pi T_2)$. This is a beneficial technique to measure the very narrow homogeneous linewidth even with a laser with broader spectral linewidth.

In this thesis, I have measured coherence time using the photon echo decay method of 0.005% doped Er:YSO crystal to be at $1.5\mu s$ at 3.5K. So, in that crystal, the homogeneous broadening of Er was $\sim 200KHz$ at 3.5K.

4.4 Homodyne and Heterodyne detection

The primary purpose of homodyne and heterodyne is to extract information encoded as modulation of phase-frequency or both. In this detection process signal is compared with standard or reference light coming from a local oscillator.

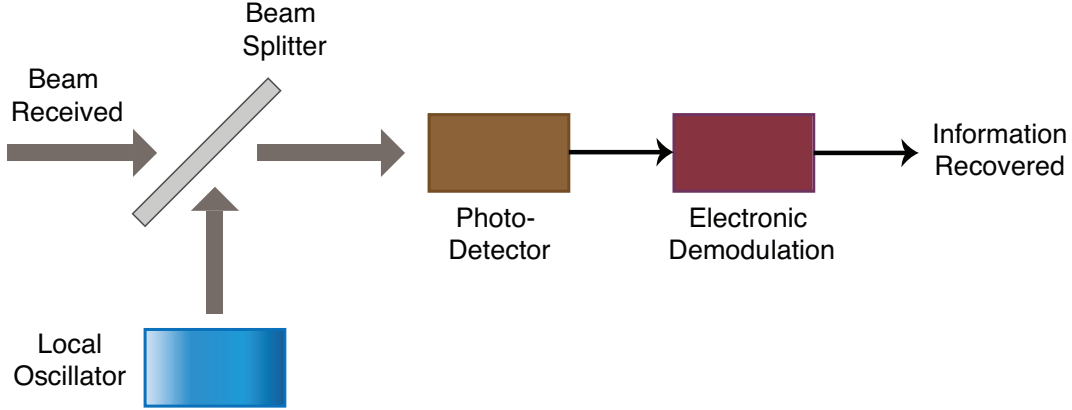


Figure 4.6. Schematic diagram of the experimental setup for heterodyne detection.

In the figure 4.6, we can see the schematic diagram showing the experimental setup for heterodyne detection. In this process, the reference signal coming from the local oscillator is mixed with the signal by a beam splitter, and then the combined signal is detected by a photodetector. Now, if we do electronic demodulation, we can extract the information about the actual signal.

The main advantage of homodyne and heterodyne detection is the gain in the detected signal. The larger the local oscillator amplitude is, the larger the gain in the detected signal will be. This relation can be easily seen by this equations:

$$I \propto [E_{sig} \cos(\omega_{sig}t + \phi) + E_{LO} \cos(\omega_{LO}t)]^2$$

$$I \propto \frac{1}{2}E_{sig}^2 + \frac{1}{2}E_{LO}^2 + 2E_{sig}E_{LO}\cos(\omega_{sig}t + \phi)\cos(\omega_{LO}t)$$

Where E_{sig} , E_{LO} are the electric field amplitude of the signal and local oscillator, respectively, if we see the last term, it does have the phase information of the signal as well as it got multiplied by the local oscillator amplitude. So, this kind of detection is beneficial for sensitive measurements as the linewidth of the modulated signal is much smaller than the optical linewidth of the signal or local oscillator. So, tiny shifts in the signal's center frequency can be measured with this technique.

In the homodyne measurement, the local oscillator and the signal have the same frequency, whereas those frequencies are different for the heterodyne measurement.

One problem for heterodyne measurement is the shot noise keeps on increasing as we increase the power of the local oscillator. So, then the signal-to-noise ratio is limited by shot noise. For this reason, balanced detection is preferred where a beam splitter is used to divide the signal and local oscillator equally into two detectors. Then, the difference between these two detectors is not influenced by the local oscillator noise.

5. THEORETICAL INVESTIGATION OF INTERACTION OF LIGHT WITH ATOMIC ARRAY

Portions of this chapter have been previously published: Keiichiro Furuya, Arindam Nandi, and Mahdi Hosseini. **“Study of atomic geometry and its effect on photon generation and storage.”** Optical Materials Express 10.2 (2020): 577-587. This is a collaborative project and my colleague Keiichiro Furuya has significant contribution on developing the theory discussed in this chapter.

The study of collective excitations in atomic ensembles is an important research topic aiming to advance our understanding of many-body dynamics in quantum systems [18], [19]. The framework for such study was initially formulated by Dicke [20]. It has been shown that photons can mediate the interaction between atoms confined in sub-wavelength regions in free space[21], [22] or near optical resonators or waveguides[23], [24]. The Raman excitation triggering collective excitations can also give rise to superradiant-type emission from extended ensembles, $V > \lambda^3$. The nonlinearity can be introduced to the emission process by the projective measurement leading to generation of correlated photons. The bi-photons created in this way has been the center of research for quantum state engineering as a viable approach for entanglement distribution[25]. The spin of an ensemble of atoms, spontaneously emitting photons upon off-resonance excitation with a pump, can be projected into a single collective excitation when a single photon is detected in a pre-defined spatial mode. The collective excitation can give rise to the emission of a correlated photon through an inverse Raman process. This approach has been used to entangle four quantum memories[26] and generate multi-dimensional correlated photons[27]. Recently, effect of atomic distribution near waveguides[24], [28] and cavities has been investigated as a way to control photon emission and propagation through the waveguides. The system which atoms are placed inside or nearby a ring cavity is one of the popular ones to explore general dynamics in 1D and 2D quantum physics.

5.1 Introduction

In this chapter, we consider atomic geometry as a control knob to suppress loss and noise in the process of photon generation and storage from an ensemble of emitters or photons. We show that by precision manipulation of position of atoms, forming a periodic or an aperiodic lattice, chiral photon emission can be achieved to enhance correlation between the photons. Our approach can be used to describe and enhance photon generation processes from various emitters[29], including neutral atoms, defect centers in solids, rare earth materials and quantum dots, for engineering active photonic materials[30] with novel application in quantum information.

5.2 Model: light interaction with a periodic lattice of atoms

We consider an array of atoms or emitters incorporated into an optical ring resonator as shown in Fig.5.1 (a). The atoms are distributed around the resonator with spacing between them chosen such that various collective behaviors emerge. The positions of the atomic segments are denoted by θ_j , as shown in Fig.5.1 (a). The distance ϕ_j , ($j = 1, 2, \dots, N$), on the ring is the spacing between j th and $(j - 1)$ th atomic segments. There should be a periodic condition on any distribution of atomic segments which is $\theta_N = 2\pi$.

The interaction Hamiltonian of the system is given in terms of atomic operators as

$$H_{int} = \sum_j \int \hbar/2\pi(g(\theta)(\hat{\sigma}_j/\sqrt{N})(\hat{a}_c^\dagger e^{ikr\theta} + \hat{a}_{cc}^\dagger e^{-ikr\theta}) + h.c.)d\theta \quad (5.1)$$

where $\hat{\sigma}_j = |g_j\rangle\langle s_j|$ is the atomic operator of j -th atoms, $g(\theta)$ is the coupling strength and $\hat{a}_{c/cc}$ is the operator for the field propagating in the clockwise (c) or counter-clockwise (cc) direction, respectively. Assuming equal light-atom coupling strength, $\mathbf{g} = g(\theta)$, at all discrete locations, we arrive at:

$$H_{int} = \hbar\mathbf{g}\{\hat{S}(k)\hat{a}_c^\dagger + \hat{S}(-k)\hat{a}_{cc}^\dagger + h.c.\} \quad (5.2)$$

where the collective atomic operator is defined as

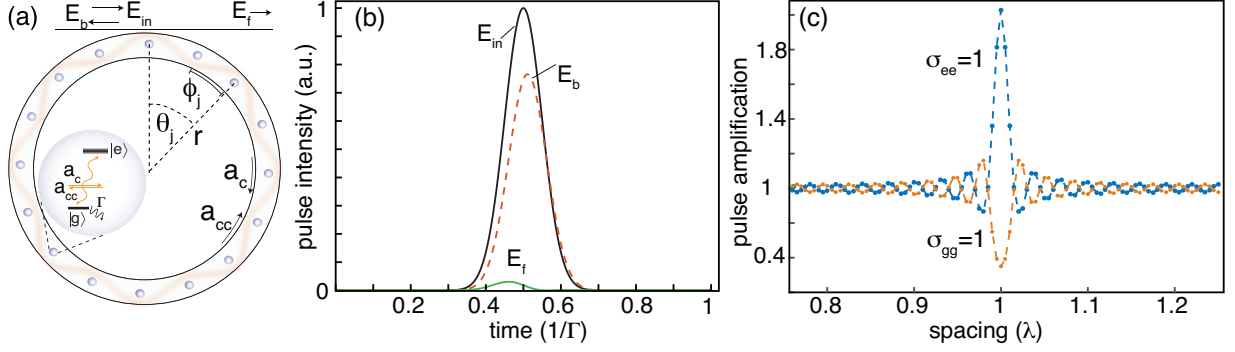


Figure 5.1. (a) A schematic of an optical ring resonator hosting an array of atomic segments forming a lattice commensurate with the emission wavelength resonant with the cavity. (b) The input (E_{in}), transmitted (E_f) and reflected (E_b) light intensities for a pulse propagating through the bus waveguide coupled to the resonator. An atomic lattice consists of 100 segments with spacing of λ is considered. (c) A pulse of light resonant with the resonator can be amplified or deamplified depending on the initial state of the atoms and atomic spacing. σ_{ee} and σ_{gg} denote the atomic population in excited state $|e\rangle$ and ground state $|g\rangle$, respectively. The simulation parameters used are : $g/\Gamma = 0.5$, $\delta\omega = 0$, $N = 15$ and propagation time $c/r\phi_j \ll 2\pi/\Gamma$ where c is the velocity of light in vacuum and r is the radius of the ring resonator.

$$\hat{S}(k) = 1/\sqrt{N} \sum_j e^{-ikr\theta_j} \hat{\sigma}_j, \quad (5.3)$$

and state $|g_1, g_2, \dots, s_j, \dots, g_N\rangle$ refers to the state with atom j excited to the level $|e\rangle$ while other atoms remain in the ground state $|g\rangle$. Here N denotes the total number of atomic segments in the ring resonator. Considering a single-pass propagation, the interaction dynamics can be obtained by numerically solving the semiclassical Maxwell-Bloch equations of motion. To this end, we write the time-dependent equations in Heisenberg picture and replace the operators with their mean values. We numerically solve the following equations:

$$\frac{d\hat{\mathcal{E}}_{c/cc}}{d\theta} = \pm i\mathcal{N}(\theta) \sum \hat{\sigma}_j \quad (5.4)$$

$$\frac{d\hat{\sigma}_j}{dt} = -(\Gamma + i\delta\omega)\hat{\sigma}_j - i\mathbf{g}(\hat{\mathcal{E}}_c^* + \hat{\mathcal{E}}_{cc}e^{2ikr\theta})(\hat{\sigma}_{gg} - \hat{\sigma}_{ee})_j \quad (5.5)$$

where $\hat{\mathcal{E}}_{c/cc}(\theta) = \hat{a}_{c/cc}e^{\mp ikr\theta}$ is the optical mode in the clockwise or counter-clockwise direction (see Fig.5.1). Also, $\hat{\sigma}_{ee/gg}$ is the atomic population operator, and Γ is the decoherence rate

between two levels $|g\rangle$ and $|e\rangle$. The inhomogeneous broadening of the atomic transition is described by light-atom detuning $\delta\omega = \delta\omega(\theta_j)$ for individual atoms. The atomic density around the ring is described by a top-hat function as

$$\mathcal{N}(\theta) = gr/4\pi c \sum_m (\tanh(\theta - m\phi_m + \delta\phi) - \tanh(\theta - m\phi_m - \delta\phi)) \quad (5.6)$$

with position uncertainty $\delta\phi$. By replacing operators with expected values of atomic, $\langle\hat{\sigma}\rangle = \sigma$, and optical, $\langle\hat{\mathcal{E}}\rangle = E$ fields, dynamics of the mean fields are achieved by integrating the equations over time and space. We numerically solve these equations using multi-dimensional differential equation solver (XMDS) [31] for various atom geometries.

The transmitted and reflected light intensity when a single pulse impinges on to the ring in the clockwise direction is shown in Fig.5.1(b). At high atom numbers, a significant portion of the incoming pulse is reflected due to the presence of an atomic Bragg resonance. The atomic resonances of this kind has been predicted [32]–[34] and observed using cold atoms near waveguides and fibers [28]. The total amplification and attenuation of the pulse as a function of lattice constant or atom spacing is also shown in Fig.5.1(c). The pulse can be amplified or attenuated depending on the initial atomic state and lattice spacing. The frequency of the oscillation in Fig.5.1(c) is $\lambda/2N$ resulting from the spatial interference of the E-field amplitude. At the atomic resonance condition, maximum interference occurs when the coherence length of photons is larger than the effective propagation length, or $\kappa > \gamma$, where κ and γ are decay rates of the cavity and excited atomic state, respectively.

5.3 Long-range cooperative light emission

The cooperative decay of an ensemble of emitters confined in a region much smaller than λ^3 has been predicted [35], [36] and experimentally observed in various platforms[21]–[24]. In a solid state environment, the presence of disorder such as inhomogeneous broadening is responsible for simultaneous appearance of sub and superradiant emission modes [37], [38]. Moreover, it is known that atomic distribution affects the cooperative emission [38], [39].

For observation of superradiance inside a cavity, the resonator decay rate, κ , must be large enough such that the intra-cavity photons leave the cavity before being reabsorbed by

the atoms or before atoms decohere. Thus, the interactions need to be in the limit where $\kappa \gg \gamma + \Gamma$, and also the decoherence rate Γ should be less than the cooperative decay rate, $N\gamma$, where N is the effective atom number contributing to the emission. The atomic lattice interacting via the intra-cavity light can exhibit mesoscopic cooperative interactions where cooperative coupling is extended to regions beyond the wavelength scale. Inside the resonator, the time evolution of the optical field, \hat{a}_c , in the clockwise direction is described by:

$$\frac{d\hat{a}_c}{dt} = -\kappa\hat{a}_c + ig\tilde{\sigma} + \sqrt{\kappa/\tau}a_{in} \quad (5.7)$$

where a_{in} represents the incoming field, τ is the round-trip time of photons inside the ring, and $\tilde{\sigma} = \langle \int \mathcal{N}(\theta)(\sum_j \hat{\sigma}_j) d\theta \rangle$.

Figure 5.2(a) shows the numerical solution to the pulsed emission from an ensemble of two-level atoms initially prepared in the excited state. In this regime, the pulse envelope has a width inversely proportional to the atom number, N , and its peak intensity scaling with N^2 . The coherent emission is captured by the atomic coherence built up (σ_{eg}) shortly after atoms are initially prepared.

The scaling of peak intensity is evident in Fig. 5.2 (b). As expected, the intensity increases quadratically with atom number beyond a threshold atom number (needed to overcome decoherence). We note that these results are also valid for the case where instead of one atom per site, an ensemble of N_0 atoms are localized ($r\delta\phi \ll 1$) per segment. In such case, $g \rightarrow g\sqrt{N_0}$ and $r\delta\phi$ represents the atomic distribution per site. As the atoms are delocalized with respect to the cavity anti-nodes' position, $r\delta\phi > 0$, superradiance becomes less evident and a larger threshold is needed to overcome disorder. In presence of inhomogeneous broadening, with width of Ω , the requirement for the observation of cooperative decay is more stringent. The necessary condition for observation of superradiance then becomes $\Omega/N \ll \gamma$. With a resonator with a linewidth $\kappa < \Omega$, the effect of inhomogeneous broadening to cooperative emission can be evaluated by considering an effective atom number

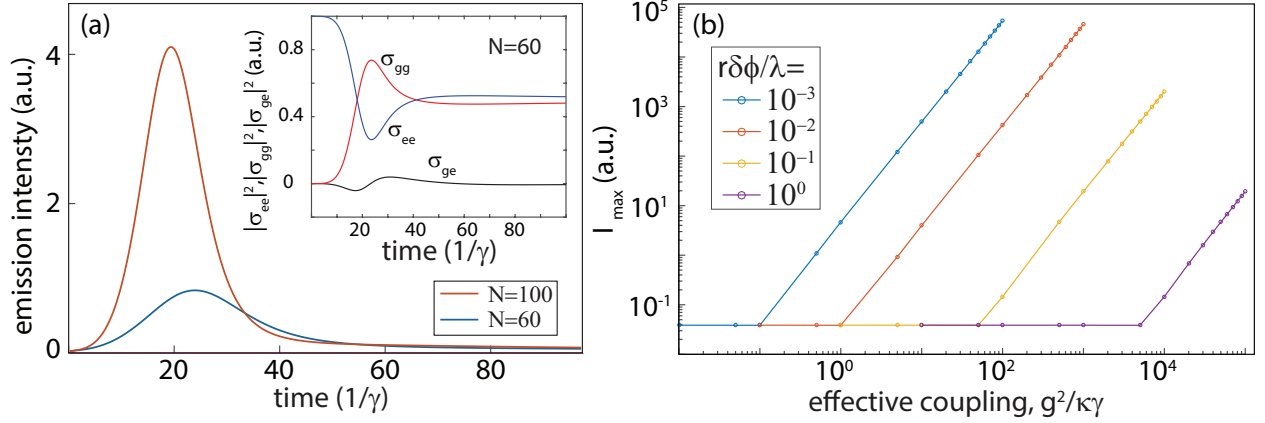


Figure 5.2. (a) Intensity of the emission light from an ensemble of 60 and 100 atoms inside the resonator. Inset is a plot of atomic population and coherence as a function of time. (b) Maximum emission intensity as a function of total atom number in the cavity for 100 atomic segments with different width of local atomic distribution. Simulation parameters include: cavity decay rate, $\kappa = 10^6\gamma$, atomic decoherence rate $\Gamma = 0.01\kappa$, light-atom coupling strength, and $g/\Gamma = 0.5$.

$N_{eff} = \kappa/\Omega N$ contributing to the superradiance emission. Overall, the broadening gives rise to sub and superradiance emission lines with non-exponential decay curves [22].

5.4 Controlling dissipation

In this section we discuss that even when cooperative emission conditions are not fully satisfied, atomic geometry can be engineered to reduce dissipation in the system. Recently, we have performed an experiment studying cooperative resonances formed by a lattice of erbium ions in a silicon nitride ring resonator. An array of atomic segments were implanted into the solid resonator and resonant excitation were used to probe the atomic resonance. Due to the relatively large inhomogeneous broadening and decoherence rate of the atoms in the systems, observation of timed Dicke states were prohibited [37]. Nevertheless, the fast cavity decay rate, relative to the decoherence processes, enabled investigation of a new regime of cooperative interactions. In an ordered lattice commensurate with the emission wavelength, a standing wave is formed by emission from the discrete atomic segments. Because the life time of photons inside the resonator is longer than the decoherence time,

interference between photons from spatially distributed atoms occurs within the time scale of cavity lifetime. The maximum intra-cavity intensity (at the location of any segment) short time after excitation thus scales with $\langle |\sum_j E_{c/cc}(\theta_j)|^2 \rangle = \langle |N E_{max}|^2 \rangle$, where E_{max} is the maximum field amplitude from a single segment and $E_{c/cc}$ is the mean field propagating in either clockwise or counterclockwise directions. In a randomly distributed ensemble, on the other hand, the intensity at the segment i is given by $\langle |\sum_j E_{c/cc}(\theta_i) + E_{c/cc}(\theta_j)|^2 \rangle = \langle N |E_{max}|^2 \rangle$. At the resonance condition, the single-frequency intensity scales nonlinearly with the atom number, however it does not reach the peak cooperative emission because the interaction time, $1/\kappa$, is smaller than the coherence time. In other words, as the cavity decay rate, κ , is faster than any relevant time scale in the system, e.g. $\kappa > \Gamma, \Omega/N, \gamma$, timed superradiance is not observable, because light leaves the cavity before cooperative coherence is built up. Although the inhomogeneous broadening in the system masks the true timed superradiance characteristics (lifetime shortening) by effectively reducing the contributing atom number, it enables almost continuous tuning of the atomic resonance. Therefore, the atomic resonance can be achieved at different emission wavelength by either changing the implantation parameters or varying the effective index of the solid resonator. As the result, losses induced by non-radiative decay, propagation (scattering) loss, or phonon-assisted excitation can be compensated for by tuning the resonance at a desired emission wavelength. For example, the propagation loss is reduced by minimizing the light intensity between the atoms at the resonance condition. In other words, the relatively broad atomic resonance spans over multiple resonator's free-spectral ranges giving rise to Fano-type interference and loss suppression.

In the limit of low atom numbers, less than one photon can be emitted within the cavity lifetime, as was the case in our recent experiment. The emitted photon creates a collective excitation as superposition of atoms contributing to the emission. The process can also be seen as amplified spontaneous emissions which its controlled rephasing [40], [41] can lead to retrieval of the collective excitation in a form of a second photon correlated to the first one. Below, we discuss the general principles of bi-photon generation in more details in the case of three-level atoms.

5.5 Photon generation

The collective emission from atomic ensembles has been the center of research for the generation of photon pairs from atomic gasses and solid state emitters[42], [43]. As proposed by Duan-Lukin-Cirac-Zoller (DLCZ) [44] the memory-based bi-photon generation in this way can be used to implement entanglement distribution for long-distance secure communication[1]. The DLCZ protocol is one of the practical proposals, to date, for implementation of quantum repeaters [45] and its proof of principle demonstration has been achieved using laser cooled atoms[26], [46]. The cooperative emission can be engineered via the atomic geometry to realize topological effects [47]. To study photon generation in the present case, we consider an array of three-level atoms hosted by a ring whose resonance wavelength matches the atomic transition, see Fig.5.3 (a). Figure 5.3 (b) provides a 1-D representation of the system where atomic segments form a commensurate or incommensurate lattice with light propagating along the lattice. We note that, instead of multiple atoms per segment, single atoms can be considered without change of the general discussion below. On the resonance condition, atoms define fixed antinodes of an standing wave inside the resonator symmetrically emitting light in both directions. Upon excitation with the pump light (P_a), a Stokes photon generated in mode a is indistinguishably emitted in the forward or backward (clockwise or counterclockwise) directions. In the cooperative emission regime, the atoms emit in-phase, and in the single-photon regime a collective excitation of atomic spins is formed as the footprint of the emitted photon. The single collective excitation can be created even when conditions for timed Dicke superradiance are not quite met. The collective excitation can then be retrieved using another pump (P_b) in a form of an anti-Stokes photon in mode b . Such bi-photon generation has been studied in depth in atomic systems and the method has been proposed and demonstrated for application in entanglement distribution [26], [44]. In solids, bi-photon generation of this kind was also achieved [43] by preparing atoms in an atomic frequency comb to address difficulties with optical pumping in solids.

A Hamiltonian similar to Eq.5.2 can be written for the anti-Stokes photon in mode b with field operators denoted by \hat{b}_c and \hat{b}_{cc} . Assuming a discrete distribution of atoms at locations θ_j , we use second perturbation and trace out the atomic degrees of freedom to arrive at:

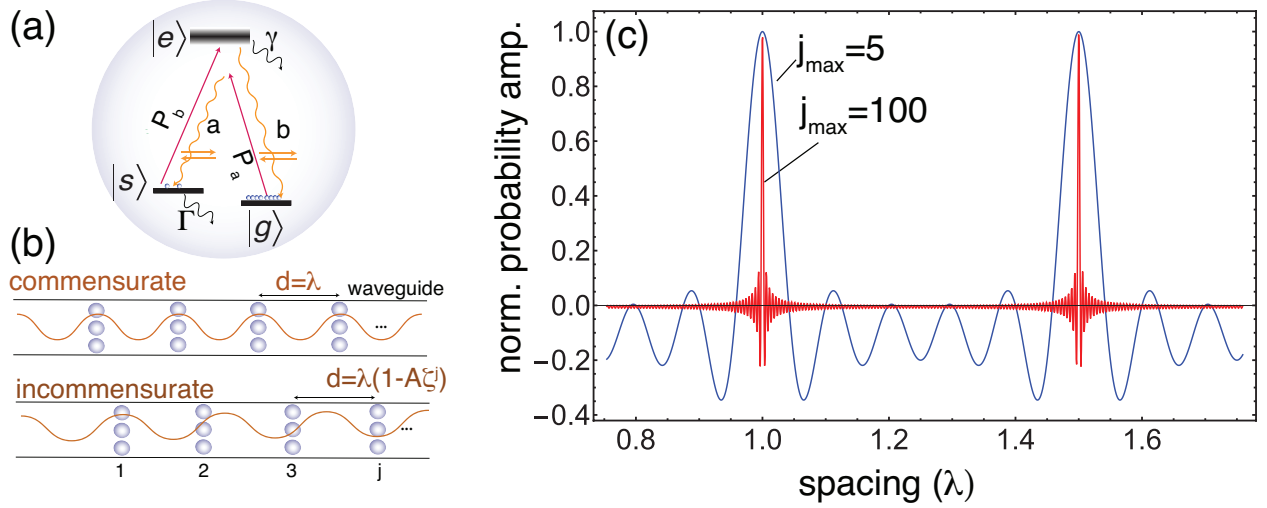


Figure 5.3. (a) The level diagram of a three-level atom considered with two pump light deriving two Λ transitions creating photons in modes a and b in two directions. (b) A 1-D representation of the light-atom interaction for two arrays of atoms one commensurate and one incommensurate with the intra-cavity light whose also resonant with the Raman transition of the atoms. (c) The normalized probability amplitude of emitting bi-photons in the same direction is plotted as a function of lattice constant for 5 and 100 atoms interacting with the intra-cavity light.

$$\tilde{H}_{int}/\hbar \simeq J \left\{ \Theta(k) \hat{b}_c^\dagger \hat{a}_c^\dagger + \Theta(-k) \hat{b}_{cc}^\dagger \hat{a}_{cc}^\dagger + \hat{b}_c^\dagger \hat{a}_{cc}^\dagger + \hat{b}_{cc}^\dagger \hat{a}_c^\dagger + h.c. \right\} \quad (5.8)$$

where J is the effective coupling rate of each segment (atom), and the coefficient $\Theta(k)$, defined as

$$\Theta(k) = \frac{1}{\sqrt{N}} \sum_{j=1}^N e^{-2ikr\theta_j}, \quad (5.9)$$

is the collective phase factor controlled by the geometry of atoms. Applying this Hamiltonian to the initial state, the optical field (vacuum state) returns the final (unnormalized) optical state given by

$$|\Psi_f\rangle = \Theta(k) |1_a\rangle_c |1_b\rangle_c + \Theta(-k) |1_a\rangle_{cc} |1_b\rangle_{cc} + |1_a\rangle_c |1_b\rangle_{cc} + |1_a\rangle_{cc} |1_b\rangle_c \quad (5.10)$$

where, for example, $|1_a\rangle_c$ represents one photon created in the mode a propagating in the clockwise direction. The phase factor $\Theta(k)$ is related to the probability of generating two

co-propagating photons and it is plotted in Fig.5.2 (c). When atomic spacing is a multiple of $\lambda/2$, this probability is maximum. The absolute probability at this resonance condition scales with the square of number of segments and the width of the resonance scales linearly with the number of segments. The probability of creation of co-propagating bi-photons is close to zero for a large lattice with lattice spacing not equal to the wavelength. In this regime, similar to a large ensemble of randomly positioned atoms, correlated photons are emitted only in opposite directions. In small atomic ensembles, unlike a random sample, probability of co-propagating bi-photon generation can be set to zero by carefully designing atomic spacing. The approach enables generation of entangled photon pairs from a small ensemble of atoms arranged in a cavity.

To further study the effect of atomic geometry on photon emission and also state engineering, we consider an atomic lattice with spacing between the segments engineered as j and $j + 1$ to be $d_j = \lambda(1 - A\zeta^j)$, where λ is the wavelength of the emitted photons, A is a constant and ζ is the incommensurability factor (see Fig.5.3 (b)). As seen in Fig.5.4 (a) and (b), when the lattice becomes more and more incommensurate with the wavelength, the probability of generating co-propagating bi-photons decreases while a phase appears in the first term of Eq.5.10, which is opposite to that of the second term. In the following section, we see how a proper choice of the Θ parameter in an incommensurate lattice enables mitigating noise in atomic ensembles.

5.6 Storage in an ordered lattice and the effect of geometry

To see the effect of atomic geometry in protecting quantum information in the system, we now consider retrieval of a single-photon pulse after being stored inside the atoms as a collective excitation. We consider a lattice of two-level atoms initially prepared in the ground state, $|g\rangle$, arranged around the ring. A single photon pulse enters the cavity can be coherently absorbed by the atoms using, for example, a controlled reversible inhomogeneous broadening (CRIB) technique [48] and retrieved after time τ_s . The Hamiltonian of the full storage/retrieval interaction can be approximately written as

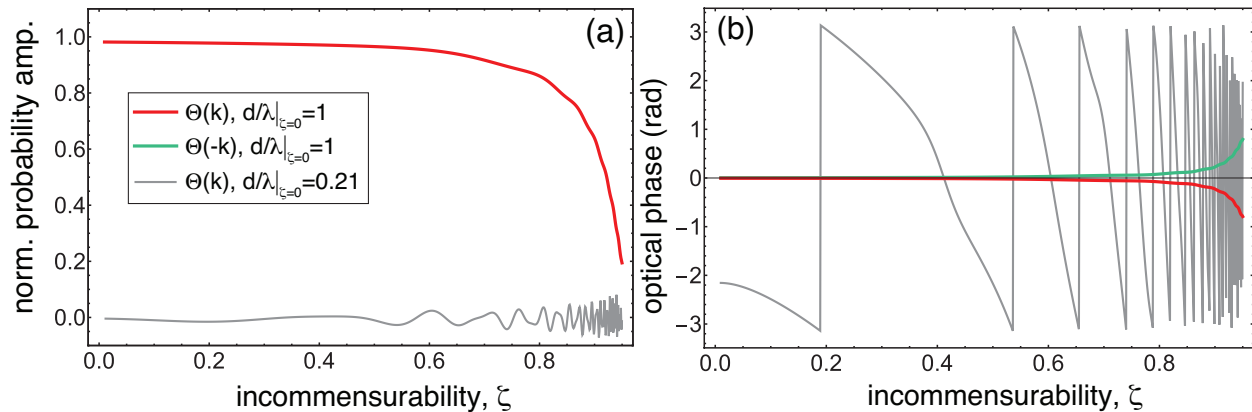


Figure 5.4. The amplitude (a) and phase (b) of $\Theta(k)$ as a function of the incommensurability constant ζ . The gray curve shows amplitude and phase of $\Theta(k)$ for an atomic array out of the resonance with the optical wavelength. Results plotted considering 100 segments with $A = 0.2$.

$$H_{int}/\hbar \simeq J \left\{ \hat{S} \hat{S}^\dagger [\hat{a}_c^\dagger(t + \tau) + \hat{a}_{cc}^\dagger(t + \tau)] [\hat{a}_c(t) + \hat{a}_{cc}(t)] + h.c. \right\}.$$

For an input field (e.g. a photon wavepacket) initially propagating in the clockwise direction through an atomic lattice, the retrieved photon can be emitted in either clockwise or counterclockwise direction introducing loss to the memory. In absence of phase noise and considering a random distribution of atoms in an ensemble, one can see that ideally perfect retrieval can be achieved in the backward direction, in the limit of large J . We note that scattering into the free-space is determined by the spontaneous emission and is independent of atomic geometry in the limit of weak coupling. The free-space scattering introduces a constant loss to the process which we ignore in the following treatment.

In presence of phase noise, $\delta\theta(t)$, the quality of the storage process declines and we show below that an ordered lattice can overcome some of the losses introduced by the phase noise among the atoms. In presence of phase noise, the effective Hamiltonian of the optical fields, after tracing over the atomic excitations, can be written as:

$$H_{eff}/\hbar = J \int_{\tau_s/2}^{\tau_s} \int_0^{\tau_s/2} \left\{ \Theta(k) e^{im\delta\theta(t-t)} \hat{a}_c^\dagger(t) \hat{a}_c(t) + e^{-im\delta\theta(t-t)} \hat{a}_{cc}^\dagger(t) \hat{a}_c(t) \right\} dt dt$$

where $m = 2\pi r/\lambda$ is the number of atomic segments and the phase noise is characterized by $\delta\theta(t)$. In a randomly distributed ensemble and when $\delta\theta_{max} \sim 1$ (in units of 2π), both terms vanish and no coherent interaction is expected. The absorbed photon is randomly emitted in both directions washing out the imprinted phase information of the input signal.

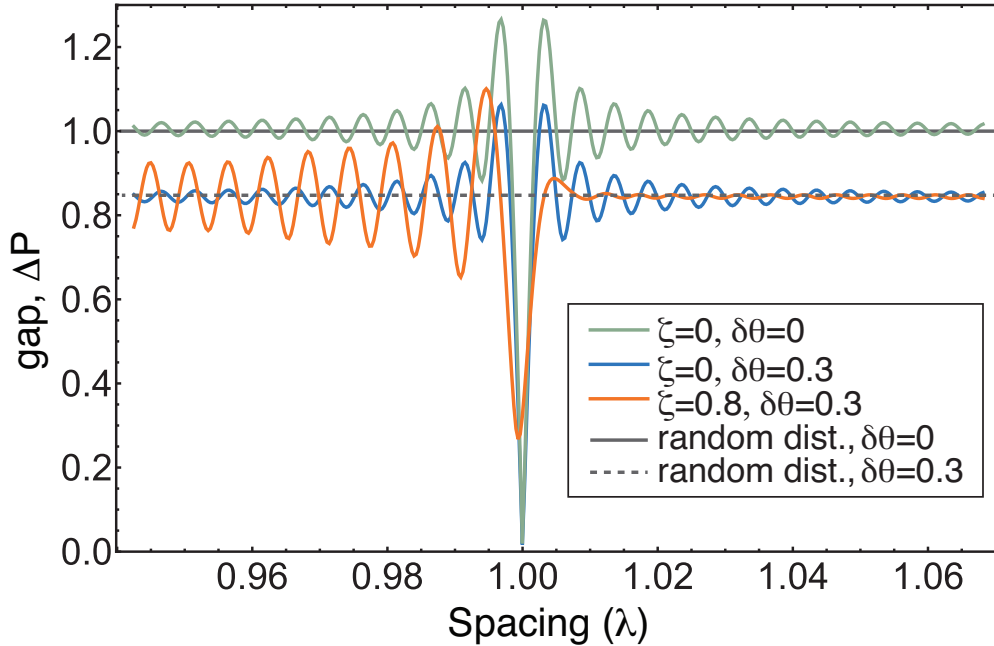


Figure 5.5. The difference in effective coupling (energy gap) of the two clockwise and counter clockwise modes.

For an ordered lattice, however, an energy gap between co- and counter-propagating photons is created whose magnitude scales with $\Delta P = |(\Theta(k) - 1) \cos(kr\delta\theta) + i(\Theta(k) + 1) \sin(kr\delta\theta)|$, preventing the scattering in the forward direction and thus reduces the radiative loss within the atomic media. As an example, the energy gap is plotted in Fig.5.5 for a lattice of 100 atoms (or atomic segments) with 30% phase noise. The introduced phase noise reduces the gap (and similarly coherent retrieval efficiency) compared to the ideal lattice as shown by green and orange curves, respectively. Slightly away from the atomic resonance, the gap increase recovering the efficiency and even reach the ideal performance of a random sample crossing $\Delta P = 1$. When an incommensurate lattice is considered, the gap can increase to ≥ 1 and operation regime can be wider and more robust to lattice parameters, Θ . We note that for a random atomic distribution, the gap still exists which arises from the

entanglement between the atoms and the first emitted photon. In such case, the maximum achievable gap is one. The current results suggest the gap can be increased by a careful choice of atomic distribution even in presence of phase noise.

5.7 Conclusion

We investigated the role of atomic geometry on light emission and storage within a ring resonator. We showed that by designing atoms within a photonic waveguide or resonator, it is possible to significantly boost the efficiency of the interactions. We showed that an incommensurate lattice of atoms embedded in a ring resonator can be used to suppress loss and phase noise in photon retrieval process. The clockwise and counterclockwise photons can be regarded as sudo-spin $1/2$ particles and therefore lattice engineering can be used to eventually design active topological quantum photonic structures [49]–[51]. Active elements including quantum dots [21], [52], [53], laser trapped atoms[24], [54] and rare earth ions integrated with photonic waveguides and resonators are suitable platforms for studying cooperative effects in active photonic devices[55] with application in classical and quantum photonics[30], [56].

6. ATOMIC ARRAY IN SILICON PHOTONICS

Portions of this chapter have been previously published: Nandi, Arindam, et al. **“Controlling light emission by engineering atomic geometries in silicon photonics.”** Optics letters 45.7 (2020): 1631-1634.

Novel phenomena emerge when resonant modes of a hybrid system undergo coherent interactions [57]. The interactions of this kind may result in engineering unconventional materials and platforms for broad applications. In photonics, the coherent and cooperative mode coupling has resulted in observation of peculiar effects including Fano interference [57], cooperative light scattering, [24], [28], [58], cavity quantum electrodynamic (cQED) interactions [59], [60], Borrmann effect [61], [62], and topological optical effects [51], [63], [64]. Also, controlling the position of laser-cooled atoms near waveguides and fibers has led to the observation of peculiar effects such as coherent backscattering[58]and superradiance[24]. In a different platform, photon-mediated coupling between a small ensemble of microwave oscillators in a superconducting circuit has been observed[65]. In solid photonics, engineering light-atom interactions to achieve long-range coherent interference in the medium has not been achieved due to the lack of control on atomic positioning. Towards realization of scalable and long-range interference between fields in an atomic ensemble, we study the effect of atomic geometry on photon emission in solid-state photonics. The atoms, in this case, are erbium ions which are rare earth ions with a telecom-band transition embedded in silicon nitride materials. The approach enables study of a novel regime of light-matter interactions in solids by designing the atomic geometry and mode coupling in the system. The relatively low sensitivity of the rare earth (RE) ions to the solid’s environment makes these ions an attractive substance for realization of linear and nonlinear light-matter interactions for quantum applications[7], [8], [10].

6.1 Introduction

In this work, by activation of silicon nitride structures using precision implantation of isotopically pure Er ions, we study coupling between optical and atomic Bragg resonant modes. We observe emission enhancement when the embedded atomic lattice is commensu-

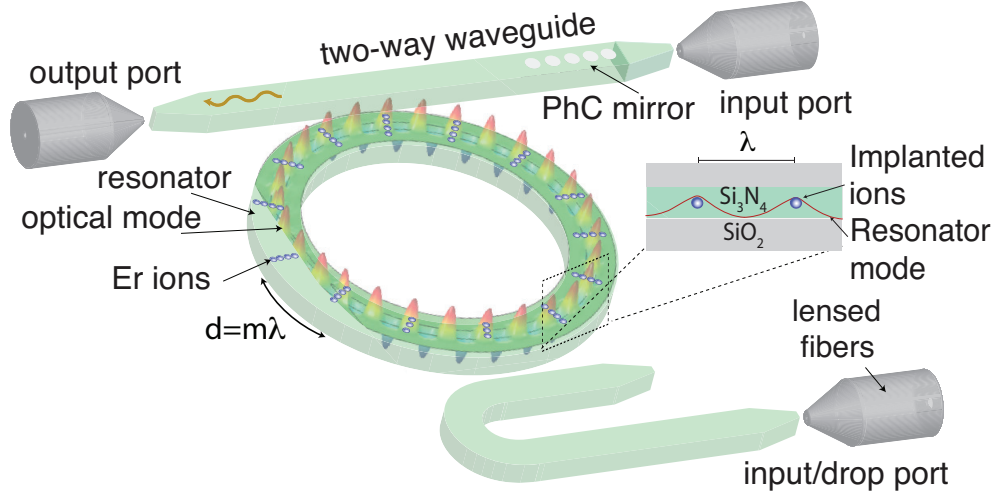


Figure 6.1. Schematic of the designed active SiN ring resonator. Isotopically pure ^{168}Er ions are implanted as an array inside a microring cavity. The segments are separated by multiples of the wavelength of Er emission. At each segment with a width much smaller than the wavelength, around 10^4 ions were implanted along the diameter of the ring. A photonic crystal mirror is used to increase the collection efficiency to the lensed fiber on the left (output port). The excitation pump enters the ring either from the drop-port or the mirror-side waveguide using another lensed fiber.

rate with the wavelength of the emitted light. This is because, the emitted light from the atomic lattice gives rise to coherent spatial interference creating a Bragg atomic resonance. On the resonant condition where the emission wavelength is commensurate with the atomic lattice, the scattering loss decreases. Moreover, we record asymmetric lineshapes of photon emission governed by Fano interference between the resonant modes of the system. In this way, we take advantage of the inhomogeneous broadening of ions in silicon nitride to enhance collection of radiation at a desired wavelength within the emission band of the Er ions .

6.2 Theory

We use isotopically pure ^{168}Er ions directly implanted in a SiN microring resonator into a periodic array (atomic lattice) (see Fig.6.1). Considering an array of ion segments (with the width of each segment being much smaller than the wavelength) implanted in a ring resonator, the emission from the ion array can be approximately described by a 1D theory of atoms coupled to a waveguide.

We study the interaction dynamics by numerically solving the semiclassical Maxwell-Bloch equations of motion. The equations of motion capturing the interaction of light with an ensemble of atoms in free space are

$$\frac{d\mathcal{E}_{b/f}}{dz} = \pm i\mathcal{N}(z)\sigma_{12} \quad (6.1)$$

$$\frac{d\sigma_{12}}{dt} = -(\gamma_h + i\delta\omega)\sigma_{12} + ig(\mathcal{E}_f^* + \mathcal{E}_b e^{2ikz})(\sigma_{22} - \sigma_{11}) \quad (6.2)$$

where $\mathcal{E}_{f/b}$ is the expected value of the forward/backward intra-cavity electric field operator, $\mathcal{N}(z)$ is a function describing the linear atomic density, σ_{12} is the amplitude of the atomic polarization in a two-level atom, γ_h is the decoherence rate which includes both population decay rate ($\gamma = 1/T_1$) and excess dephasing (γ_p) and g is the light-atom coupling rate. The inhomogeneous broadening of the atomic transition is described by $\delta\omega$. We numerically solve these equations for various atom spacing. The result for emission from the array is shown in Fig.6.2(a) as a function of the atomic spacing. The maximum intensity is observed when the atom spacing is a multiple of half of the resonant wavelength. This is consistent with the free-space Bragg theory[66]. In the case of a continuously driven ring resonator and in the limit of $\kappa > \gamma$, the cavity field with decay rate κ can be adiabatically eliminated with light-atom dynamics approximately described by Eqs.(1)-(2). The mode mixing [67], [68] and coherent interference in the spatially ordered lattice [66] in the ring resonator gives rise to a standing wave structure for the scattered light [69]. The atomic lattice acts as a Bragg grating [58] scattering light in both directions with probability $|\beta_{eff}/(1 + \beta_{eff})|^2$, where β_{eff} is the effective ratio of scattering into the resonator mode by the ensemble of the atomic segments [70], $N_{eff}g^2/\kappa$, to that of free space, γ , and N_{eff} is the effective atom number contributing to the scattering process. Compared to the free-space case, β_{eff} is enhanced in the ring by a factor of F/π [71], where F is the equivalent resonator finesse. With standing wave nodes of the scattered light at the position of the atoms, the scattering loss is expected to reduce[66]. We note that reduction in scattering occurs in all directions due to lower field intensity at the location of the atoms. This is different from Purcell enhancement or superradiance because the cavity effect induced by the atoms is not strong enough, or atomic coherence is not long enough, to affect the spontaneous emission rate. The enhanced photoluminescence is

because of the reduction in scattering loss imposed by the Bragg resonance. The scattering loss from the ensemble is approximately given by $(1+2\beta_{eff})/(1+\beta_{eff})^2$, for an optically thin ensemble. In an optically thick sample, multiple reflections give rise to radiation trapping and scattering loss, which can still be significantly less than the case of random atomic distribution[66].

The emission from the ion array is theoretically described by a 1D theory of atoms coupled to a waveguide [58]. For a single atom in the cavity, the ratio between the spontaneous emission into the cavity or waveguide, Γ_{1D} to that of the free-space, Γ , is given by the cooperativity defined in the main text. In a multilevel-multiatom system, this ratio is modified due to the non-unity branching ratio[72], atomic position and inhomogeneous broadening in the atomic transition. It should be noted, for a system in the bad cavity limit with excess dephasing, there are two different cooperativity to parametrize the system [73]. For a two-level atom, depending on the application the cooperativity can be defined as $\eta_I = g^2/\gamma\kappa$ or $\eta_\phi = g^2/2\gamma_h\kappa$ where κ is the cavity linewidth, $\gamma = 1/T_1$, $\gamma_h \sim 1/T_2$ and g is the coupling between atom and cavity. For characterizing light-light interaction and spatiotemporal coherent properties of the atom-cavity system, the quantity η_ϕ is used. For emission of a two level atom inside a cavity the definition η_I is more appropriate, as discussed in Ref.[73]. In our system, the temporal coherence condition needed to observe photon-photon interaction leading to phenomena like superradiance is not satisfied. For description of PL in a multilevel atom we use $\eta = \eta_I \frac{T_1}{T_{spon}}$ and the branching ratio is $\frac{T_1}{T_{spon}}$. Here T_{spon} is the spontaneous emission time for a simple two level system from the excited state to the ground state. As the oscillator strength for Er in silicon materials [73] is similar to crystals such as YSO, the branching ratio can be estimated from the measurement in Er:YSO crystal[72]. For Er in silicon, we estimate the branching ratio to be around 0.1. We calculate the bare cooperativity, η_I using the measured FSR, cavity linewidth and assuming 0.7% of mode energy at the ions' position and find values of approximately 1.25 and 2.25, for ringA and ringB respectively. To account for the inhomogeneous broadening, atomic distribution and lattice incommensurability one needs to calculate the effective cooperativity of each atomic segment of width $\delta = Rd\theta$ by calculating the convolution function as $\eta_j = \int_{-\infty}^{\infty} f(\lambda)d\lambda \int_{-\lambda/2}^{\lambda/2} \eta_I \cos^2 [k(ja_0 + x)]\mathcal{N}(x)dx$ where $f(\lambda)$ is the frequency distribution of

atomic transitions due to inhomogeneous broadening approximately described by a Gaussian distribution of atomic frequencies, and $\mathcal{N}(x)$ is the linear atomic density. In the case of current work, $\delta \simeq 40nm$ and total number of atom segments is 245 and 980 for ringA and ringB, respectively. For simplicity, we assume a relatively flat inhomogeneous broadening distribution of atomic frequency in the range where PL drops around $\zeta = 1$. The effective cooperativity averaged over all atoms can be calculated using the above equation with its value less than 0.1.

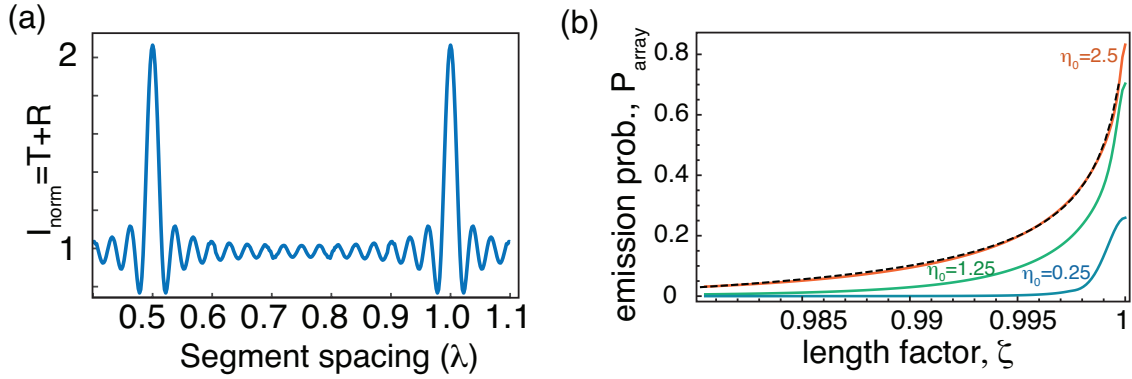


Figure 6.2. (a) Result of numerical simulation for total field intensity ($T + R = |\mathcal{E}_b(z = 0)|^2 + |\mathcal{E}_f(z = L)|^2$) as a function of atom spacing from a lattice of atoms, which is normalized to that of a random atomic distribution. In this simulation, 15 atomic segments were considered. (b) Emission probability plotted using Eq.6.3 for $\eta_I = 0.25, 1.25$ and 2.5 (solid lines). The dashed line shows the Beta probability function approximately describing the decay of the probability at high cooperativities.

For a perfect point-like ion array ($\eta_I = \eta_j$) the normalized emission probability from the ensemble is given by multiplying the transfer matrix of each ion segment as, $P_{array} = \left| \frac{M(1,2)}{M(2,2)} \right|^2$, where $M_{array} = T_{a,N} \cdot T_{f,N} \cdot T_{a,N-1} \cdot T_{f,N-1} \dots T_{a,1} \cdot T_{f,1}$ and

$$T_{a,j} = \begin{pmatrix} 1 - \eta_j/2 & -\eta_j/2 \\ \eta_j/2 & 1 + \eta_j/2 \end{pmatrix}, T_{f,j} = \begin{pmatrix} e^{ika_j} & 0 \\ 0 & e^{-ika_j} \end{pmatrix} \quad (6.3)$$

are the transfer matrices of the atomic segment j and free-space propagation from the $j - 1$ to j segment.

As the excitation emission wavelength deviates from the lattice spacing, it becomes incommensurate with the lattice and therefore the emission drops. Figure 6.2(b) shows a plot of P_{array} for $\eta_I = 0.25, 1.25$ and 2.5 . At bare cooperativities close or higher than one, the probability decays approximately as a beta function. For low cooperativities the decay of PL emission is more and less Lorentzian.

6.3 Experimental details

To experimentally study the effects described above, we fabricate microring resonators using a 500nm thick SiN layer on SiO₂. The width and diameter of the ring is 1.5 μm and 150 μm , respectively. Er ions were implanted into an ion array, separated by an integer number of the Er emission wavelength, with a precision of $\pm 10\text{nm}$ at the Sandia National Laboratories. The energy used for the implantation was 200 keV with implantation depth of 50nm. About 10^4 ions were implanted in a rectangular area of width 20nm along the radius of the ring.

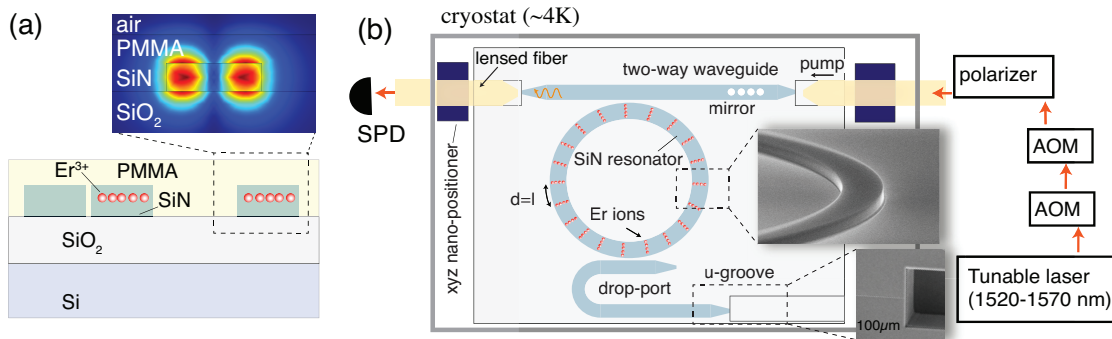


Figure 6.3. (a) Schematic cross section of the SiN resonator with Comsol simulation of the mode with effective index 1.58 shown in the inset. (b) Experimental setup showing two lensed fiber precisely controlled inside the cryostat using nanopositioners to couple light in and out of the sample. Inset shows the SEM of the ring resonator wall with smooth etching and u-grooved for fiber-to-chip coupling.

The sample was then annealed at 1100°C for one hour in nitrogen flow of 5.0 standard liter per minute (SLPM). A polymer (PMMA) layer of around 1 μm thick was spin coated on the sample as an upper-cladding after annealing for better mode confinement and also to fine tune the effective index of the optical mode by varying the thickness of this layer. The sample was placed inside a cryostat with typical temperature of 4K with two optical fibers directing light to/from the sample from/to the room-temperature setup outside the cryostat for measurement. The atoms were resonantly excited by a tunable diode laser. Typical input power of the pump in the experiments was around 5 μW , below the saturation limit of the erbium ions. Two AOMs were used to create a pulse to pump the atoms for 6ms and turn it off for 10-15ms during the photoluminescence (PL) measurement. The PL light was detected using a single photon detector and counts were averaged over 10^5 runs.

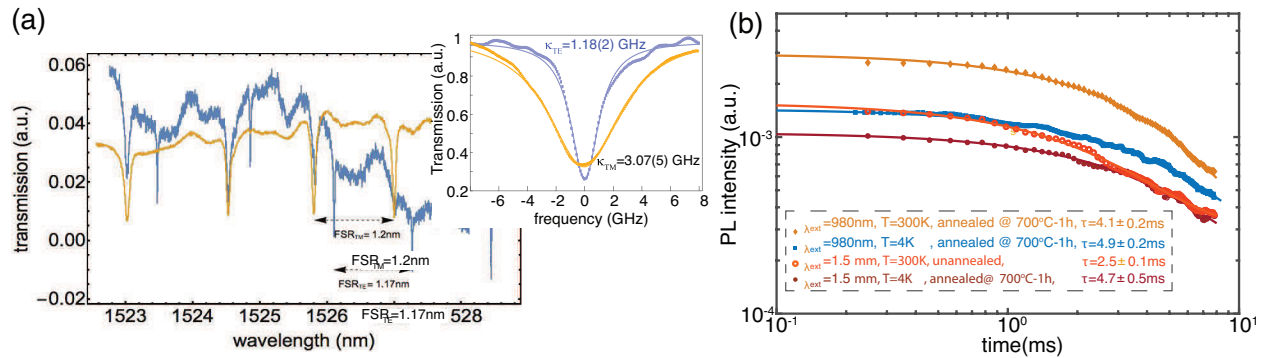


Figure 6.4. (a) Measured cavity transmission for the two orthogonal polarization. As the waveguide and ring are design for the TM mode, TM has the highest coupling while TE has the highest Q factor. The free-spectral range (FSR) of the two TM and TE modes and effective mode indices match the COMSOL calculations. The inset shows the fitted Lorentzian cavity transmission for TE (blue) and TM (orange) modes. (b) Photoluminescence decay of ions in the resonator is shown under 980nm (off-resonant) and 1.5 μm (on-resonant) excitation of annealed and not-annealed sample.

The experimental setup is shown in Fig.6.3(a). The fabrication process of the SiN structures (Fig.6.3(b)) starts with a (100) silicon wafer with 3 μm thermally grown oxide layer. First, stoichiometric SiN layer of 500 nm is deposited in the horizontal tube furnace of a low-pressure chemical vapor deposition (LPCVD) tool from a gas mixture of dichlorosilane and ammonia at a temperature of 800 °C. Next, an electron-beam resist of hydrogen

silsesquioxane (HSQ) is spun over the sample and device patterns. The device patterns (micro-resonator structures) are written by a 100kV ultra-high resolution, wide-field electron beam lithography (EBL) tool. Reactive-ion-etching (RIE) is then performed to etch the SiN using HSQ as an etch mask by an inductively-coupled plasma RIE machine. We use CF_4/O_2 chemistry to etch the SiN to create almost vertical etching profile (Fig.6.3(a) Inset). This method enables fabrication of high-Q ($\sim 10^7$) microring resonators at 1550 nm [74].

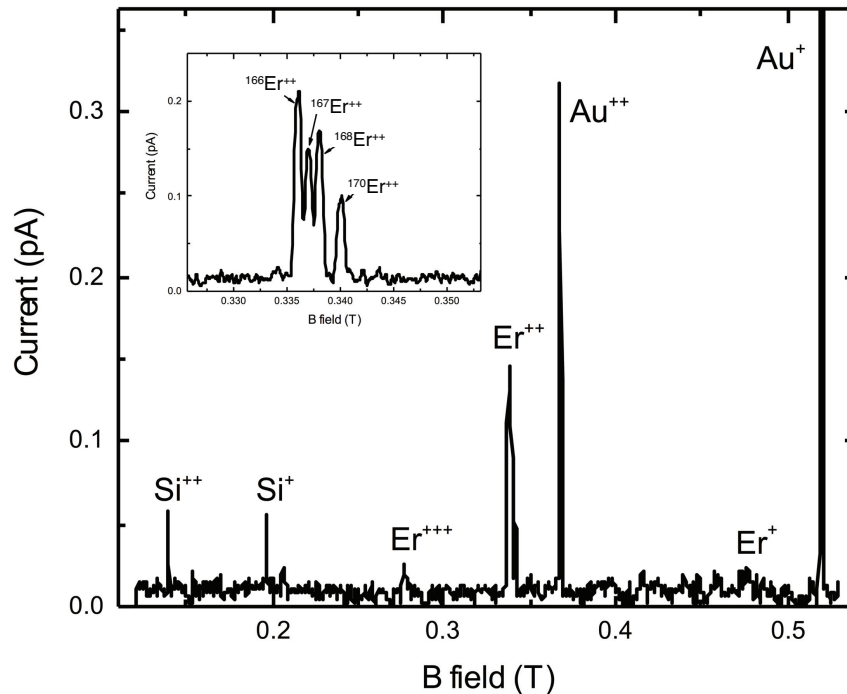


Figure 6.5. Mass spectrum of Er isotopes (inset) and Er, Au and Si ions measured at Sandia to deterministically select an Er isotope prior to implantation.

In order to efficiently couple light to the waveguide we use a tapered waveguide and couple the light directly from the fiber to the optical resonators. To have a stable and low-loss fiber to chip coupling for optical measurements we use patterned substrates with U-grooves (Fig.6.3(b)) that allow self-alignment of the optical fibers to the waveguides without any active positioning of the fibers. The grooves can be placed in any orientation of the wafer using RIE dry etching, a procedure first implemented at Purdue. This method avoids limitation of the wet etching that requires devices to be precisely aligned to the crystal lattice

of the wafer. The cross-section of the U-groove shows vertical and smooth sidewall profiles, defined by the Bosch process. The height of the U-groove is about 65 μm from the bottom to the nitride layer. It is about half of the diameter of an optical fiber with cladding. Hence, by simply placing the fiber down into the groove, it allows the fiber core to be aligned with the waveguide in close proximity. Then fine tuning of the fiber position can be achieved by slight adjustment of the fiber position using the nanopositioning stages inside the cryostat. The lifetime measurement shown in Fig.6.4(b) is obtained at different temperature and pump wavelengths using a single-photon detector.

To implant isotopically pure Er ions, we use the Sandia National Lab’s nanoImplanter (nI), which is a focused ion beam system with the ability to implant many different ion species with 10 of nm’s spot size. We first carry out mass spectrometry using a AuSiEr source before the implantation and select a specific Er isotope using a combination of electric and magnetic fields (see Fig.6.5). We were able to unambiguously distinguish Er^+ , Er^{++} and Er^{+++} ions as well as individual Er isotopes of 164, 166, 168 and 170. We chose ^{168}Er isotope and carried out implantation using at 200 keV Er^{++} (100 kV accelerating voltage) and ion fluence of 10^{14} ions/ cm^{-3} . The purity of Er isotope is about 90% based on Fig.6.5 data.

6.4 Measurements and results

For measuring the emission spectrum, we test three ring resonators, ringA, ringB and ringC with 980, 245 and 327 atomic segment numbers, respectively. The bus waveguide is designed to maximally transmit the TM polarization by tapering the waveguide at the fiber-waveguide interface. Due to the large width of the resonator, TM1 mode is efficiently coupled to the resonator with more than 60% coupling efficiency having a loaded Q factor of about 7×10^4 . The calculated effective index for ringA and ringB for this mode is about 1.58. Considering this effective index, the Bragg resonance condition is satisfied at about 1520nm when the atomic lattice spacing is an integer multiple of $1520\text{nm}/n_{eff} = 962\text{nm}$. We refer to this as “commensurate lattice (CL)” at around 1520nm. For ringC, we removed the PMMA layer on the SiN ring resonator. So, the calculated effective index for ringC for this mode is about $n_{eff} = 1.568$, which, in theory, shifts the resonance condition to lower wavelengths (\sim

1508nm). We refer to this as “incommensurate lattice (iCL)” condition where the emission wavelength centered within the Er emission band does not match the lattice spacing.

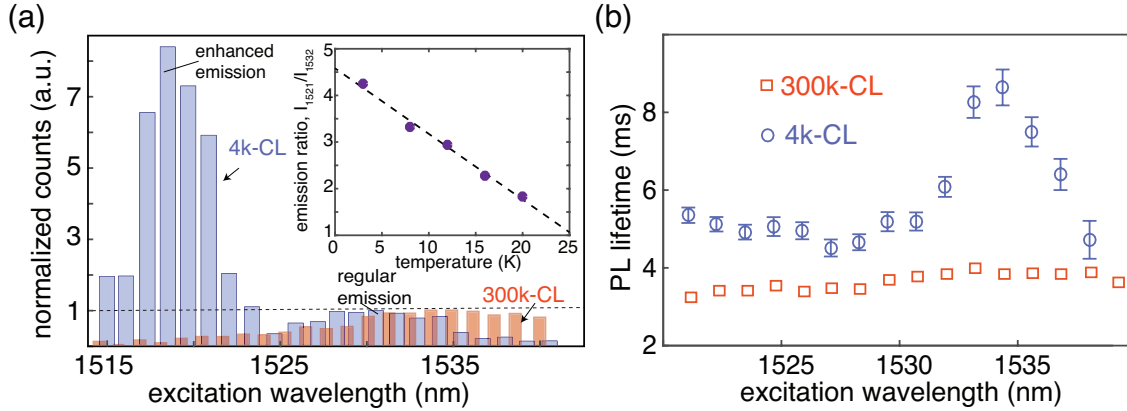


Figure 6.6. (a) Resonance photoluminescence spectrum at 4K (blue bars) and 300K (red bars). The enhanced emission around 1520nm is a signature of the Bragg resonance induced by the atomic lattice. Inset shows the ratio between the peak emission photon number at 1521nm (near the Bragg resonance) to that at 1532 nm (near the typical Er emission) as a function of temperature. Inset shows the temperature dependency of the emission ratio with a dashed line fitted to guide the eye. (b) The PL lifetime is shown for 4K (blue circles) and 300K (red squares). The longer PL decay time around 1535nm is associated with enhanced reabsorption away from the CL condition.

The lowest wavelength that could be reached with our laser is 1510nm. We also note that the implantation of Er ions and annealing conditions for the CL and iCL samples were done under the same conditions and the only difference is the PMMA upper cladding layer and thus the observed effect can not be explained by presence of implantation damage[75], [76]. The fact that host is amorphous and emission shows pump-power dependency and long-lifetime (corresponding to erbium ions) confirms that the enhanced emission is not caused by defects in the hosts.

The emitted mean photon number is measured at every free-spectral range of the cavity. The resulted emission spectrum at 4K temperature is shown in Fig.6.6 (a). The spectrum significantly deviates from the emission of the ions at room temperature. The observed peak emission near 1518nm corresponds to a commensurate lattice with 962nm spacing between implanted segments. Assuming an effective index of 1.578, the result is in agreement with the

calculated resonant wavelength value. Taking into the account our experimental parameters including the spatial atomic distribution width (20nm), inhomogeneous broadening (3nm), total atom number (10^7), yield factor of the implantation (10%), branching ratio in Er ions (0.1), and ion-cavity field overlap (0.5), the estimated β_{eff} is about 50. The scattering loss in this limit can be numerically calculated where significant enhancement is expected[66]. The result in Fig.6.6 (a) shows an enhancement of >30 , in broad agreement with the Bragg theory.

6.4.1 Photon-assisted excitations

As temperature increases the PL ratio decreases suggesting suppression of the emission near the Bragg resonance . This is because of increase in homogenous broadening and phonon-assisted excitations [77] (confirmed by observation of increased absolute emission intensity with temperature rise) at elevated temperatures. The emission ratio is plotted versus temperature as an inset to Fig6.6.(a). The expected homogenous linewidth, γ_h , in amorphous hosts like silicon nitride is expected to exceed the cavity linewidth, κ , at higher temperatures[78] causing β_{eff} to decrease . Moreover, presence of phonon-assisted excitation and also increased inhomogeneous broadening contribute to the reduction of the β_{eff} as the temperature increases. Consequently, the spatial interference and the Bragg resonance effect from the atoms is suppressed at elevated temperatures. It should be noted, that even though we observe enhanced Bragg effect from the ensemble at low temperatures, the single-atom cooperativity is not large enough to alter the atomic decay rate.

The room temperature data in Fig.6.7 provides another evidence of phonon-assisted excitation for 1532nm transition at room temperature. The fitted FWHM of the cavity resonance measured on transmission at 1532nm is 2.8 ± 0.6 GHz while the FWHM of the Erbium emission for that wavelength is 7.3 ± 0.6 GHz. The emission is measured by varying the excitation wavelength around the cavity resonance and collecting emitted photons after the pump is switched off. The broadening of emission spectrum suggests phonon-assisted excitation at room temperature.

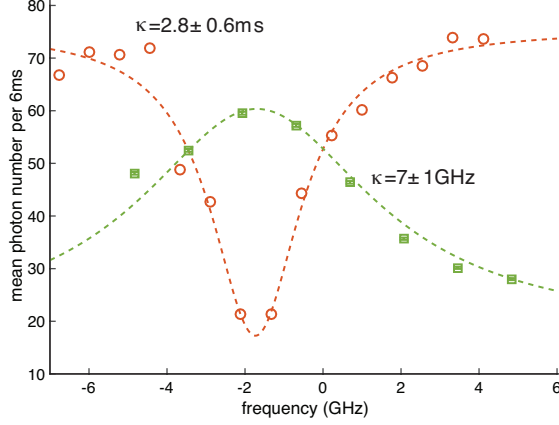


Figure 6.7. PL Emission of Er ions (green square) and pump transmission spectrum (red circle) at room temperature near 1532nm cavity dip.

The emission decay time measured at different wavelengths (Fig.6.6 (b)) shows lengthening of the lifetime at low temperatures, which we associate to suppression of non-radiative decay. The lengthened decay time around 1535 nm is due to the reabsorption [79] (radiation trapping) at the peak (regular) emission wavelength where more atoms exist. The negligible lifetime change around 1520nm ruling out the possibility of dominant superradiance emission from the ions near the atomic Bragg resonance condition.

We plot light intensity at around 1521nm (emission near the Bragg resonance) relative to that of 1532nm (near regular emission peak). Figure 2 (c) shows that beyond some pump power, the emission overcomes the re-absorption and enhanced emission is evidenced. Such enhanced emission is absent for the iCL as the emission signal over the entire spectrum linearly changes with the atom number. At high pump powers, the PL eventually saturates for both transitions.

6.4.2 Absence of Sub and superradiant modes

Our system does not lie in the superradiance regime because of the combination of large inhomogeneous broadening ($\sim 300\text{GHz}$, although significant Erbium emission can be seen across few THz), limited atom number $\sim 10^6$ and long excited state lifetime $\sim 5\text{ms}$. The number of Erbium ions implanted in our sample is in total about $\sim 10^7$ for ringA. Considering yield factor of 0.1, around 10^6 ions will emit upon excitation. In our system, the cavity will

work as filter to allow only a fraction of Er atoms to have a strong coupling to the incoming field. For example, as our cavity linewidth (κ) is ~ 3 GHz, only those Er atoms whose resonance frequency lies within that range, will interact strongly to the field and the effective Ω can be reduced by ~ 100 times. On the other hand, the effective Erbium ions interacting to the emission mode in the cavity is also reduced by the same factor as the result of the inhomogeneous broadening, making the total number of ions $N_{eff} \sim 10^4$.

The superradiance regime is reached in the bad cavity limit: $\kappa \gg \gamma_h/2$, where $\gamma_h = 1/\tau + 1/T_2 \sim 1/T_2$, where τ is the single-atom lifetime of the excited state and $1/T_2$ parameterizes additional atomic dephasing mechanisms. Another necessary condition to observe superradiance is $\Omega/N_{eff} < \tau^{-1}$. The last condition to satisfy is $1/T_2 \ll g^2 N_{eff}/\kappa$ or $\tau/T_2 \ll N_{eff}\eta$. Taking into account the experimental parameters namely T_2 of few ns, $N_{eff} \sim 10^4$ and $\eta \sim 1$, our system does not lie in the superradiance regime. This also supports the argument used before, that our system is not in the limit to observe temporal coherence, which is very important for observing superradiance. This is also the reason, we do not see significant change in the lifetime of the Erbium decay around 1520nm in our system. At higher atom number, a regime of mesoscopic cooperative emission can be reached where both sub and superradiance modes are present[37], [38].

6.4.3 Loss suppression due to atomic geometry

Figure 6.8(b) shows the total photons emitted from the ions in ringA, ringB and ringC as a function of the spacing parameter, $\zeta = n_0 d/m\lambda$, where $n_0 = 1.58$. As ringA and ringB consists of a CL at around 1520nm, we see the enhanced emission near that wavelength. Whereas, for ringC, the Bragg resonance is shifted to lower wavelengths. The center peak ($\zeta \sim 0.992$) corresponds to the regular emission around 1532 nm, which is inhomogeneously broadened. We use a Gaussian function to model the emission centered around 1532nm with a full inhomogeneous width of about 3nm. The linewidth of the enhanced emission peak is governed by atomic spatial distribution (with a Gaussian width of around 40nm), inhomogeneous broadening of the atomic transitions (around 3nm) and number of atoms. We note that although the number of ions for ringC is more than ringB, the effective atom

number, taking into the account the Er atomic transition, is less for ringC giving rise to its broader emission peak.

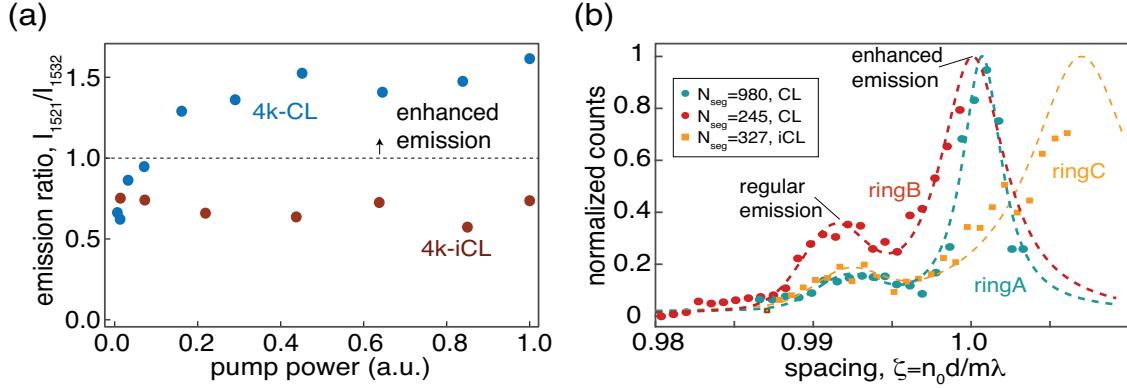


Figure 6.8. (a) The ratio between the peak emission photon number at 1521nm to that at 1532 nm as a function of pump laser power. Here, for the iCL (ringC), near 1520nm, the emission ratio does not depend on laser power, but for the CL (ringB) the ratio increases with laser power and then saturates. Such nonlinear response across the emission spectrum in the CL is expected when emission exceeds the re-absorption probability in the CL. (b) Normalized emission (probability) as a function of spacing parameter, ζ , is plotted for ringA, ringB, and ringC (see text for details). Here ringA and ringB satisfy the CL condition near 1520nm while ringC does not. The dashed lines are Gaussian and Lorentzian fits to the regular and Bragg resonance emission profiles, respectively.

By comparing the fitted amplitudes of the Gaussian (describing PL emission around 1532nm) and Lorentzian distribution (describing the enhanced emission around 1520nm) functions we observe nonlinear dependence of the relative emission to the atom number. For an iCL, the ratio between the two emission peaks (around 1520nm and 1532nm) is independent of the atom number. This is evidenced in Fig. 6.8(a) where power is a proxy for atom number. We observe that the ratio between the emission near the Bragg resonance and regular PL emission scales nonlinearly with the number of atomic segments. In the case of data in Fig. 6.8(b), the resonator with $m = 1$ (ringA) has four times more atoms compared to the resonator with $m = 4$ (ringB). Using the values extracted from the model plotted in Fig. 6.8(b) we infer a ratio of about 2.4 between the emission near the Bragg resonance and the regular emission.

6.5 Fano resonance

The interference between a discrete quantum state and a continuum band of states gives rise to Fano resonances. The shape of the resonant spectrum can be represented by the Fano Formula [57]:

$$\sigma(E) = D^2 \frac{(q + \Omega)^2}{1 + \Omega^2}$$

where E denotes the energy, $q = \cot \Delta$ is the Fano Parameter, Δ is the phase shift of the continuum, $\Omega = 2(\omega - \omega_0)/\Delta\omega$, where ω_0 and $\Delta\omega$ are the resonance energy and width respectively, and $D^2 = 4 \sin^2 \Delta$. We use the above equation to fit the emission spectrum in Fig. 3(b) and extract the q parameter.

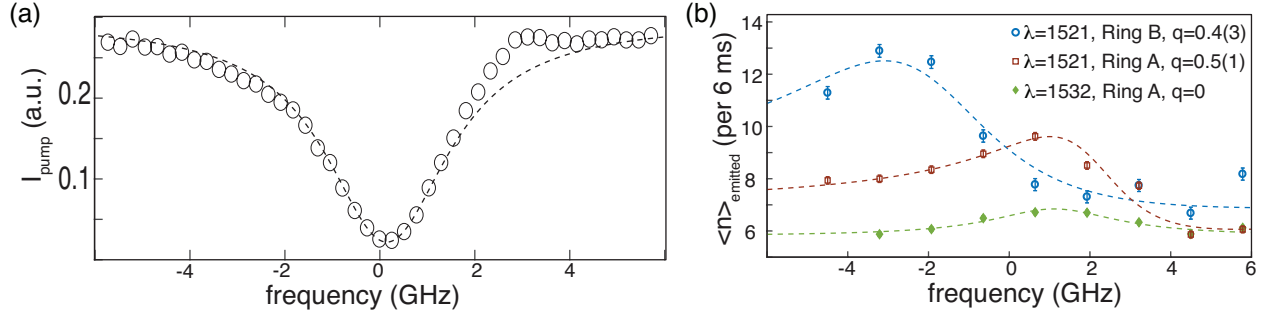


Figure 6.9. (a) Transmitted spectrum of the pump light through ringA with fitted Lorentzian width of 2.6 ± 0.1 GHz. (b) Emission spectrum near cavity resonance at 1520 and 1532nm for ringA and ringB. The spectrum is fitted with Fano-Lorentzian lines with asymmetry described by Fano parameter. The asymmetry in the lineshape of (a) is due to a change in the rate of the scan which does not appear when a wide scan is used. In the case of (b) the laser frequency is fixed for each point and the lineshape around 1532nm (green data) shows a symmetric Lorentzian, as expected from an iCL.

The presence of atomic Bragg condition suggests the possibility of mode interference and appearance of Fano-type resonances in the system[57]. In our system, the coupling between the atomic Bragg mode (continuum mode) and the ring resonator (discrete mode) gives rise to asymmetric emission lines, where phase change of the atomic mode happens very slowly compared to the ring resonator mode. The asymmetry in the lineshape is characterized by the Fano parameter $q = \cot \delta$, where δ is the phase shift of the atomic mode with respect to the cavity mode. This is evidenced by the observed lineshapes in Fig. 6.9(a) and 6.9(b).

A non-zero Fano parameter is fitted to the emission spectrum centered around 1520nm for both ringA and ringB while the emission spectrum around 1532nm (green data) is described by a symmetric Lorentzian function. To obtain this data, we collect PL from the ions after pump excitation at different frequencies around a single cavity resonance near 1520 nm and 1532 nm.

6.6 Conclusion

In conclusion, we design atomic geometries of erbium ions inside a silicon nitride micro-photon resonator and study the effect of geometry on light-atom coupling from the ensemble. We observe that spatial interference at low temperatures from a lattice of ions creates a Bragg atomic resonance enhancing the emission. The interference between the optical and atomic Bragg modes is also observed through Fano-type resonance features. The results indicate possibility of control on light emission, efficiency and lineshapes by engineering the atomic geometry in solid-state photonics. The investigation offers a unique path to further engineer active silicon photonic structures for studying cQED interactions between atoms and photons in an ensemble [80], on-chip photon generation[64], [70], and engineering non-Hermitian Hamiltonians [68].

7. ATOMIC ARRAY IN CRYSTAL

Portions of this chapter have been previously published: Nandi, Arindam, Haechan An, and Mahdi Hosseini. “**Coherent atomic mirror formed by randomly distributed ions inside a crystal.**” *Optics Letters* 46.8 (2021): 1880-1883.

Engineering arrays of atoms as a way to control coherent light-atom interactions has been the subject of intense research in recent years. Collective interaction of atomic arrays with optical photons can give rise to directional absorption or emission which enables engineering of broadband strong atom-photon interactions [81]. It has been suggested that quantum memories with exponentially enhanced fidelities can be achieved using such atomic arrays [82]. Trapped atoms and ion arrays in free-space[83], [84], within cavities [85], or near fibers [28], [58] are being investigated for their application in quantum information. So far, most studies of light interaction with atomic arrays were carried out in laser-trapped atoms. Engineering interaction Hamiltonian of photons with atoms or defects centers in solid-state photonics is of great interest from both fundamental and applied aspects. Design of atomic geometries in solids is challenging as atoms’ location inside solid host cannot be easily controlled.

We have recently shown that using precision ion implantation in silicon nitride materials, arrays of rare earth ions can be engineered to study collective atomic resonances [86]. Other implantation techniques were also carried out in different materials to study on-chip light interaction with rare earth ions [87]–[90]. For quantum applications, however, ion implantation can cause damage to the crystalline host as ion leaves tracks by releasing energy through deceleration, which increases the inhomogeneous broadening and decoherence rate. Rare earth ions doped inside yttrium orthosilicate (YSO) crystals have shown unprecedented coherence time as long as six hours[91], [92]. The random distribution of doped ions, however, does not allow engineering specific distributions of ions. Using spectral hole-burning techniques[93] the absorption spectrum can be reshaped to store quantum light in rare earth crystals[94], [95]. Moreover, spatially addressed single rare earth ions were also demonstrated taking advantage of their spectral broadening [96], [97].

7.1 Introduction

Recently, there has been great interest in engineering arrays of atoms as a way to control coherent light-atom interactions. Spatial distribution of atoms can play an important role in interaction between atomic ensembles and electromagnetic field. Subwavelength confinement of atoms or atoms arranged in a periodic array can cooperatively interact with photons giving rise to sub- or super-radiant modes.

In this project, we demonstrate that erbium ions randomly distributed inside a bulk YSO crystal can be optically engineered to create an effective one-dimensional array collectively and coherently scattering telecom-wavelength photons. We achieve this by spectral hole-burning the randomly distributed ions via a spatially modulated pump intensity. By periodic modulation of atomic population between ground and excited state, we create spatial population grating which coherently back scatters light. The effective atomic lattice has about 5000 centers giving rise to an observed coherent reflection of more than 10 % of the incoming light.

7.2 Experimental details

The experiment is based on isotopically pure ^{167}Er doping with 0.005 % concentration inside an YSO crystal. The crystal is 2x3x4 mm with crystal D1 and D2 axes perpendicular to the optical propagation direction as shown in Fig.7.1 (a). The existence of nuclear spin in this isotope enables enhancement of spin coherence time to about a second at high magnetic fields and cryogenic temperatures [13]. The electronic spin coherence time is however limited by spin-spin coupling and spin-lattice (phonon) coupling processes and is on the order of few microseconds at 3.5K and small magnetic fields [98]. We use optical transition I13/2 to I15/2 (site 2) at 1538nm to burn spectral holes in a form of an array and probe the array by measuring reflection and transmission after spectral hole-burning. Experimental setup and simulation of coherent reflection is shown in Fig.1.

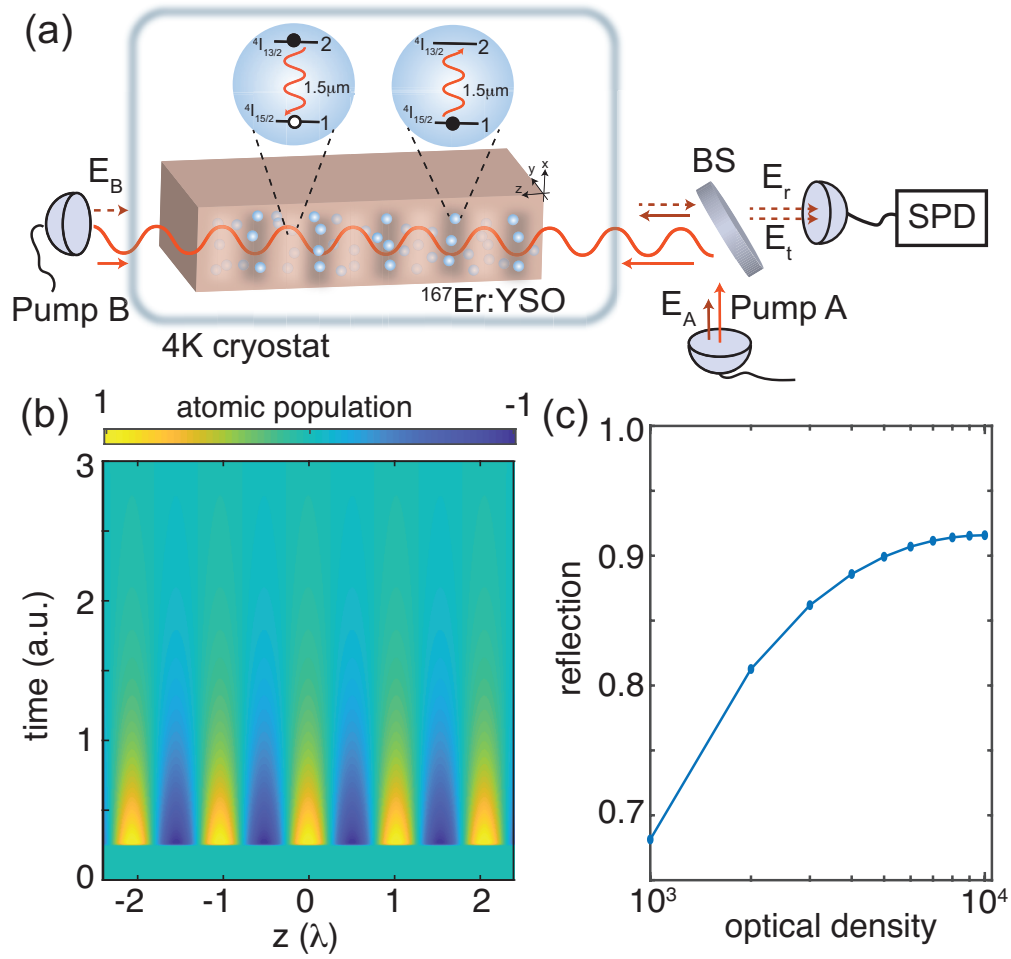


Figure 7.1. (a) A one-dimensional array of atomic scatterers is created inside an Er doped YSO crystal using a standing wave pump (pump A and B) to create spatio-spectral hole burning. Probe light E_A or E_B is applied after hole burning to measure reflection E_r or transmission E_t , respectively, detected by single photon detector (SPD). A magnetic field of 200mT was applied parallel to D1 axis for measurement of coherence time of Er ions. The crystal was placed in a cryostat at 4K. (b) shows numerical simulation of atomic population after atoms are pumped with a standing wave light. (c) Simulated coherent reflection of probe light as a function of optical density.

Here, a single continuous wave (CW) laser (TLB 6700) is used to create two counter-propagating pump pulses and a probe pulse at wavelength near 1538nm. The linewidth of the laser is less than 200kHz estimated over a 50ms time interval. Two AOMs were used to

create pulses from the CW laser. Two counter-propagating pump pulses at 1538nm create a standing wave inside the crystal where atoms are pumped out of the ground state where intensity is maximum. After a typical pumping time of 1ms, spectral holes are created at the anti-node positions of the standing-wave pump giving rise to an effective 1D periodic ion array. A probe light with frequency close to that of pump follows the pump pulse to measure transmission and reflection by the ion array.

7.3 Theory

We can theoretically describe the light atom interaction by writing a set of Maxwell-Bloch equations for atoms' and fields' expectation values as

$$\begin{aligned}\frac{d}{dz_{\pm}}\mathcal{E}_{\pm} &= \pm iN\sigma_{12,\pm} \\ \frac{d}{dt}\sigma_{12,\pm} &= -\Gamma_a + i\Delta_a\sigma_{12,\pm} - ign_0\mathcal{E}_{\pm} + n_{\pm}\mathcal{E}_{\pm} \\ \frac{d}{dt}n_0 &= -\Gamma_n(n_0 + 1) - i2g\left(\mathcal{E}_+\sigma_{12,+} + \mathcal{E}_-\sigma_{12,-} - \mathcal{E}_+\sigma_{12,+}^* - \mathcal{E}_-\sigma_{12,-}^*\right) \\ \frac{d}{dt}n_+ &= -\Gamma_n n_+ - i2g\left(\mathcal{E}_-\sigma_{12,+} - \mathcal{E}_+\sigma_{12,-}^*\right)\end{aligned}$$

Here \mathcal{E} refers to slowly-varying electric field envelope, σ_{12} is mean atomic coherence, and n_0 and n_+ indicate mean atomic population and its variation having the following relationship: $n = \sigma_{22} - \sigma_{11} = n_0 + \left(n_+e^{i2k_n z} + n_-e^{-i2k_n z}\right)$, where σ_{22} and σ_{11} are population of ground and excited states. The wavenumber of pump beam is k_n , the subscript + and - indicate quantities related to forward and backward propagating fields, respectively. Also g is single photon coupling rate, N is linear density of atoms, Γ_a is decoherence rate, Γ_n is population decay rate, and a is light-atom frequency detuning.

The steady state solution of population when $\mathcal{E}_+ = \mathcal{E}_- = \mathcal{E}_{pump}$ is written as

$$n_0 = -\frac{\beta+2}{3\beta+2} \text{ and } n_+ = \frac{\beta}{3\beta+2} \text{ where } \beta = \frac{8}{\Gamma_n} \frac{\Gamma_a}{\Gamma_a^2 + \Delta_a^2} g^2 E_{pump}^2$$

determines the shape of the population grating. At high pump powers, large β leads to maximum population grating with $n_0 \approx -\frac{1}{3}$ and $n_+ \approx \frac{1}{3}$ values. -1 represents ground state, +1 excited state for n_0 .

To account for inhomogeneous broadening of ions in solids, we consider a Gaussian broadening for absorption profile for atoms, $N(\omega)$, and integrate the electric field over all frequencies as: $\epsilon_{\pm}(\delta_p) = \pm \int \int N(\omega) \sigma_{12,\pm}(\delta_p - \omega) d\omega dz_{\pm}$, where σ_{12} is mean atomic coherence between levels 1 and 2, ω is light-atom frequency detuning, δ_p is frequency of probe relative to pump, and \pm indicates integration along different propagation directions. The scattering loss and reflection coefficient can then be obtained, respectively, from the steady-state solution as

$$\eta = \frac{1 - \exp(-2\alpha_0 L)}{\cosh^2(\alpha_+ L)}$$

$$r = -\tanh(\alpha_+ L)$$

where L is the length of the atomic medium and $\alpha_0 L$ and $\alpha_+ L$ are effective optical densities due to mean atomic population and its variation respectively. At high optical densities, the atomic grating can reach a maximum population contrast of 67%. Fig.7.1 (c) shows the result of numerical simulation of coherent back-scattering for increasing optical density, assuming constant broadening and decay rates. At high optical densities, the atomic population grating acts as a mirror coherently reflecting most of the incident light.

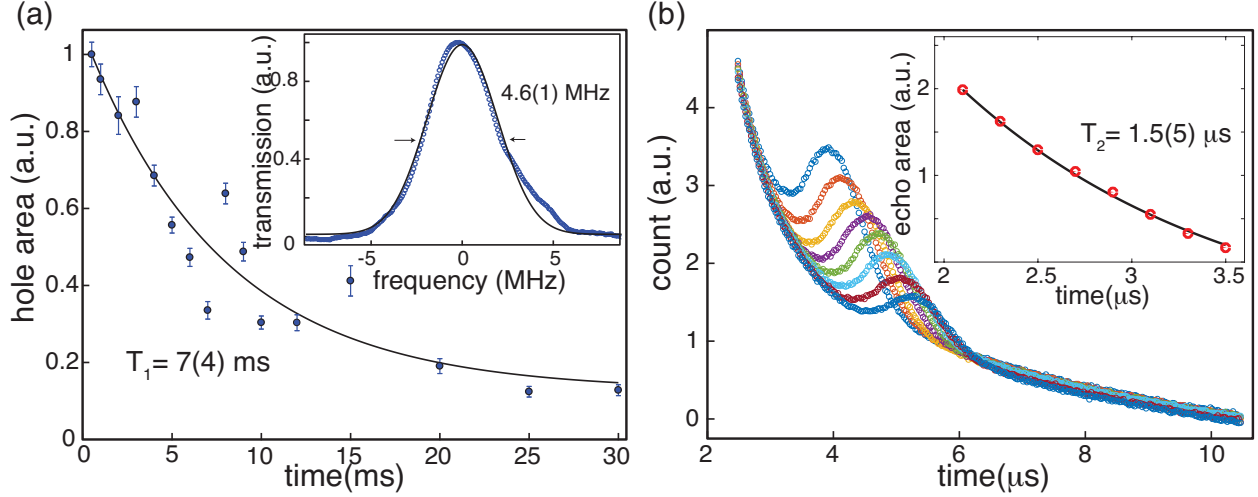


Figure 7.2. a) The population lifetime measured by observing the area of the spectral hole probed at different delay times after pumping. Inset shows the linewidth of a single hole in inhomogeneously broadened absorption spectrum. b) A two-pulse photon echo technique is used to measure the dephasing time at 4K probed by 1538nm light corresponding to the $I_{13/2}$ to $I_{15/2}$ transition. The echo area is plotted at varying delays between $\pi/2$ and π pulses of duration $0.8\mu s$ and $1.6\mu s$, respectively. The minimum time delay of $2.1\mu s$ is chosen to avoid the spontaneous emission caused by the nonideal π pulse.

The spectral hole measured by scanning the probe light frequency after a single pump pulse depopulates ground states of Er ions is observed as enhancement in transmission spectrum. The area under the hole is measured for different delay times (Fig.7.2 a) between pump and probe to identify the population lifetime, T_1 . To measure ions coherence time, T_2 , we use a two-pulse echo technique whereby delaying the timing between two π pulses, an echo signal is recorded. The decay rate of the echo is a measure of homogeneous broadening, $1/T_2$ (Fig.7.2 b). The values of T_1 and T_2 and width of the absorption line as a measure of inhomogeneous broadening are used in numerical simulations.

7.4 Results

By repeating the hole burning process using a pair of counterpropagating pump pulses creating a standing-wave pump, we write spatio-spectral holes to create an atomic population grating. The standing-wave pump inside the crystal burns hole into the absorption spectrum

only near the antinode locations while atoms near nodes remain in the ground state. Here, polarization of light is perpendicular to D1 axis, where the absorption is maximum. Such atomic population grating behaves like an atomic array whose spatially coherent mode gives rise to coherent backscattering analogous to an optical grating. We note that the spectral hole in this case is a transient hole where excited atoms decay to the ground state reducing reflection over time. To better isolate this complex hole burning dynamics and reduce the spontaneous emission noise, it is possible to optically pump atoms to an auxiliary state using a stimulated decay process [99]. Fig.7.3 (a) shows the reflection of a continuous probe light after a pair of counterpropagating pump create the atomic grating. The decay in the reflection is attributed to decay of the hole as shown in Fig.7.2 (a). In addition, a high-power probe light itself can induce reduction of the population grating contrast via absorption or stimulated emission. This is confirmed by delaying the probe pulse with respect to the end of pumping window. The reflection intensity decays slower when the probe is off. This is confirmed separately by measuring reflection at lower probe powers. Fig.7.3 (b) shows measured reflection and its exponential fitting as a function of pump's duration and power.

The total reflection reaches a plateau at high pump intensities as atomic transitions saturate. The standing-wave structure of the pump starts to quickly fade as frequency difference between the two pump pulses increases giving rise to reduced reflection. For a pump of 1ms duration, a frequency difference of 1kHz results in phase change of order 2π that spoils the standing-wave structure, in agreement with observation in Fig.7.3 (c). Using a 0.005% doped $Er : YSO$ crystal, we measure a maximum reflection efficiency of about 10% using a $50\mu W$ probe. We have also observed that averaged reflection doubles when 1% doped $Er : YSO$ crystal is used due to its higher optical density.

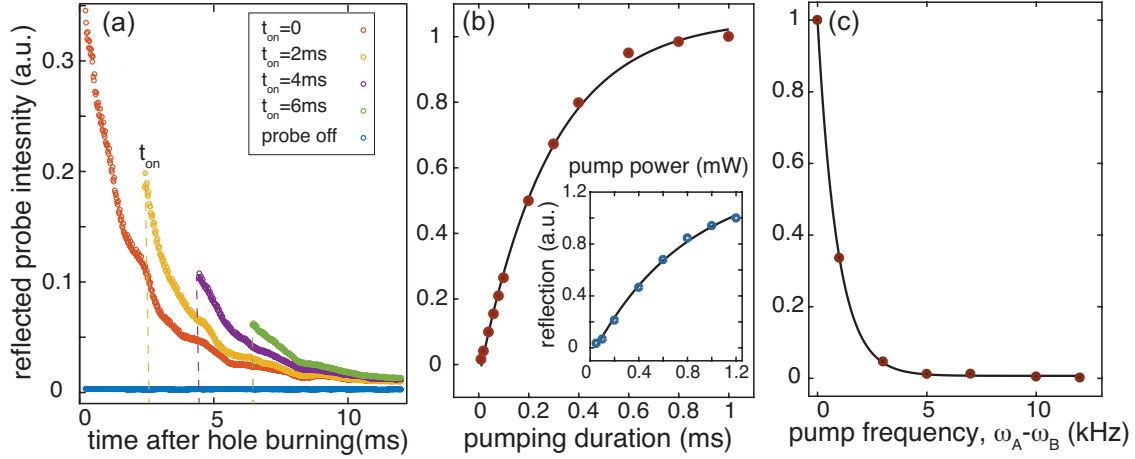


Figure 7.3. (a) Backscattered (reflected) probe after spatio-spectral hole burning ($t=0$) as a function of probe time. Reflection drops with time as population decays and probe washes out the atomic grating over time. By shifting the start of the probe pulse (t_{on}), probe-induced loss is evidenced. The spontaneous emission is also shown (pump off, blue circles), which is negligible compared to the reflected light. (b) Normalized probe reflection (peak intensity) is shown as a function of pump duration and pump power (inset). Here, the probe pulse starts at $50\mu s$ after turning off the pump pulse to avoid any leakage. The solid lines are exponential fits of form $1 - Ae^{-x/x_0}$ used to capture the saturation behavior of the ions. Here A and x_0 are the fitting parameters. A pump power and duration of $1mW$ and $400\mu s$ is used for the main plot and the inset, respectively. A maximum reflection of 10% is measured from a $50\mu W$ probe, which corresponds to normalized value 1 in the vertical axes. (c) Normalized probe reflection (peak intensity) is plotted as a function of frequency difference between the counter-propagating pumps, $\omega_a - \omega_b$, of $1ms$ duration. All measurements were done at $4K$ and probe duration is $10ms$.

The spectral hole has a linewidth which is ultimately limited by atomic linewidth but in our case, it is dominated by pump frequency instability during the pumping stage. As the result, the frequency-dependent probe reflection and transmission is expected to have a profile matching that of the spectral hole. Fig.7.4 (a) shows the probe transmission and reflection as a function of probe frequency with respect to the pump frequency. Interestingly, the reflection appears to have a local minimum at the resonant frequency. This is due to spatial distribution of atomic excitations near the node of the pump's standing wave. Because of the contribution from ions slightly away from the antinode location, incoherent probe scattering is enhanced near the resonance frequency giving rise to more loss. Such effect has also been

manifested in laser-trapped atoms near fibers [6]. Such spatial broadening can be reduced by shortening the pump pulse duration to effectively reduce the pump frequency fluctuation during the hole-burning stage. This is confirmed by observation of hole-linewidth broadening when the hole-burning process is extended in time. The probe reflection profile is also plotted in Fig.7.4 (b) for different pump durations where resonant incoherent scattering is reduced for short pumping durations. In other words, the pump frequency fluctuation during the hole-burning process reduces the quality of standing wave and thus spatio-spectral hole burning. This limits the maximum reflection. Under these conditions, and away from the resonance, probe reflection increases as it propagates further into the medium interacting with more atomic layers.

We observe that by increasing the optical density, the total coherent backscattering efficiency can increase from 10% to 20%. The backscattering efficiency does not necessarily increase linearly with ion concentration in the crystal. At high concentrations, the dipole-dipole interaction increases the broadening and decoherence rates of the ions. This problem can be avoided by creating long photonic waveguides on a low-density crystal surface to increase the optical depth. As part of future work, we have already fabricated 10mm-long waveguides with ions inside to increase the optical density without increasing the ion concentration in the host. The laser frequency stability also plays an important role in determining the quality of the atomic grating. The waveguide geometry together with laser stabilization to an external cavity can enable observation of higher atomic reflections to the point where atomic-induced cavity effects may be observed.

7.5 Conclusions

In conclusion, we have shown that the absorption profile of a randomly distributed ensemble of rare earth ions in a solid-state crystalline host can be engineered to effectively create a 1D array of atomic scatterers. Coherent interference between light scattered by atoms can reduce the propagation loss and give rise to coherent backscattering resembling a mirror. The excited ions near the antinode locations of the pump can be subsequently transferred to a different ground state via stimulated process [20] to suppress the spontaneous emission.

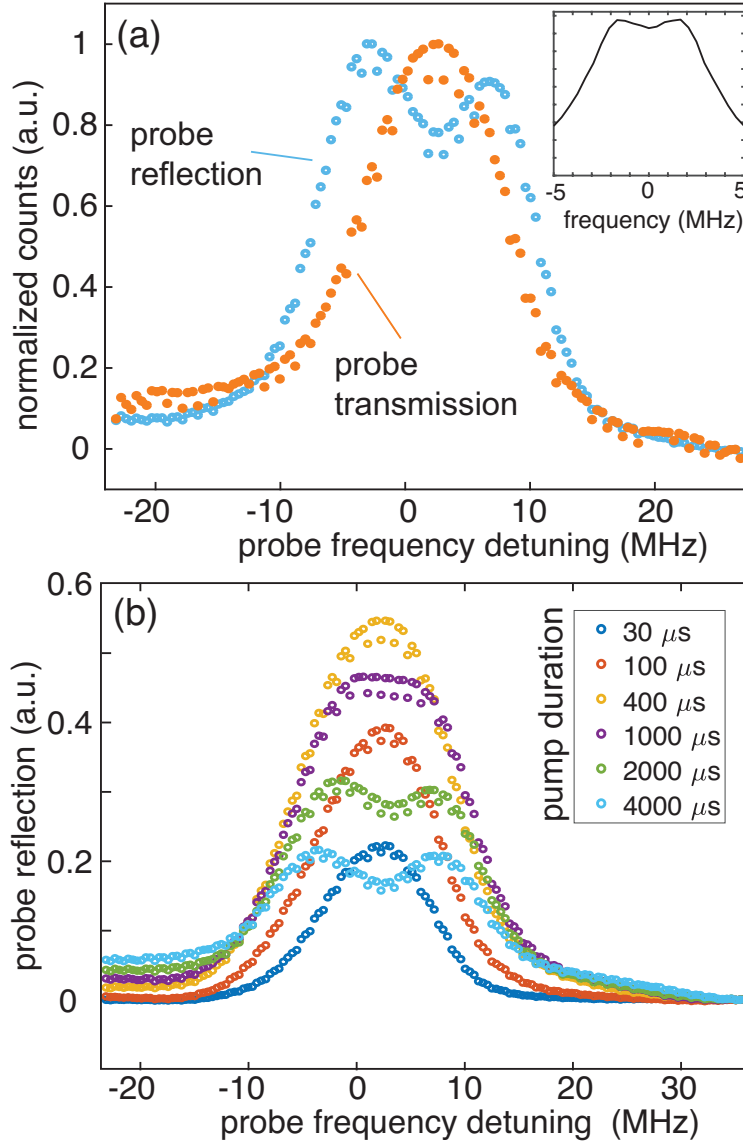


Figure 7.4. (a) Probe reflection and transmission spectra at 4K. Inset shows the result of numerical simulation taking into account the frequency fluctuation of the pumping laser. (b) Reflected probe spectra for different pumping duration is shown. The probe frequency in both plots is referenced to the center frequency of the spectral hole.

Our observation can help to enhance quantum light storage[2] and photon generation [70], [100] from rare earth solids and to further understand collective interactions as an alternative approach to create photonic cavities hosting ions. The approach uses the full atomic bandwidth and provides reconfigurable and switchable design of collective resonances.

8. PREPARATION FREE STORAGE

Quantum memories can store and retrieve arbitrary quantum states of light, which has applications in long-distance quantum communication and quantum information processing. Quantum memories are building blocks for quantum repeater architectures that allow long-distance quantum communications to overcome fiber loss. An optical quantum memory reversibly maps the photons onto long-lived coherent excitations. There has been much research devoted to realizing an efficient quantum memory.

8.1 Introduction

Rare-earth ions doped or implanted in host crystals at very low temperatures and high magnetic fields can have highly coherent quantum states in their valence orbital. For that reason, rare-earth ions in crystalline hosts have been identified as attractive media for quantum optical applications where record-high coherence times, quantum storage efficiency in solids, and quantum storage bandwidth have been demonstrated. Among rare-earth ions, Erbium uniquely possesses optical transitions at $1.5 \mu m$ region that matches the telecommunication C band. It allows a quantum memory system with Erbium to integrate with low-loss optical fibers at telecommunication wavelength.

There are still two main disadvantages in most demonstrated long-lived quantum memories. The first one is that memories are not always scalable. The second problem is almost universal, which is the time required to prepare quantum memory is much longer than the actual storage time of the memory itself.

We set up the experiment where the pump pulse itself is modulated in frequency space to solve this problem. This modulated pulse passes through the inhomogeneously broadened medium, Erbium-doped YSO crystal. An atomic frequency comb is created instantly after the modulated pulse passes through the erbium ions. If we send any optical pulse through the medium, it can store the information and work as a preparation-free quantum memory. We are also trying to make it on-demand quantum memory by adjusting the storage time with a pulsed electric field. The applied electric field will shift the energy states of the ions, which in turn change the frequency spacing Δ between the peaks of the atomic comb. This shift in Δ

will shift the storage time ($2\pi/\Delta$) according to the applied electric field. By this method, we are working on the rare earth platform offering the possibility of data storage at the telecom wavelength making the memory compatible with the existing communication infrastructure. Implementing on-demand single-photon sources at telecommunication wavelength is another broader application of the proposed research.

8.2 Traditional AFC memory

In Atomic Frequency Comb (AFC) storage protocol [101], a pulse of light is absorbed by an atomic Frequency Comb. If the intertooth spacing of the AFC is Δ , then the light will come out of a time, $t = 1/\Delta$. A frequency selective optical pumping can create a comb-like absorption profile if an atomic medium has large inhomogeneous bandwidth. This is why rare-earth ions are a popular choice as a storage medium in this protocol as they have large inhomogeneous broadening and long coherence time.

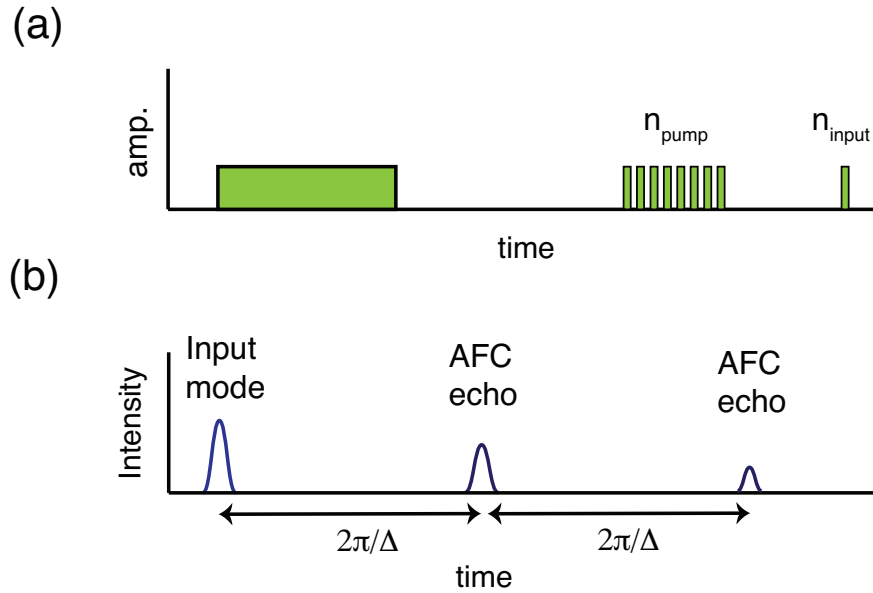


Figure 8.1. Schematic diagram of Atomic Frequency Comb. (a) shows the preparation pulse sequence to create the atomic frequency comb (AFC) structure. (b) shows The input pulse is stored and comes out as an echo after a time $t = 2\pi/\Delta$.

Let's assume the storage medium consisting ensemble of ions has an excited state $|e\rangle$, which is connected to two lower states $|g\rangle$ and $|s\rangle$. With frequency-selective pumping, the $|g\rangle \rightarrow |e\rangle$ transition is spectrally shaped in a way such that the atomic density function looks like a comb and has a series of narrow peaks of linewidth γ separated by distance Δ spanning a large frequency range. The spectrally shaped atomic density function is called as atomic frequency comb.

The light pulse that needs to be stored should have linewidth γ_p larger than the AFC peak spacings Δ . To store efficiently, γ_p also needs to be smaller than the whole frequency range spanning of AFC. Ideally, then input light can be absorbed by the AFC. This light is stored as a single excitation in the AFC over all the atoms resonant with the photon. This forms a collective state, also known as the Dicke state.

This collective state is formed by a coherent excitation of the AFC modes by the incoming photons. This collective state has a detuning of $\delta_i = n_i\Delta$, where n_i are integers and Δ is the AFC spacing. After the initial excitation, the collective state starts to dephase. The rephasing happens after a time, $t = 2\pi/\Delta$, which results in coherent reemission of light in a forwarding direction similar to the photon-echo process.

The described process is a quantum storage protocol with a fixed storage time $t = 2\pi/\Delta$. The main problem with these protocols is the preparation times are much longer than the storage time. As seen in figure 8.1(a), first frequency-selective optical pumping is applied for the creation of the comb-like structure in the inhomogeneous broadening. Creating a comb-like structure with good finesse takes a long pulse time. Once the AFC is formed, the signal is sent to the atomic medium, where the echo is retrieved after the storage time.

8.3 Experimental Approach for preparation free storage

For experimentally achieving the preparation-free storage, we used erbium-doped YSO crystal with a concentration of 0.005% as the atomic medium. The crystal was kept in a cryostat with temperatures at 4K for better coherence properties. We used a tunable continuous-wave laser for excitation at the erbium resonance wavelength. The crystal is 2x3x4 mm with crystal D1 and D2 axes perpendicular to the optical propagation direction.

The existence of nuclear spin in this isotope enables enhancement of spin coherence time to about a second at high magnetic fields and cryogenic temperatures. The electronic spin coherence time is, however, limited by spin-spin coupling and spin-lattice (phonon) coupling processes and is on the order of a few microseconds at 3.5K and small magnetic fields [98]. We use optical transition $I_{13/2}$ to $I_{15/2}$ (site 2) at 1538nm to create the atomic frequency comb.

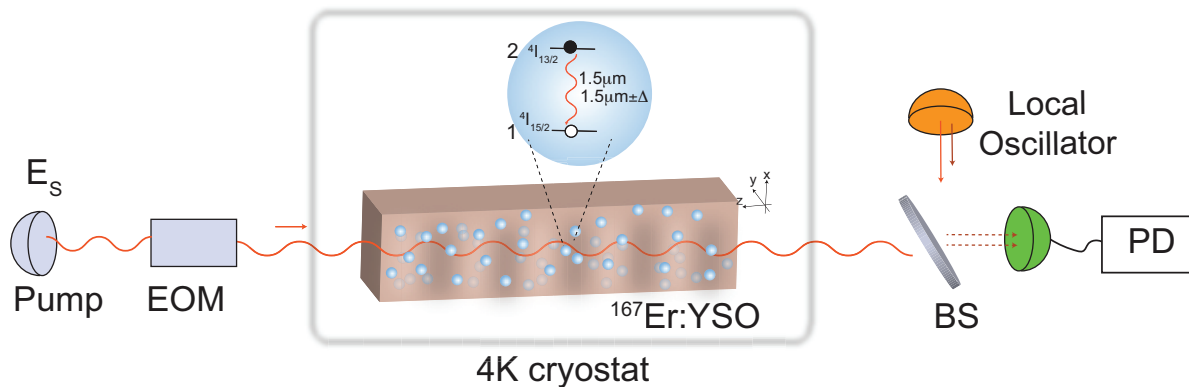


Figure 8.2. Schematic diagram of the experimental setup for the preparation free storage protocol. First, the light from the laser is modulated by the Electro-optic Modulator (EOM). Then it goes to the sample, which is kept in the 4K cryostat. Then the signal from the ions is mixed with the local oscillator using a beam splitter (BS) to do the heterodyne detection. We used a photodetector (PD) for heterodyne measurement.

For creating the atomic frequency comb, we did not use the traditional approach, which requires a long preparation time. The traditional approach for creating the AFC storage is discussed in detail in section 3.4.2. Instead, we send the laser light directly to an Electro-optic Modulator (EOM) as shown in figure 8.2 which creates sideband frequencies along with the original frequency. When this different frequency of light passes through the atomic medium, it gets absorbed by a group of atoms that are in resonance with that particular frequency. So, it creates a comb-like distribution of the density of atoms in the ground state as the erbium ions absorb modulated light. This comb shape can be controlled precisely by the modulation parameters of the EOM. The advantage of this process is the creation of the atomic frequency comb takes much less time and can be efficiently used as a memory protocol.

After creating AFC, a collective state is formed by a coherent excitation of the AFC modes by the incoming photons. This collective state has a detuning of $\delta_i = n_i\Delta$, where n_i are integers and Δ is the AFC spacing. After the initial excitation, the collective state starts to dephase. The rephasing happens after a time, $t = 2\pi/\Delta$, resulting in coherent reemission of light in a forward direction similar to the photon-echo process.

To improve the signal to ratio and check the coherence properties of the echo, we have used heterodyne measurements to detect the signal as shown in figure 8.2. The main advantage of homodyne and heterodyne detection is the gain in the detected signal. The larger the local oscillator amplitude is, the larger the gain in the detected signal will be. This relation can be easily seen by this equations:

$$I \propto [E_{sig} \cos(\omega_{sig}t + \phi) + E_{LO} \cos(\omega_{LO}t)]^2$$

$$I \propto \frac{1}{2}E_{sig}^2 + \frac{1}{2}E_{LO}^2 + 2E_{sig}E_{LO}\cos(\omega_{sig}t + \phi)\cos(\omega_{LO}t)$$

Where E_{sig} , E_{LO} are the electric field amplitude of the signal and local oscillator, respectively, if we see the last term, it does have the phase information of the signal as well as it got multiplied by the local oscillator amplitude. So, this kind of detection is beneficial for sensitive measurements as the linewidth of the modulated signal is much smaller than the optical linewidth of the signal or local oscillator. So, minimal shifts in the signal's center frequency can be measured with this technique.

8.4 Experimental Results

We have collected the results showing the echo by the protocol described above. The efficiency of this memory depends on the modulation parameters. The results for EOM modulation frequency at 5MHz and 10 MHz are presented in the figure below.

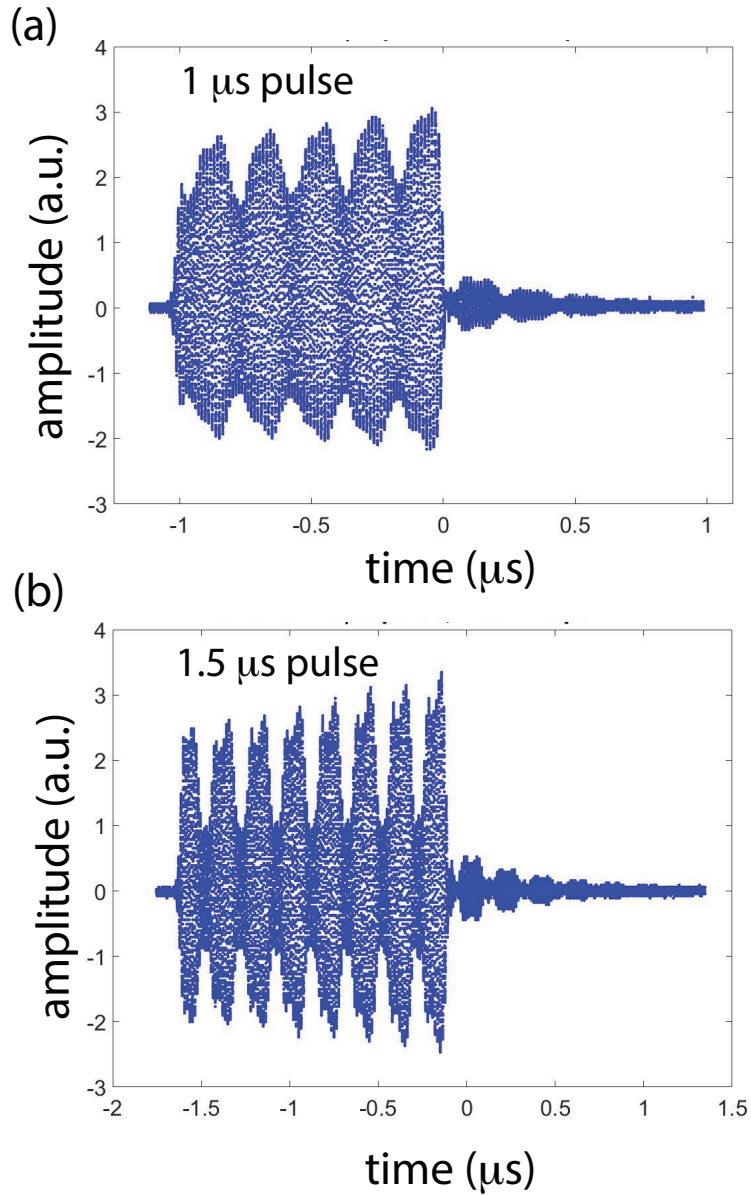


Figure 8.3. Experimental results for echo measurements at modulation frequency of 5MHz. Here $\delta/2\pi$ is 5 MHz and the echo comes out at every $2\pi/\delta = 200ns$.

For a modulation frequency of 10 MHz, as the δ increases, $2\pi/\delta$ decreases. So, the echo will come quicker, and the intensity will increase, as seen in the figure below.

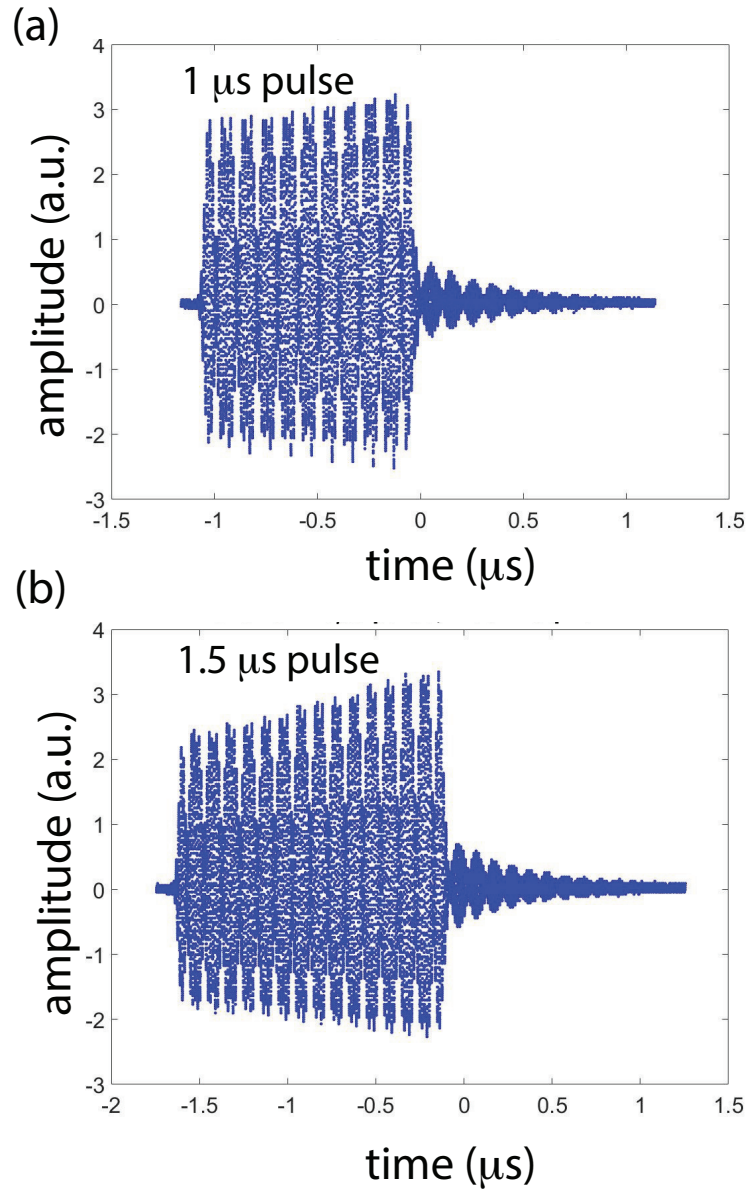


Figure 8.4. Experimental results for echo measurements at modulation frequency of 10MHz. Here $\delta/2\pi$ is 10 MHz and the echo comes out at every $2\pi/\delta = 100ns$.

Here, memory efficiency is also good, and more importantly, it can be achieved without a long preparation time, which is very useful.

8.5 On-demand memory

One crucial thing about ideal quantum memory is retrieving the data on demand. This can be achieved by our memory protocol also by manipulating the applied electric field [102].

The control via an electric field can be done in two ways. First, the phase of the output light can be modified if we apply the electric field between the absorption and emission. On the other hand, if we use the electric field while the echo is coming out, we can control the frequency profile of the echo.

To achieve this experimentally, we used a high voltage source that can generate up to 3KV voltage difference and installed a switch that can create fast pulses needed to see this effect. It is essential to have a practical circuit that can work with this very high voltage and have very little noise so that the signal can be identified clearly. Also, electrodes on the two sides of the crystal were mounted to create a significant potential difference along the b axis of the crystal. It is an ongoing project, and we are still trying to make the experimental system better for higher detection efficiency and better signal-to-noise ratio.

8.6 Conclusion

In conclusion, this project addresses a fundamental problem in on-demand quantum memory and finds a practical solution for preparation-free storage at telecommunication wavelength.

9. CONCLUSION AND FUTURE DIRECTION

The primary goal in this thesis was to use an ensemble of ions and geometric structure to enhance light atom interactions and build an atomic array for low loss, efficient quantum memory. Several theoretical and experimental platforms are presented throughout the thesis, where we have successfully executed our approach and got the desired results.

In recent years, engineering atomic arrays to control coherent light-atom interactions has been of great interest. Directional absorption and emission can also result from the collective emission of atomic arrays with photons. It paves the way for broadband atom-photon solid interactions. For quantum information research and development, much effort is given to platforms with trapped atoms and ions in free space, inside cavities, or near fibers. Though, most of the research is being carried out in laser-trapped atoms. But, there is a great potential for engineering interaction Hamiltonian of photons with atoms or defects centers in solid-state photonics from fundamental and applied aspects.

9.1 Summary and Conclusion

In the first theoretical project in this thesis, we investigated the role of atomic geometry on light emission and storage within a ring resonator. We showed that by designing atoms within a photonic waveguide or resonator, it is possible to boost the efficiency of the interactions significantly. Furthermore, we showed that an incommensurate lattice of atoms embedded in a ring resonator could be used to suppress loss and phase noise in the photon retrieval process. The clockwise and counterclockwise photons can be regarded as sudo-spin $1/2$ particles, and therefore lattice engineering can be used to design active topological quantum photonic structures eventually. Active elements, including quantum dots, laser trapped atoms, and rare earth ions integrated with photonic waveguides and resonators, are suitable platforms for studying cooperative effects in active photonic devices with application in classical and quantum photonics.

To test the theory results, we started working experimentally in engineering cooperative light-matter interactions to study many-body interactions, non-equilibrium dynamics, and

topological photonics to develop quantum photonic systems. For the first time, we design photonic materials by engineering the geometry of active quantum centers and photonic modes. We implement a cooperative light-matter interaction scheme in a solid-state photonic material operating at the telecommunication wavelength. By precision ion implantation of an array of atomic segments (isotopically pure Erbium ions) in a SiN resonator, we modify the material's properties through collective and long-range interactions between hybrid modes of the system. In this way, we have observed long-range atomic resonance effect and Fano-type mode interferences between atomic resonance modes and optical resonator modes. Our study paves the way for the design of active topological materials with enhanced nonlinearity and controllable multimode dynamics in quantum applications.

In the above project, we were looking for a SiN host. But SiN is an amorphous host, and implanting ions further degrades the optical properties. So, the inhomogeneous broadening of Er in SiN becomes quite large, around 400GHz, with a short coherence time, about 5ns. To improve the optical property and study other interesting effects, we tried to look into doped crystals. We have a very high coherence time and low inhomogeneous broadening in erbium-doped YSO. But the problem is doping atom is random, and we cannot create an atomic array while doping. We can create an array with implanting, but optical properties degrade significantly in implanting. So, if somehow, we can make an atomic array in a doped crystal, then we have the best combination possible to study the collective resonances. So, we did the next project described below to create an atomic array in the Er-doped YSO crystal.

In the subsequent experimental project, we have shown that the absorption profile of a randomly distributed ensemble of rare-earth ions in a solid-state crystalline host can be engineered to create a 1D array of atomic scatterers effectively. Coherent interference between light scattered by atoms can reduce the propagation loss and give rise to coherent back-scattering resembling a mirror, giving rise to more than 10% reflection in our system. More than 90% coherent back-scattering can be achieved by increasing ion concentration (100x) or creating long photonic waveguides on the crystal surface. Our observation can help to enhance quantum light storage and photon generation from rare earth solids.

9.2 Future Direction

We are continuously trying to improve the results of our previous experiments. Here, I am describing some of the ongoing works I am a part of related to this thesis.

9.2.1 Atomic mirror assisted light trapping

In one of our experimental projects, we have shown that the absorption profile of randomly distributed erbium ions in a YSO can be engineered to create an atomic array effectively. Coherent interference between light scattered by this atomic array gives coherent back-scattering resembling a mirror. At high concentrations, the dipole-dipole interaction increases the decoherence rates of the ions.

This problem can be avoided by creating long photonic waveguides on a low-density crystal surface to increase the optical depth. To solve this, we have fabricated long waveguides in LiNbO₃ with rare-earth ions implanted to increase the optical density without increasing the concentration. Higher atomic reflections can result in atomic-induced cavity effects. This can help to enhance quantum light storage and photon generation [70], [100] from rare earth solids and to further understand collective interactions as an alternative approach to create photonic cavities hosting ions. The approach uses the total atomic bandwidth and provides a reconfigurable and switchable design of collective resonances.

9.2.2 Long-range cooperative resonances in Solid-state platform

After our success in implementing a cooperative light-matter interaction scheme in SiN material operating at the telecommunication wavelength, we investigate improving our result by choosing appropriate quantum emitter, host, and photonic design. Integrated solid-state photonics based on lithium niobate (LN) materials provide salable platforms as hosts for REIs. Furthermore, ion implantation in photonic materials has shown low inhomogeneous and homogeneous broadenings. In this project led by my lab-mate Dongmin, we have precisely implanted Tm_{2+} ions in LN micro-ring resonators.

We showed in this project that cooperative effects could be observed in an ordered ion array extended far beyond the light’s wavelength. We observe enhanced emission from both cavity-induced Purcell enhancement and array-induced collective resonances at cryogenic temperatures. We are still designing geometry for the precise implantation of rare-earth ions in other host materials to improve our results. The solid-state and multifunctionality of the materials hosting rare-earth ions can open possibilities of new quantum photonic device engineering for applications in scalable and multiplexed quantum networks. This work has been submitted for publication with the title ”Long-range Cooperative Resonances in Rare-Earth Ion Arrays inside Photonic Resonators”[90].

9.2.3 Preparation free storage

I also want to mention the ongoing work in building preparation-free quantum storage. We propose a novel technique to store optical qubits in a solid-state platform where a long preparation time can be avoided. To date, most of the demonstrated long-lived quantum memories have two main disadvantages. The first one is that memories are not always scalable. The second problem is almost universal, which is the time required to prepare quantum memory is much longer than the actual storage time of the memory itself.

We set up the experiment where the pump pulse itself is modulated in frequency space to solve this problem. This modulated pulse passes through the inhomogeneously broadened medium, an erbium-doped YSO crystal. An atomic frequency comb is created instantly after the modulated pulse passes through the erbium ions. If we send any optical pulse through the medium, it can store the information and work as a preparation-free quantum memory. We are also trying to make it on-demand quantum memory by adjusting the storage time with a pulsed electric field. The applied electric field will shift the energy states of the ions, which in turn change the frequency spacing Δ between the peaks of the atomic comb. This shift in Δ will shift the storage time ($2\pi/\Delta$) according to the applied electric field. By this method, we are working on the rare earth platform offering the possibility of data storage at the telecom wavelength making the memory compatible with the existing communication infrastructure.

Implementing on-demand single-photon sources at telecommunication wavelength is another broader application of the proposed research.

REFERENCES

- [1] N. Gisin and R. Thew, “Quantum communication,” *Nature photonics*, vol. 1, no. 3, p. 165, 2007.
- [2] L.-M. Duan, M. D. Lukin, J. I. Cirac, and P. Zoller, “Long-distance quantum communication with atomic ensembles and linear optics,” *Nature*, vol. 414, no. 6862, pp. 413–418, 2001.
- [3] J. L. O’Brien, “Optical quantum computing,” *Science*, vol. 318, no. 5856, pp. 1567–1570, 2007.
- [4] P. W. Shor and J. Preskill, “Simple proof of security of the bb84 quantum key distribution protocol,” *Physical review letters*, vol. 85, no. 2, p. 441, 2000.
- [5] Y.-A. Chen, Q. Zhang, T.-Y. Chen, *et al.*, “An integrated space-to-ground quantum communication network over 4,600 kilometres,” *Nature*, vol. 589, no. 7841, pp. 214–219, 2021.
- [6] M. Pant, H. Krovi, D. Towsley, *et al.*, “Routing entanglement in the quantum internet,” *npj Quantum Information*, vol. 5, no. 1, pp. 1–9, 2019.
- [7] M. P. Hedges, J. J. Longdell, Y. Li, and M. J. Sellars, “Efficient quantum memory for light,” *Nature*, vol. 465, no. 7301, pp. 1052–1056, 2010.
- [8] E. Saglamyurek, J. Jin, V. B. Verma, *et al.*, “Quantum storage of entangled telecom-wavelength photons in an erbium-doped optical fibre,” *Nature Photonics*, vol. 9, no. 2, pp. 83–87, 2015.
- [9] S. Probst, *Hybrid quantum system based on rare earth doped crystals*. KIT Scientific Publishing, 2016, vol. 16.
- [10] A. Dibos, M. Raha, C. Phenicie, and J. D. Thompson, “Atomic source of single photons in the telecom band,” *Physical review letters*, vol. 120, no. 24, p. 243601, 2018.
- [11] M. Rancic *et al.*, “High resolution spectroscopy of erbium doped solids,” 2017.
- [12] T. Bottger, *Laser frequency stabilization to spectral hole burning frequency references in erbium-doped crystals: material and device optimization*. Montana State University, 2002.
- [13] M. O. Scully and M. S. Zubairy, *Quantum optics*, 1999.

- [14] D. F. Walls and G. J. Milburn, *Quantum optics*. Springer Science & Business Media, 2007.
- [15] G. Hétet, *Quantum memories for continuous variable states of light in atomic ensembles*. Australian National University, 2008.
- [16] M. Hosseini *et al.*, “Quantum optical storage and processing using raman gradient echo memory,” 2012.
- [17] I. Craiciu, M. Lei, J. Rochman, *et al.*, “Nanophotonic quantum storage at telecommunication wavelength,” *Physical Review Applied*, vol. 12, no. 2, p. 024062, 2019.
- [18] J. Zhang, G. Pagano, P. W. Hess, *et al.*, “Observation of a many-body dynamical phase transition with a 53-qubit quantum simulator,” *Nature*, vol. 551, no. 7682, pp. 601–+, 2017, ISSN: 0028-0836. DOI: [10.1038/nature24654](https://doi.org/10.1038/nature24654).
- [19] H. Bernien, S. Schwartz, A. Keesling, *et al.*, “Probing many-body dynamics on a 51-atom quantum simulator,” *Nature*, vol. 551, no. 7682, pp. 579–+, 2017, ISSN: 0028-0836. DOI: [10.1038/nature24622](https://doi.org/10.1038/nature24622).
- [20] R. H. Dicke, “Coherence in spontaneous radiation processes,” *Phys. Rev.*, vol. 93, pp. 99–110, 1 1954. DOI: [10.1103/PhysRev.93.99](https://doi.org/10.1103/PhysRev.93.99). [Online]. Available: <https://link.aps.org/doi/10.1103/PhysRev.93.99>.
- [21] M. Scheibner, T. Schmidt, L. Worschech, *et al.*, “Superradiance of quantum dots,” *Nature Physics*, vol. 3, no. 2, p. 106, 2007.
- [22] C. Bradac, M. T. Johansson, M. van Breugel, *et al.*, “Room-temperature spontaneous superradiance from single diamond nanocrystals,” *Nature communications*, vol. 8, no. 1, p. 1205, 2017.
- [23] J. G. Bohnet, Z. Chen, J. M. Weiner, D. Meiser, M. J. Holland, and J. K. Thompson, “A steady-state superradiant laser with less than one intracavity photon,” *Nature*, vol. 484, no. 7392, p. 78, 2012.
- [24] A. Goban, C.-L. Hung, J. Hood, *et al.*, “Superradiance for atoms trapped along a photonic crystal waveguide,” *Physical review letters*, vol. 115, no. 6, p. 063601, 2015.
- [25] Y.-A. C. *et al.*, “Memory-built-in quantum teleportation with photonic and atomic qubits,” *Nature Phys.*, vol. 4, p. 103, 2008.
- [26] K. S. Choi, A. Goban, S. B. Papp, and S. J. van Enk and H. J. Kimble, “Entanglement of spin waves among four quantum memories,” *Nature*, vol. 468, p. 412, 2010.

- [27] M. Parniak, M. Dabrowski, M. Mazelanik, A. Leszczynski, M. Lipka, and W. Wasilewski, “Wavevector multiplexed atomic quantum memory via spatially-resolved single-photon detection,” *Nat. Commun.*, vol. 8, p. 2140, 2017, ISSN: 2041-1723.
- [28] N. V. Corzo, B. Gouraud, A. Chandra, *et al.*, “Large bragg reflection from one-dimensional chains of trapped atoms near a nanoscale waveguide,” *Physical review letters*, vol. 117, no. 13, p. 133603, 2016.
- [29] I. Aharonovich, D. Englund, and M. Toth, “Solid-state single-photon emitters,” *Nat. Photonics*, vol. 10, no. 10, pp. 631–641, 2016, ISSN: 1749-4885. DOI: [10.1038/NPHOTON.2016.186](https://doi.org/10.1038/NPHOTON.2016.186).
- [30] S. Bogdanov, M. Y. Shalaginov, A. Boltasseva, and V. M. Shalaev, “Material platforms for integrated quantum photonics,” *Opt. Mater. Express*, vol. 7, no. 1, pp. 111–132, 2017, ISSN: 2159-3930. DOI: [10.1364/OME.7.000111](https://doi.org/10.1364/OME.7.000111).
- [31] G. Collecutt and P. D. Drummond, “Extensible multi-dimensional simulator,” *Computer Physics Communications*, vol. 142, pp. 219–223, 2001.
- [32] I. H. Deutsch, R. J. C. Spreeuw, S. L. Rolston, and W. D. Phillips, “Photonic bandgaps in optical lattices,” *Phys. Rev. A*, vol. 52, no. 2, pp. 1394–1410, 1995, ISSN: 1050-2947.
- [33] E. Shahmoon, D. S. Wild, M. D. Lukin, and S. F. Yelin, “Cooperative resonances in light scattering from two-dimensional atomic arrays,” *Physical review letters*, vol. 118, no. 11, p. 113601, 2017.
- [34] J. S. Douglas, H. Habibian, C. .-. Hung, A. V. Gorshkov, H. J. Kimble, and D. E. Chang, “Quantum many-body models with cold atoms coupled to photonic crystals,” *Nat. Photonics*, vol. 9, no. 5, pp. 326–331, 2015, ISSN: 1749-4885. DOI: [10.1038/NPHOTON.2015.57](https://doi.org/10.1038/NPHOTON.2015.57).
- [35] R. H. Dicke, “Coherence in spontaneous radiation processes,” *PHYS REV*, vol. 93, no. 1, pp. 99–110, 1954, ISSN: 0031-899X.
- [36] J. W. Czarnik and P. R. Fontana, “Resonance radiation from interacting atoms,” *J. Chem. Phys.*, vol. 50, no. 9, pp. 4071–&, 1969, ISSN: 0021-9606.
- [37] T. V. Shahbazyan, M. E. Raikh, and Z. V. Vardeny, “Mesoscopic cooperative emission from a disordered system,” *Phys. Rev. B*, vol. 61, no. 19, pp. 13266–13276, 2000, ISSN: 1098-0121.

- [38] W. Feng, Y. Li, and S.-Y. Zhu, “Effect of atomic distribution on cooperative spontaneous emission,” *Phys. Rev. A*, vol. 89, no. 1, 2014, ISSN: 1050-2947. DOI: [10.1103/PhysRevA.89.013816](https://doi.org/10.1103/PhysRevA.89.013816).
- [39] Y. Miroschnyenko, U. V. Poulsen, and K. Molmer, “Directional emission of single photons from small atomic samples,” *Phys. Rev. A*, vol. 87, no. 2, 2013, ISSN: 1050-2947.
- [40] P. M. Ledingham, W. R. Naylor, and J. J. Longdell, “Experimental realization of light with time-separated correlations by rephasing amplified spontaneous emission,” *Physical review letters*, vol. 109, no. 9, p. 093 602, 2012.
- [41] L. A. Williamson and J. J. Longdell, “Cavity enhanced rephased amplified spontaneous emission,” *New Journal of Physics*, vol. 16, no. 7, p. 073 046, 2014.
- [42] C. Simon, H. de Riedmatten, M. Afzelius, N. Sangouard, H. Zbinden, and N. Gisin, “Quantum repeaters with photon pair sources and multimode memories,” *Phys. Rev. Lett.*, vol. 98, p. 190 503, 2007.
- [43] K. Kutluer, M. Mazzera, and H. de Riedmatten, “Solid-state source of nonclassical photon pairs with embedded multimode quantum memory,” *Physical review letters*, vol. 118, no. 21, p. 210 502, 2017.
- [44] L. -. Duan, M. D. Lukin, J. I. Cirac, and P. Zoller, “Long-distance quantum communication with atomic ensembles and linear optics,” *NATURE*, vol. 414, p. 413, 2001. DOI: [10.1038/35106500](https://doi.org/10.1038/35106500). [Online]. Available: <https://doi.org/10.1038/35106500>.
- [45] C. Simon, H. De Riedmatten, M. Afzelius, N. Sangouard, H. Zbinden, and N. Gisin, “Quantum repeaters with photon pair sources and multimode memories,” *Physical review letters*, vol. 98, no. 19, p. 190 503, 2007.
- [46] Y. -. Pu, N. Jiang, W. Chang, H. -. Yang, C. Li, and L. -. Duan, “Experimental realization of a multiplexed quantum memory with 225 individually accessible memory cells,” *Nat. Commun.*, vol. 8, p. 15 359, 2017, ISSN: 2041-1723.
- [47] Y. Feng, J. Fan, X. Zhou, G. Chen, and S. Jia, “Topological superradiance in a shaken dynamical optical lattice,” *Phys. Rev. A*, vol. 99, p. 043 630, 2019.
- [48] B. Kraus, W. Tittel, N. Gisin, M. Nilsson, S. Kröll, and J. Cirac, “Quantum memory for nonstationary light fields based on controlled reversible inhomogeneous broadening,” *Physical Review A*, vol. 73, no. 2, p. 020 302, 2006.

- [49] Y. Wang, Y.-H. Lu, F. Mei, *et al.*, “Direct observation of topology from single-photon dynamics,” *Phys. Rev. Lett.*, vol. 122, no. 19, 2019, ISSN: 0031-9007. DOI: [10.1103/PhysRevLett.122.193903](https://doi.org/10.1103/PhysRevLett.122.193903).
- [50] S. Barik, A. Karasahin, C. Flower, *et al.*, “A topological quantum optics interface,” *Science*, vol. 359, no. 6376, pp. 666–668, 2018, ISSN: 0036-8075. DOI: [10.1126/science.aag0327](https://doi.org/10.1126/science.aag0327).
- [51] S. Mittal, E. A. Goldschmidt, and M. Hafezi, “A topological source of quantum light,” *Nature*, vol. 561, no. 7724, pp. 502–506, 2018.
- [52] P. Tighineanu, R. S. Daveau, T. B. Lehmann, *et al.*, “Single-photon superradiance from a quantum dot,” *Physical review letters*, vol. 116, no. 16, p. 163 604, 2016.
- [53] N. S. Perminov and S. A. Moiseev, “Spectral-topological superefficient quantum memory,” *Sci Rep*, vol. 9, no. 1568, 2019, ISSN: 2045-2322. DOI: [10.1038/s41598-018-38244-5](https://doi.org/10.1038/s41598-018-38244-5).
- [54] M. E. Kim, T.-H. Chang, B. M. Fields, C.-A. Chen, and C.-L. Hung, “Trapping single atoms on a nanophotonic circuit with configurable tweezer lattices,” *Nat. Commun*, vol. 10, p. 1647, 2019.
- [55] M. Delanty, S. Rebic, and J. Twamley, “Novel collective effects in integrated photonics,” *Eur. Phys. J. D*, vol. 66, no. 4, 2012, ISSN: 1434-6060. DOI: [10.1140/epjd/e2012-30044-2](https://doi.org/10.1140/epjd/e2012-30044-2).
- [56] J. L. O’Brien, A. Furusawa, and J. Vuckovic, “Photonic quantum technologies,” *Nat. Photonics*, vol. 3, no. 12, pp. 687–695, 2009, ISSN: 1749-4885. DOI: [10.1038/nphoton.2009.229](https://doi.org/10.1038/nphoton.2009.229).
- [57] M. F. Limonov, M. V. Rybin, A. N. Poddubny, and Y. S. Kivshar, “Fano resonances in photonics,” *Nature Photonics*, vol. 11, no. 9, p. 543, 2017.
- [58] H. Sørensen, J.-B. Béguin, K. Kluge, *et al.*, “Coherent backscattering of light off one-dimensional atomic strings,” *Physical review letters*, vol. 117, no. 13, p. 133 604, 2016.
- [59] D. Roy, C. M. Wilson, and O. Firstenberg, “Colloquium: Strongly interacting photons in one-dimensional continuum,” *Reviews of Modern Physics*, vol. 89, no. 2, p. 021 001, 2017.
- [60] S. Haroche, “Nobel lecture: Controlling photons in a box and exploring the quantum to classical boundary,” *Reviews of Modern Physics*, vol. 85, no. 3, p. 1083, 2013.

- [61] G. Borrmann, “Über extinktionsdiagramme der röntgenstrahlen von quarz,” *Phys. z.*, vol. 42, pp. 157–162, 1941.
- [62] V. Novikov and T. Murzina, “Borrmann effect in photonic crystals,” *Optics letters*, vol. 42, no. 7, pp. 1389–1392, 2017.
- [63] L. Lu, J. D. Joannopoulos, and M. Soljačić, “Topological photonics,” *Nature photonics*, vol. 8, no. 11, pp. 821–829, 2014.
- [64] S. Barik, A. Karasahin, C. Flower, *et al.*, “A topological quantum optics interface,” *Science*, vol. 359, no. 6376, pp. 666–668, 2018.
- [65] M. Mirhosseini, E. Kim, X. Zhang, *et al.*, “Cavity quantum electrodynamics with atom-like mirrors,” *Nature*, vol. 569, no. 7758, pp. 692–697, 2019.
- [66] I. Deutsch, R. Spreeuw, S. Rolston, and W. D. Phillips, “Photonic band gaps in optical lattices,” *Physical Review A*, vol. 52, no. 2, p. 1394, 1995.
- [67] T.-H. Chang, B. M. Fields, M. E. Kim, and C.-L. Hung, “Microring resonators on a suspended membrane circuit for atom–light interactions,” *Optica*, vol. 6, no. 9, pp. 1203–1210, 2019.
- [68] L. Feng, Z. J. Wong, R.-M. Ma, Y. Wang, and X. Zhang, “Single-mode laser by parity-time symmetry breaking,” *Science*, vol. 346, no. 6212, pp. 972–975, 2014.
- [69] S. Slama, C. Von Cube, M. Kohler, C. Zimmermann, and P. W. Courteille, “Multiple reflections and diffuse scattering in bragg scattering at optical lattices,” *Physical Review A*, vol. 73, no. 2, p. 023 424, 2006.
- [70] K. Furuya, A. Nandi, and M. Hosseini, “Study of atomic geometry and its effect on photon generation and storage,” *Optical Materials Express*, vol. 10, no. 2, pp. 577–587, 2020.
- [71] H. Tanji-Suzuki, I. D. Leroux, M. H. Schleier-Smith, *et al.*, “Interaction between atomic ensembles and optical resonators: Classical description,” *Advances in atomic, molecular, and optical physics*, vol. 60, pp. 201–237, 2011.
- [72] D. L. McAuslan, J. J. Longdell, and M. J. Sellars, “Strong-coupling cavity qed using rare-earth-metal-ion dopants in monolithic resonators: What you can do with a weak oscillator,” *Phys. Rev. A*, vol. 80, no. 6, 2009, ISSN: 2469-9926.
- [73] D. McAuslan, J. J. Longdell, and M. Sellars, “Strong-coupling cavity qed using rare-earth-metal-ion dopants in monolithic resonators: What you can do with a weak oscillator,” *Physical Review A*, vol. 80, no. 6, p. 062 307, 2009.

- [74] Y. Xuan, Y. Liu, L. T. Varghese, *et al.*, “High-q silicon nitride microresonators exhibiting low-power frequency comb initiation,” *Optica*, vol. 3, no. 11, pp. 1171–1180, 2016, ISSN: 2334-2536. DOI: [10.1364/OPTICA.3.001171](https://doi.org/10.1364/OPTICA.3.001171).
- [75] N. Sobolev, O. Gusev, E. Shek, V. Vdovin, T. Yugova, and A. Emel’yanov, “Dislocation-related luminescence in er-implanted silicon,” *Journal of luminescence*, vol. 80, no. 1-4, pp. 357–361, 1998.
- [76] A. Kenyon, “Erbium in silicon,” *Semiconductor Science and Technology*, vol. 20, no. 12, R65, 2005.
- [77] T. Miyakawa and D. Dexter, “Phonon sidebands, multiphonon relaxation of excited states, and phonon-assisted energy transfer between ions in solids,” *Physical Review B*, vol. 1, no. 7, p. 2961, 1970.
- [78] Y. Gong, M. Makarova, S. Yerci, *et al.*, “Linewidth narrowing and purcell enhancement in photonic crystal cavities on an er-doped silicon nitride platform,” *Optics express*, vol. 18, no. 3, pp. 2601–2612, 2010.
- [79] D. Sumida and T. Fan, “Effect of radiation trapping on fluorescence lifetime and emission cross section measurements in solid-state laser media,” *Optics Letters*, vol. 19, no. 17, pp. 1343–1345, 1994.
- [80] D. Chang, J. Douglas, A. González-Tudela, C.-L. Hung, and H. Kimble, “Colloquium: Quantum matter built from nanoscopic lattices of atoms and photons,” *Reviews of Modern Physics*, vol. 90, no. 3, p. 031 002, 2018.
- [81] D. E. Chang, L. Jiang, A. Gorshkov, and H. Kimble, “Cavity qed with atomic mirrors,” *New Journal of Physics*, vol. 14, no. 6, p. 063 003, 2012.
- [82] A. Asenjo-Garcia, M. Moreno-Cardoner, A. Albrecht, H. Kimble, and D. E. Chang, “Exponential improvement in photon storage fidelities using subradiance and “selective radiance” in atomic arrays,” *Physical Review X*, vol. 7, no. 3, p. 031 024, 2017.
- [83] M. Saffman, “Quantum computing with atomic qubits and rydberg interactions: Progress and challenges,” *Journal of Physics B: Atomic, Molecular and Optical Physics*, vol. 49, no. 20, p. 202 001, 2016.
- [84] M. Endres, H. Bernien, A. Keesling, *et al.*, “Atom-by-atom assembly of defect-free one-dimensional cold atom arrays,” *Science*, vol. 354, no. 6315, pp. 1024–1027, 2016.
- [85] M. Cetina, A. Bylinskii, L. Karpa, *et al.*, “One-dimensional array of ion chains coupled to an optical cavity,” *New Journal of Physics*, vol. 15, no. 5, p. 053 001, 2013.

- [86] A. Nandi, X. Jiang, D. Pak, *et al.*, “Controlling light emission by engineering atomic geometries in silicon photonics,” *Optics letters*, vol. 45, no. 7, pp. 1631–1634, 2020.
- [87] C. M. Phenicie, P. Stevenson, S. Welinski, *et al.*, “Narrow optical line widths in erbium implanted in tio2,” *Nano letters*, vol. 19, no. 12, pp. 8928–8933, 2019.
- [88] S. Wang, L. Yang, R. Cheng, *et al.*, “Incorporation of erbium ions into thin-film lithium niobate integrated photonics,” *Applied Physics Letters*, vol. 116, no. 15, p. 151 103, 2020.
- [89] D. Pak, H. An, A. Nandi, X. Jiang, Y. Xuan, and M. Hosseini, “Ytterbium-implanted photonic resonators based on thin film lithium niobate,” *Journal of Applied Physics*, vol. 128, no. 8, p. 084 302, 2020.
- [90] D. Pak, A. Nandi, M. Titze, E. S Bielejec, H. Alaeian, and M. Hosseini, “Long-range cooperative resonances in rare-earth ion arrays inside photonic resonators,” *Submitted for Publication*, 2022.
- [91] M. Zhong, M. P. Hedges, R. L. Ahlefeldt, *et al.*, “Optically addressable nuclear spins in a solid with a six-hour coherence time,” *Nature*, vol. 517, no. 7533, pp. 177–180, 2015.
- [92] M. Rančić, M. P. Hedges, R. L. Ahlefeldt, and M. J. Sellars, “Coherence time of over a second in a telecom-compatible quantum memory storage material,” *Nature Physics*, vol. 14, no. 1, pp. 50–54, 2018.
- [93] H. Trommsdorff, A. Corval, and L. Von Laue, “Spectral hole burning: Spontaneous and photoinduced tunneling reactions in low temperature solids,” *Pure and applied chemistry*, vol. 67, no. 1, pp. 191–198, 1995.
- [94] E. Saglamyurek, N. Sinclair, J. Jin, *et al.*, “Broadband waveguide quantum memory for entangled photons,” *Nature*, vol. 469, no. 7331, pp. 512–515, 2011.
- [95] T. Zhong, J. M. Kindem, J. G. Bartholomew, *et al.*, “Nanophotonic rare-earth quantum memory with optically controlled retrieval,” *Science*, vol. 357, no. 6358, pp. 1392–1395, 2017.
- [96] S. Chen, M. Raha, C. M. Phenicie, S. Ourari, and J. D. Thompson, “Parallel single-shot measurement and coherent control of solid-state spins below the diffraction limit,” *Science*, vol. 370, no. 6516, pp. 592–595, 2020.
- [97] C. Yin, M. Rancic, G. G. de Boo, *et al.*, “Optical addressing of an individual erbium ion in silicon,” *Nature*, vol. 497, no. 7447, pp. 91–94, 2013.

- [98] T. Böttger, C. Thiel, Y. Sun, and R. Cone, “Optical decoherence and spectral diffusion at $1.5 \mu\text{m}$ in $\text{Er}^{3+}:\text{Y}_2\text{SiO}_5$ versus magnetic field, temperature, and Er^{3+} concentration,” *Physical Review B*, vol. 73, no. 7, p. 075101, 2006.
- [99] B. Lauritzen, S. Hastings-Simon, H. De Riedmatten, M. Afzelius, and N. Gisin, “State preparation by optical pumping in erbium-doped solids using stimulated emission and spin mixing,” *Physical Review A*, vol. 78, no. 4, p. 043402, 2008.
- [100] Y. Miroshnychenko, U. V. Poulsen, and K. Mølmer, “Directional emission of single photons from small atomic samples,” *Physical Review A*, vol. 87, no. 2, p. 023821, 2013.
- [101] T. Chaneliere, J. Ruggiero, M. Bonarota, M. Afzelius, and J. Le Gouët, “Efficient light storage in a crystal using an atomic frequency comb,” *New Journal of Physics*, vol. 12, no. 2, p. 023025, 2010.
- [102] I. Craiciu, M. Lei, J. Rochman, J. G. Bartholomew, and A. Faraon, “Multifunctional on-chip storage at telecommunication wavelength for quantum networks,” *Optica*, vol. 8, no. 1, pp. 114–121, 2021.